

UCSF

UC San Francisco Electronic Theses and Dissertations

Title

Cellular and Molecular Mechanisms of Axonal Degeneration in Experimental Glaucoma

Permalink

<https://escholarship.org/uc/item/0fv3s9v3>

Author

Fu, Christine Ting

Publication Date

2010

Peer reviewed|Thesis/dissertation

Cellular and Molecular Mechanisms of Axonal Degeneration in Experimental Glaucoma

by

Christine Ting Fu

DISSERTATION

Submitted in partial satisfaction of the requirements for the degree of

DOCTOR OF PHILOSOPHY

in

Neuroscience

in the

GRADUATE DIVISION

of the

Copyright 2010

By

Christine Ting Fu

For my family

Acknowledgements

I would like to thank my advisor Dr. David Sretavan, without whom this thesis work would not have been possible. Through my time in the Sretavan lab, I have learned that the completion of a Ph.D. requires not only creativity, critical thinking and technical prowess, but also hard work, patience, independence and perseverance. The skills acquired and lessons learned during this period will remain with me for the rest of my life.

I am grateful to my thesis committee, including Drs. Steve Finkbeiner, Jennifer LaVail and Erik Ullian, for generously providing me with advice and guidance along the way. Thanks must also go to my outside committee member Dr. Ben Barres, for attending my thesis seminar and giving valuable feedbacks.

I am indebted to Dr. Louis Reichardt, director of the Neuroscience program. His caring support was instrumental in encouraging me to seize that “light at the end of the tunnel.” I would also like to acknowledge Pat Veitch and Carrie Huckaba for overseeing administrative duties in the program efficiently so we never had to worry about any paperwork.

I had the fortune of working with a group of fun and supportive colleagues in the Sretavan lab. Special thanks go to Juan Du, who was a post-doc at the beginning of my thesis research. She got me off the ground by introducing me to many basic techniques used in the lab. Tony Tran, our lab manager, took good care of us with his extraordinary organizational skills. I owed a tremendous amount to Tony’s help with maintaining the mouse colonies and many other lab chores. Wesley Chang brought to the lab an engineer’s perspective on research, which was fresh and inspiring. We shared not only

serious discussions on science and life, but also many silly laughs. Our genotyping geniuses Ryan Sze and Liz Hawkes were both wonderful colleagues who contributed to the friendly atmosphere in this lab. Fernanda Albarracin provided excellent administrative support, so we had more time to focus on our research.

Last but not least, my deepest and most sincere gratitude goes to my family: My parents, whose unfaltering love and faith in me keep hope alive, and whose sacrifices make all my sufferings seem worthwhile. My soul mate Pumpkin, the kite runner who never fails to catch me when my string gets cut, and sends me off again to the freedom of the sky. Thank you...

Statement of Contribution

Chapter 2 is modified from the following publication:

Fu, C. T. & Sretavan, D. Laser-induced ocular hypertension in albino CD-1 mice. *Invest Ophthalmol Vis Sci* **51**, 980-990 (2010).

This work was performed entirely by Christine Fu under the supervision of Dr. David Sretavan.

Part of Introduction in Chapter 3 is modified from the following review paper:

Du, J., **Fu, C. & Sretavan, D. W.** Eph/ephrin signaling as a potential therapeutic target after central nervous system injury. *Curr Pharm Des* **13**, 2507-2518 (2007).

Juan Du and Christine Fu contributed equally to literature research and writing.

The Results and Discussion sections in Chapter 3 are based on the following publication:

Fu, C. T., Tran, T. & Sretavan, D. Axonal/glia upregulation of EphB/ephrin-B signaling in mouse experimental ocular hypertension. *Invest Ophthalmol Vis Sci* **51**, 991-1001 (2010).

Tony Tran contributed to the RT-PCR analysis in Figure 3.2 and in situ hybridization data in Figure 3.3, 3.4, and 3.5.

All other experiments in Chapter 3 and Chapter 4 were designed and executed by Christine Fu, under the supervision of Dr. David Sretavan.

Cellular and Molecular Mechanisms of Axonal Degeneration in Experimental Glaucoma

by

Christine Ting Fu

ABSTRACT

Glaucoma is a major cause of blindness worldwide, and is characterized by the progressive loss of retinal ganglion cells (RGCs). Although elevated intraocular pressure (IOP) has been identified as a principal risk factor, IOP-reducing treatment does not always lead to favorable clinical outcomes. Delineating the cellular and molecular mechanisms of glaucoma pathogenesis is therefore instrumental in designing IOP-independent neuroprotective interventions. This dissertation uses an experimental model of mouse glaucoma to explore the mechanisms of axonal degeneration, with a focus on the optic nerve head (ONH) generally accepted as an important site of initial axon injury.

I first established and characterized Laser-Induced Ocular Hypertension (LIOH) in albino mice as an experimental glaucoma model. IOP elevation is triggered by photocoagulation of the aqueous humor outflow pathway, resulting in pathologies that recapitulate characteristics of glaucoma. This study offers the research community a temporally-controlled new tool amenable to both pharmacological and genetic manipulations.

I next investigated the role of EphB/ephrin-B signaling in this experimental model. *EphB* and *ephrin-B* mRNAs are upregulated in ONH axons and glia early in glaucoma, and reverse ephrin-B signaling is preferentially activated in morphologically normal compared to aberrant axons. Genetic ablation of EphB2 or EphB3 results in more severe axonal degeneration, while C-terminal truncation partially reduces the effect of EphB2, suggesting that the EphB/ephrin-B system protects axons against glaucomatous injury via bidirectional signaling.

In the third project, I present evidence of localized excitotoxicity that plays a role in RGC axonal degeneration. Ectopic accumulation of synaptic vesicle-like structures can undergo exocytosis and release glutamate at the glaucomatous ONH. Pharmacological antagonism of glutamate signaling preserves RGC axon integrity *in vitro* and *in vivo*. *Cre/loxP*-mediated deletion of the vesicular glutamate transporter VGLUT2 or the obligatory NMDA receptor subunit NR1 in RGCs confers protection against axonal degeneration, supporting the *in vivo* significance of this pathway.

Together, these findings provide insight into the complex pathways activated by IOP elevation in glaucoma, involving both pro-survival and pro-degeneration signals. Improved understanding of these mechanisms may contribute to combinatorial therapeutic strategies that tip the balance toward intrinsic neuroprotective programs while mitigating the effect of pathogenic pathways.

TABLE OF CONTENTS

CHAPTER 1

GENERAL INTRODUCTION.....	1
<i>Glaucoma Overview</i>	<i>2</i>
<i>RGC Somas Die by Apoptosis in Glaucoma.....</i>	<i>2</i>
<i>RGC Axonal Degeneration Involves Mechanisms Distinct from Soma Apoptosis.....</i>	<i>3</i>
<i>Optic Nerve Head as the Initial Site of Injury.....</i>	<i>5</i>
<i>Potential Pathogenic Mechanisms</i>	<i>6</i>
Mechanical damage	6
Neurotrophin Deprivation.....	7
Glial activation.....	8
Excitotoxicity.....	8
Vascular Insufficiency and Oxidative Stress	9
<i>Main Findings of the Dissertation.....</i>	<i>12</i>

CHAPTER 2

LASER-INDUCED OCULAR HYPERTENSION IN ALBINO CD-1 MICE.....	14
<i>Abstract.....</i>	<i>15</i>
<i>Introduction</i>	<i>16</i>
<i>Materials and Methods.....</i>	<i>18</i>
Animals.....	19
Laser-Induced Ocular Hypertension (LIOH).....	19
IOP Measurement	20
Retinal Histology and Morphometry	21
PPD Staining and Axon Counting	21

Cryostat Section Preparation.....	23
Immunohistochemistry	23
Confocal Microscopy.....	24
Retinal Whole-Mount	25
Experimental Controls	26
Statistical Analysis.....	26
<i>Results</i>	27
IOP Elevation in CD-1 Mice After Laser Treatment.....	27
Induced Cell Loss Specific to the Retinal Ganglion Cell Layer	29
Axon Degeneration in the Myelinated Optic Nerve	34
Axon Integrity in the Lamina and Pre-Lamina ONH.....	35
Axon Degeneration in the Lamina ONH Occurs Early After Laser Treatment.....	38
Aberrant Axon Trajectories at the Pre-Lamina ONH	40
Degeneration of Optic Nerve Myelin.....	41
<i>Discussion</i>	44
Selective RGC Damage After LIOH in CD-1 Mice	44
Comparison to Other Animal Models of Glaucoma	45
Characteristics of IOP Elevation in CD-1 LIOH	46
Axon Reactive Plasticity in the Pre-Lamina ONH	47
Axonal Damage as an Early Manifestation of Disease.....	48

CHAPTER 3

THE ROLE OF EPHB/EPHRIN-B SIGNALING IN EXPERIMENTAL GLAUCOMA 50

<i>Abstract</i>	51
<i>Introduction</i>	52
Potential of Contact-dependent Signaling in Glaucoma	52

The Eph and ephrin Protein Families.....	52
Diverse Eph/ephrin Functions in Development and Adulthood	53
Features of Eph/ephrin Signaling.....	56
Eph/ephrin in CNS Injury	57
Investigating Eph/ephrin Signaling in Mouse Glaucoma	58
<i>Materials and Methods</i>	60
Animals	60
Laser-Induced Ocular Hypertension (LIOH).....	60
Cryostat Section Preparation.....	60
Immunohistochemistry	61
<i>In situ</i> Hybridization	62
Real-time Polymerase Chain Reaction	62
Quantification of pEB Expression	64
Statistical Analysis.....	65
<i>Results</i>	66
Upregulation of <i>Eph</i> and <i>ephrin</i> mRNAs at the Laser-Treated ONH.....	66
ONH Expression of <i>Ephs</i> and <i>ephrins</i> in a Subset of Astrocytes	68
ONH Expression of <i>Ephs</i> and <i>ephrins</i> in Microglia	71
ONH Expression of <i>Ephs</i> and <i>ephrins</i> in Ectopic NG2 ⁺ Cells.....	73
Upregulation of ephrin-B Reverse Signaling After Laser Treatment	76
ephrin-B Reverse Signaling Differentiates Axons with Radial versus Aberrant Trajectories	81
EphB Deficiency Aggravates Glaucomatous Axonal Degeneration.....	84
<i>Discussion</i>	87
Shared Eph and ephrin Upregulation in Human Glaucoma and Animal Models	87

Early Response of Eph/ephrin System after IOP Elevation.....	87
A Broad-Based Axonal/Glial Network of Eph/ephrin Signaling.....	89
Transient ephrin-B Reverse Signaling in RGC Axons	90
Bidirectional Eph/ephrin Signaling in Axonal Protection	91

CHAPTER 4

THE ROLE OF VESICULAR GLUTAMATE RELEASE AND GLUTAMATE SIGNALING IN EXPERIMENTAL GLAUCOMA 93

<i>Abstract</i>	94
<i>Introduction</i>	95
<i>Materials and Methods</i>	97
Mouse Lines.....	97
Laser-Induced Ocular Hypertension (LIOH).....	98
Immunohistochemistry	98
Quantification of Fluorescence in Confocal Images.....	99
Immuno-Electron Microscopy	100
Synaptotagmin Labeling Assay	100
Glutamate Detection with NADH Assay	102
AGB Activation Assay	103
Organotypic Culture of Optic Nerve Explants.....	104
<i>In vivo</i> Glutamate Antagonist Treatment.....	106
Recombinant AAV Vectors	106
Intravitreal Injection.....	107
Statistical Analysis.....	107
<i>Results</i>	109
Ectopic Accumulation of Synaptic Vesicle Proteins at the Glaucomatous ONH	109

Ectopic Synaptic Vesicle Proteins Are Localized to RGC Axons But Not Astrocytes ...	111
Ultrastructural Detection of Synaptophysin-positive Vesicles in Axons at the Glaucomatous ONH.....	112
Glutamate Is contained in Ectopic SV-like Vesicles and Upregulated at the Glaucomatous ONH.....	115
Ectopic SV-like Vesicles Partially Co-localize with SNAP-25 and Bassoon.....	116
Ectopic SV-like Vesicles Can Undergo Exocytosis.....	120
Glutamate Can Be Released from the Glaucomatous ONH	124
Glutamate Receptor Expression on RGC Axons and Glia at the ONH	127
Functional Demonstration of Glutamate Receptor Activity Upregulation at the Glaucomatous ONH.....	129
Pharmacological Blockage of Glutamate Signaling Attenuates Glaucomatous Axon Degeneration <i>in vitro</i> and <i>in vivo</i>	132
Generation of Albino Mice Carrying Floxed Alleles of VGLUT2 and NR1.....	135
Intravitreal Injection of Recombinant AAV Vectors.....	136
VGLUT2 Deletion in RGCs Diminishes Glutamate Accumulation at the Glaucomatous ONH.....	137
VGLUT2 Deletion in RGCs Attenuates Glutamate Receptor Activity at the Glaucomatous ONH.....	140
NR1 Deletion in RGCs Reduces Glutamate Signaling in Axons at the Glaucomatous ONH	142
Deletion of VGLUT2 or NR1 in RGCs Promotes Axon Survival in Experimental Glaucoma	143
<i>Discussion</i>	145
Morphology and Organization of Ectopic Vesicles at the Glaucomatous ONH.....	147
Ectopic Release in Normal Physiology.....	148

Role of Axonal NMDA Receptors.....	Error! Bookmark not defined.
Excitotoxic Hotspots.....	152
Cause of Ectopic Vesicle Accumulation.....	154
<i>Supplemental Figures</i>	156
CHAPTER 5	
CONCLUSIONS	160
<i>Summary of Findings</i>	161
<i>Connecting Eph/ephrin Signaling and Glutamate Excitotoxicity</i>	163
<i>Concluding Remarks</i>	164
CHAPTER 6	
REFERENCES	166

LIST OF FIGURES

Figure 1-1. Proposed theories of glaucoma pathogenesis.....	11
Figure 2-1. Laser treatment induced IOP elevation in CD-1 mice	28
Figure 2-2. Retinal histology and morphometric analysis	30
Figure 2-3. Laser treatment resulted in decreased number of Brn-3b ⁺ RGCs	34
Figure 2-4. Axon degeneration in the myelinated optic nerve.....	35
Figure 2-5. Early occurrence of axonal damage in the lamina ONH after laser treatment	37
Figure 2-6. Aberrant axon trajectories at the pre-lamina ONH after laser treatment	39
Figure 2-7. Detection of degraded myelin basic protein (dMBP) in the optic nerve.....	43
Figure 3-1. Upregulation of <i>Eph</i> and <i>ephrin</i> mRNAs at the laser-treated ONH	67
Figure 3-2. RT-PCR analysis of <i>EphB2</i> , <i>EphB3</i> and <i>ephrin-B3</i> mRNA expression	68
Figure 3-3. <i>Eph/ephrin</i> mRNAs were expressed in a subset of ONH astrocytes	70
Figure 3-4. Microglia accumulation at the ONH after LIOH and expression of <i>Eph/ephrin</i> mRNAs	72
Figure 3-5. Ectopic NG2 ⁺ cells at the ONH expressed <i>Eph/ephrin</i> mRNAs.....	76
Figure 3-6. Upregulation of phosphorylated ephrin-B (pEB) protein	79
Figure 3-7. Expression of phospho-ephrin-B in astrocytes, axons and microglia at the lamina ONH	80
Figure 3-8. Heterogeneity of phospho-ephrin-B expression in the LIOH retina	84
Figure 3-9. <i>EphB</i> mutants exhibit more severe axonal degeneration in experimental glaucoma.....	86
Figure 3-10. Approximate timeline of pathological events after LIOH	88
Figure 4-1. Ectopic accumulation of synaptic vesicle markers at the ONH after LIOH	111

Figure 4-2. Ectopic VGLUT2 is present in axons but not astrocytes at the glaucomatous ONH.....	112
Figure 4-3. Ultrastructural analysis reveals the presence of Synaptophysin-positive vesicles at the ONH after LIOH.....	114
Figure 4-4. Immuno-detection of glutamate at the ONH.....	116
Figure 4-5. SNAP-25 and Bassoon are present at the LIOH ONH and partially overlap with VGLUT2.....	119
Figure 4-6. Living labeling with synaptotagmin luminal domain antibodies demonstrates exocytosis of ectopic vesicles.....	123
Figure 4-7. NADH assay detects release of glutamate from acutely prepared LIOH ONH tissues.....	126
Figure 4-8. Localization of glutamate receptor subunits on RGC axons and glia at the ONH.....	129
Figure 4-9. Probing ionotropic glutamate receptor activation with the channel-permeant organic cation AGB.....	132
Figure 4-10. Effects of glutamate and glutamate signaling antagonists on optic nerve axonal degeneration <i>in vitro</i> and <i>in vivo</i>	134
Figure 4-11. Effective VGLUT2 knockdown and reduction of ONH glutamate by AAV-Cre in VGLUT2-f mice.....	140
Figure 4-12. AGB assay demonstrates reduced glutamate receptor activity by AAV-Cre injection in both VGLUT-f and NR1-f mice.....	142
Figure 4-13. AAV-Cre-mediated deletion of VGLUT or NR1 is protective for RGC axons after LIOH.....	144

Figure 4-14. Proposed model of localized glutamate excitotoxicity at the glaucomatous ONH.....	146
Figure 4-15. Ectopic synaptic vesicle proteins SV2 and Synaptophysin are present in axons but not astrocytes.....	157
Figure 4-16. VAMP2 accumulation at the LIOH ONH and co-localization with SNAP-25.....	158
Figure 4-17. Efficiency and specificity of AAV-Cre transduction of RGCs.....	159

LIST OF TABLES

Table 2-1. Summary of experimental glaucoma models 18

Chapter 1

General Introduction

Glaucoma Overview

Glaucoma is a progressive neurodegenerative disease characterized by visual impairment as a result of optic nerve degeneration and retinal ganglion cell (RGC) loss. It is the second leading cause of blindness worldwide, estimated to affect 79.6 million people by the year 2020³⁰. Clinical representation of the disease is associated with changes in optic disc morphology described as “excavation,” as well as characteristic patterns of visual field defects³¹. The prevalence of glaucoma rises sharply with advancing age, leading to the prediction that it will become an even more serious health care issue as the proportion of people over forty increases. In addition, glaucoma is a complex disease with multiple associated risk factors. While ethnicity, family history, myopia and a number of systemic diseases have all been implicated, elevated intraocular pressure (IOP) remains the most well-established risk factor³². The current clinical treatment of glaucoma centers on reduction of IOP by surgical or pharmacological methods. However, it is also clear that IOP is not the sole determinant in the pathophysiology of glaucoma. Not all people with elevated IOP develop glaucoma; not all glaucoma patients exhibit ocular hypertension; and IOP lowering interventions are not always beneficial in preventing vision loss^{31,33}. In order to devise effective and IOP-independent therapeutic strategies, it is essential to understand the cellular and molecular mechanisms underlying RGC degeneration in glaucoma.

RGC Somas Die by Apoptosis in Glaucoma

A substantial body of literature has established that RGC soma death in glaucoma occurs by the process of apoptosis³⁴⁻³⁸. Both intrinsic and extrinsic apoptotic pathways play a role in glaucoma³⁹. Signals in the intrinsic pathway converge onto the mitochondria, resulting in the release of cytochrome c, activation of caspase-9 and its downstream caspase cascade, and degradation of cellular contents⁴⁰. Activated caspase-9 has been detected in rat models of experimental glaucoma⁴¹⁻⁴². Mice deficient in the pro-apoptotic factor *Bax* are completely resistant to RGC soma death in a spontaneous model of glaucoma⁴³, providing compelling evidence that the intrinsic apoptotic pathway is required. Furthermore, the extrinsic apoptotic pathway, which is triggered when Fas ligand (FasL) or tumor necrosis factor (TNF) bind to death receptors⁴⁴, may also be involved in glaucoma. Examination of chronically hypertensive rat retinas reveals upregulation of FasL and its downstream effector Fas Associated Death Domain (FADD)⁴⁵, as well as activated caspase-8^{42,46}. Our growing knowledge of the apoptotic machinery in glaucoma lays the groundwork for therapeutic approaches that may confer protection to RGC somas in glaucoma.

RGC Axonal Degeneration Involves Mechanisms Distinct from Soma Apoptosis

Glaucoma is a degenerative optic neuropathy associated with the progressive loss of RGC axons as well as cell bodies. The emerging concept of “compartmentalized self-destruction” suggests that molecularly distinct degenerative pathways may underlie the death of RGC somas and axons⁴⁷. Inactivation of the pro-apoptotic gene *Bax* in the DBA/2J mouse, an inherited model of glaucoma, leads to dramatic rescue of the RGC somas, while allowing axonal degeneration to proceed⁴³. Conversely, the Wallerian

degeneration slow (*Wld^f*) allele, which is known to protect axons against degeneration in case of neuronal injury, strongly promotes axon survival in the DBA/2J background⁴⁸. Although the number of cells in retinal flat-mounts also seems to be preserved, shrinkage of cell size has been observed in comparison to non-glaucomatous controls. In a rat experimental glaucoma model, *Wld^f* is also found to delay axon degeneration in the optic nerve, although it fails to protect the RGC somas⁴⁹. These findings suggest that axonal degeneration in glaucoma may involve Wallerian-like mechanisms, which are, at least in part, independent of soma apoptotic programs.

The autonomous and spatially localized self-destruction pathways may not be restricted to the axonal compartment of RGCs. A study by Weber et al. in 1998 documented the earliest pathological changes in primate glaucoma, most notably including a significant reduction in dendritic field size⁵⁰. The observation has since been replicated in cat⁵¹ and rat⁵² models of experimental glaucoma. A follow-up electrophysiological study demonstrated that RGCs in glaucomatous primate retinas are less responsive to visual stimuli, possibly a consequence of reduced dendritic complexity⁵³. In addition to dendritic degeneration, occurrence of compartmentalized synaptic degeneration has recently been demonstrated in DBA/2J glaucoma. In retinas with no or early stages of damage, synaptic loss in the inner plexiform layer (IPL) is observed to precede significant soma death. This reduction in synaptic density occurs concurrently with increased punctate immunoreactivity of C1q, a component of the complement cascade found to tag synapses for elimination in the developing CNS⁵⁴. Taken together, these data argue that the compartmentalized nature of RGC degeneration necessitates a combinatorial approach to neuroprotection in glaucoma. How these

compartmentalized pathways act independently and in concert with each other remains to be determined.

The principal goal of my dissertation is to explore the cellular and molecular mechanisms pertaining to the axonal degeneration pathway in glaucoma. Implications in the somatic and other pathways are equally fascinating and will be discussed, but are not the primary focus of my experiments.

Optic Nerve Head as the Initial Site of Injury

The location where glaucomatous injury first occurs has an important bearing on the design of neuroprotective therapeutic strategies. While the traditional view holds that increasing IOP directly kills RGCs within the eye, substantial evidence indicates that the initial site of injury occurs at the optic nerve head (ONH), where RGC axons exit the globe and enter the optic nerve. RGCs are the only cell type within the retina that sends long projection toward central targets. Glaucomatous cell loss is primarily limited to RGCs, while the survival of other retinal cell types is minimally affected⁵⁵⁻⁵⁷. This implies that either specific cell populations are differentially susceptible, or detrimental insults occur outside of the retina. In addition, RGC death is not uniformly distributed across the retina⁵⁸⁻⁵⁹. However, IOP is uniform within the globe and thus affects all RGCs similarly. Therefore, direct IOP impact does not seem to be a major player. Furthermore, *in vitro* examination of cellular response to pressure insult reveals that RGCs cultured alone are relatively invulnerable to elevated hydrostatic pressure⁹. Studies of RGC morphology and retrograde transport in both inherited and experimental rodent models

demonstrate that axon dysfunction and degeneration precede cell body loss⁶⁰⁻⁶¹. Ultrastructural analyses indicate that significant structural remodeling occurs early in the development of glaucoma at the ONH, where axons appear swollen with cellular organelles and axoplasmic transport becomes obstructed^{59,62-65}. Examination of *Bax*-deficient DBA/2J mice reveals that the intra-retinal axons are largely preserved until they reach the ONH, where massive degeneration ensues⁴⁸.

These findings cannot exclude the existence of parallel pathways within the retina that could impact RGC somas, dendrites or synapses. However, they strongly support the role of ONH as the initial location of axon injury. In this dissertation research, I focused on studying early changes that occur at the ONH in response to glaucomatous insults, to shed some light on mechanisms influencing the progression of axonal degeneration.

Potential Pathogenic Mechanisms

Although it is generally accepted that RGCs ultimately die by apoptosis in glaucoma, the exact insults that trigger axonal destruction and neuronal demise remain to be elucidated. A number of pathogenic mechanisms have been proposed, some of which will be discussed briefly in the following section.

Mechanical damage

The human and monkey ONH has a highly specialized structure called lamina cribrosa, consisting of collagen-rich perforated connective tissue plates through which

RGC axons and blood vessels pass. It has been proposed that the deformation of lamina cribrosa secondary to elevated IOP causes compressive damage to RGC axons^{17,66}, or restricts the delivery of nutrients through capillaries⁶⁷⁻⁶⁸. Extensive structural alterations^{15-16,18-19} and remodeling of ONH extracellular matrix (ECM)^{59,69-74} have been documented in both human patients and animal models of glaucoma. However, the development of glaucomatous RGC axon damage in mice which lack a collagenous lamina cribrosa⁴⁸ argues that additional factors other than mechanical compression are likely involved. Glial cells including astrocytes, microglia and lamina cribrosa cells also reside at the ONH. It has been proposed that these cell types may mediate glaucomatous injuries secondary to mechanical pressure⁷⁵⁻⁷⁷.

Neurotrophin Deprivation

Neurotrophin supply for the retina is thought to be derived from central visual targets. Upon engaging their Trk receptors, neurotrophins are internalized and retrogradely transported in RGC axons to reach cell bodies in the retina³⁹. Demonstration of obstructed transport of BDNF and TrkB receptors at the ONH in glaucoma²⁸⁻²⁹ is consistent with the hypothesis that neurotrophin deprivation plays a role in RGC soma apoptosis. Exogenous supply of neurotrophins has been attempted via different delivery routes, including intravitreal injection, viral delivery, and topical application⁷⁸⁻⁸². However they are delivered, significant protection observed for RGCs makes these molecules promising therapeutic agents. However, prolonging the protective effects of neurotrophin delivery presents a challenge that still needs to be overcome.

Glial activation

Substantial glial activation has been observed in human glaucoma patients as well as experimental models^{75,77}. *In vitro* evidence suggests that glial cells secrete TNF-alpha under elevated hydrostatic pressure; this results in reduced survival of co-cultured RGCs⁹. In an *in vivo* rat model, astrocytes were shown to upregulate nitric oxide synthase (NOS) at the glaucomatous ONH, and pharmacologically inhibiting NOS-2 was neuroprotective^{7,83}. Microglia in glaucomatous DBA/2J retina appeared to increase secretion of interleukin-6⁸, and attenuating microglial activation with minocycline improved optic nerve integrity⁶. These as well as other studies^{76,84} suggest that glia are significant players in the pathogenesis of glaucoma, and may be involved in mediating tissues responses to injury. It is also important to point out that some glial actions in glaucoma could be detrimental and some protective⁷⁷. Elucidating the dual roles of glia would thus provide valuable information to tip the balance toward pro-survival signals.

Excitotoxicity

Glutamate excitotoxicity has been linked to many forms of CNS pathologies, both in the context of acute injuries and chronic neurodegenerative diseases⁸⁵. Prolonged and excessive glutamate receptor stimulation could lead to build-up of intracellular calcium, ultimately setting downstream destructive pathways in motion. Activation of calcium-dependent proteases, nitric oxide synthase (NOS), and mitochondrial dysfunction have all been implicated in mediating excitotoxicity-induced neuronal death⁸⁶. It is generally

accepted that the N-methyl-D-aspartate (NMDA) receptors plays a major role in calcium permeation and excitotoxicity, although AMPA and kainate receptors have also been shown to be involved^{85,87-88}.

Excitotoxicity in glaucoma has been an attractive hypothesis; many studies have demonstrated RGCs are vulnerable to excessive glutamate or NMDA *in vitro* and *in vivo*⁸⁹⁻⁹⁵, although these findings have been recently called into question⁹⁶. Elevation of vitreal glutamate concentration was reported in human glaucoma patients and a primate glaucoma model²², as well as glaucomatous dogs²⁰. However, this finding was not replicated in later studies⁹⁷⁻¹⁰⁰, rendering the excitotoxicity hypothesis somewhat controversial. More recent data suggest that the lack of vitreal alteration in glutamate concentration does not exclude the possibility of glutamate participation in a more localized fashion. This will be discussed in more detail in Chapter 4.

Vascular Insufficiency and Oxidative Stress

Vascular insufficiency causes compromised oxygen supply, nutrient deprivation and reduced waste removal. Glaucoma patients have been shown to have impaired blood flow in vacuatures of both the retina and ONH¹⁻⁵. The vascular theory of glaucoma pathogenesis hypothesizes that ischemic insult to the ONH and/or retina results in disruption of RGC energy metabolism and oxidative stress³³. The accumulation of oxidative free radicals in glaucoma could overwhelm the endogenous antioxidant system, leading to RGC death¹⁰¹⁻¹⁰². Expression of oxidative stress markers were found to increase in glaucoma¹⁰⁻¹². Both excessive generation of reactive oxygen species (ROS)¹³⁻

¹⁴ and nitric oxide^{7,103} have been implicated in RGC injuries. Oxidative stress may be a common mechanism onto which many pathogenic pathways converge¹⁰¹.

These proposed mechanisms of glaucoma pathogenesis likely do not act in isolation, but are instead involved in a complex interplay (summarized in Figure 1-1). Understanding how these pathways interact should lead to improved understanding of the disease and offer new treatment possibilities at the clinical level.

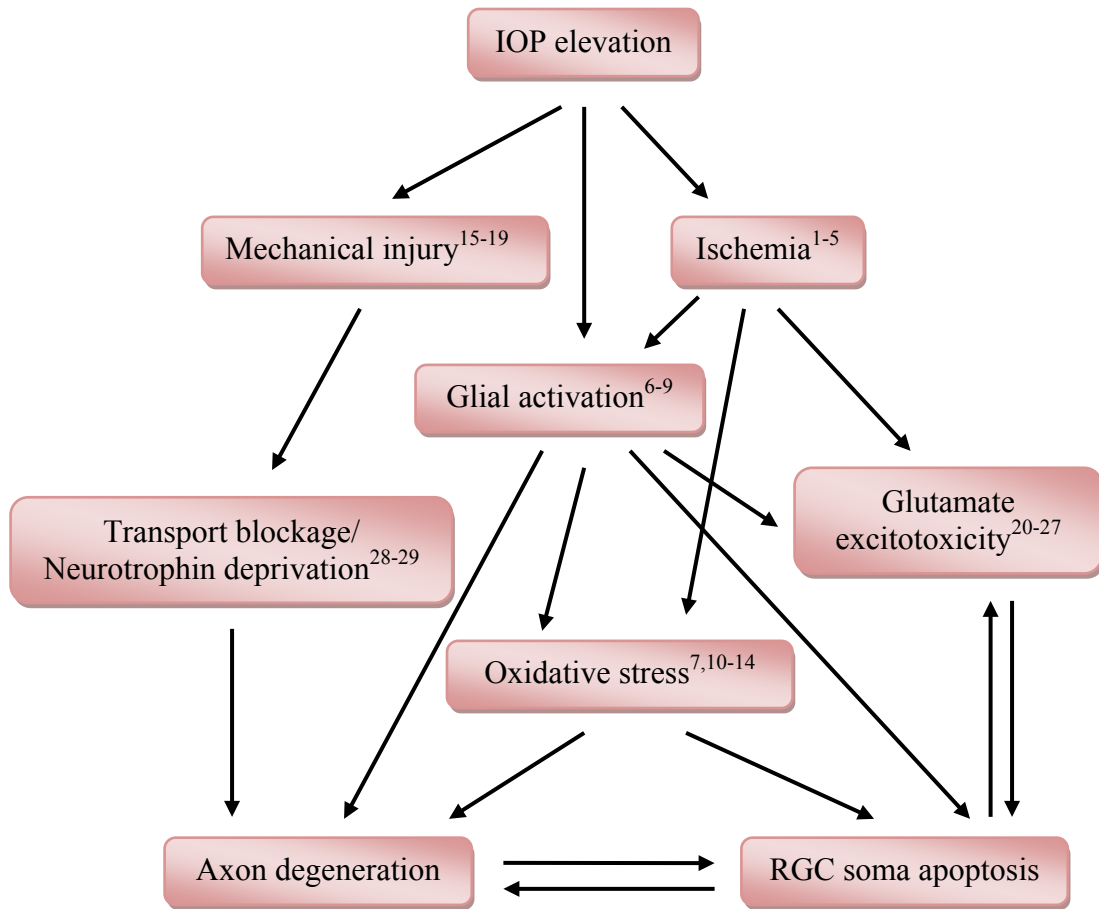


Figure 1-1. Proposed theories of glaucoma pathogenesis

Potential pathophysiological mechanisms implicated in glaucoma are summarized with corresponding references. The complex interactions between these pathways are still being elucidated.

Main Findings of the Dissertation

The first goal of my dissertation research is to establish an experimental mouse model of glaucoma, which is amenable to transgenic manipulations to interrogate specific gene function. Chapter 2 describes the protocols that I developed for a laser-induced ocular hypertension (LIOH) model in albino CD-1 mice. I characterized the progression of RGC soma loss and axon degeneration in this model, which recapitulates key features of glaucoma.

Chapter 3 contributes a small piece to the fascinating puzzle of how cellular interactions at the ONH may modulate the progression of axon degeneration in glaucoma. The Ephs and ephrins are traditionally known as axon guidance molecules playing essential roles in the developing nervous system. Here I show that the EphB/ephrin-B system is upregulated at the ONH early after experimental glaucoma both at the mRNA and activated protein levels. Using mouse mutants deficient in EphBs, I present evidence that bidirectional signaling is protective in glaucoma. The findings in this project highlight the idea that the fate of axons following glaucomatous insult depends on a balance between pro-survival and pro-degeneration signals.

In Chapter 4, I present a twist in the glutamate excitotoxicity theory of glaucoma. Contrary to the previously proposed vitreal elevation of glutamate concentration, I demonstrate localized glutamate accumulation at the glaucomatous ONH, and propose that this is a consequence of potential release from ectopic synaptic vesicles-like organelles. Prevention of glutamate transport into vesicles, or conditional deletion of the NMDA receptor subunit NR1 specifically in RGCs strongly promote axon survival in

LIOH. I have come to believe that understanding highly compartmentalized pathological mechanisms is key to conquering glaucoma. This project tells a story that expounds on that theme.

Chapter 2

Laser-Induced Ocular Hypertension in Albino CD-1

Mice

Abstract

In the first part of my dissertation research, I established a laser-induced model of ocular hypertension (LIOH) in albino CD-1 mice, and characterized the sequence of pathological events triggered by intraocular pressure (IOP) elevation. LIOH results in IOP doubling within 4 hours after laser treatment, which returns to normal level by 7 days. Axon degenerative changes, reactive plasticity, and aberrant re-growth are detected at the optic nerve head (ONH) as early as 4 days after treatment. By 7 days, axon number is significantly reduced in the myelinated optic nerve, with concurrent signs of myelin degradation. At 14 days, the density of cells expressing the RGC-specific transcription factor Brn-3b is reduced in the retina; neuronal loss is confined to the RGC layer with no apparent effects on other retinal layers. In conclusion, laser photocoagulation of limbal and episcleral veins induces transient ocular hypertension in albino CD-1 mice. The ensuing retinal and optic nerve pathologies recapitulate key features of glaucoma, and place ONH RGC axon responses as an early manifestation of damage. LIOH in albino mice may be useful as a mouse model examining mechanisms of RGC and axon degeneration in glaucomatous injury.

Introduction

Animal models of glaucoma are important tools for elucidating pathogenic mechanisms and testing potential therapeutic modalities¹⁰⁴⁻¹⁰⁸. A number of model systems (summarized in Table 2-1) have been developed in several species, each has unique strengths and limitations. Non-human primate eyes are anatomically most similar to human, yet experimentation with monkeys is limited by the high cost of purchase and maintenance of the animals. Among those rodent models that are commonly used in glaucoma research, mouse models offer the distinct advantage of genetic manipulation. While DBA/2J is currently the best-characterized mouse model of glaucoma¹⁰⁹, the genetic penetrance of the glaucoma phenotype is incomplete, and the onset of disease in individual animals cannot be precisely predicted. Furthermore, the analysis of gene function requires extensive breeding of mutant alleles into the inbred DBA/2J background. In this study, we sought to develop and characterize a laser-induced experimental model in CD-1 mice based on the following rationales: (1) CD-1 is an albino outbred stock whose genetic heterogeneity more closely mimics the variability of human population compared to inbred strains¹¹⁰. (2) Due to superior breeding performance, it is widely utilized by investigators to maintain mutant mouse strains. The addition of a CD-1 model to the repertoire of available glaucoma models would therefore enable analysis of mutant allele combinations not available in other genetic backgrounds. (3) While laser photocoagulation has previously been described in pigmented mice¹¹¹⁻¹¹⁴, no such work has been reported in strains with albino homozygosity. Since the absence of melanin dramatically alters the absorption of laser energy by ocular tissues, a distinct set of operative parameters needs to be established for the successful induction of

glaucoma. (4) Lastly, the lack of pigmentation in CD-1 mice facilitates visualization of ocular vasculature, thus enabling better targeting of laser power.

Here we describe our studies of the induction of ocular hypertension in CD-1 mice using laser photocoagulation of limbal and episcleral veins. The major pathological responses in this model consisted of RGC axon damage, and the loss of RGC molecular markers in cell somas, similar to findings in DBA/2J glaucomatous mice. Using the precise onset of ocular hypertension in this laser model, we placed these key pathological events in an approximate temporal sequence. The earliest detectable morphological sign of damaged occurred in RGC axons at the ONH, and included both degenerative changes as well as a previously undocumented phenomenon of axon reactive plasticity and aberrant growth.

Table 2-1. Summary of experimental glaucoma models

Model	Mechanism	Animal	Reference
Laser photocoagulation of trabecular meshwork and/or episcleral veins	Occlusion of aqueous humor drainage pathway	Monkey	115-116
		Rat	117-119
		Mouse	112-114
Episcleral vein injection of hypertonic saline	Sclerosis of trabecular meshwork	Rat	62
Episcleral vein cauterization	Occlusion of aqueous humor drainage pathway	Rat	36,120
		Mouse	121
Episcleral vein ligation	Occlusion of aqueous humor drainage pathway	Rat	122
Intracameral injections of hyaluronic acid	Chemical occlusion of aqueous humor drainage pathway	Rat	123
Intracameral injection of microspheres	Physical occlusion of trabecular meshwork	Monkey	124
		Rat	125-126
		Mouse	125

Materials and Methods

Animals

CD-1 mice were purchased from Charles River Laboratories (Wilmington, MA) and housed in animal facilities at the University of California, San Francisco (UCSF). Mice 3-6 months of age were used for the measurement of IOP profile (Fig. 2-1). No significant difference was noted between 3-month and 6-month old mice within this group. Subsequent experiments (Fig. 2-7) were conducted in animals 3-4 months of age. All experiments were performed in under protocols approved by the UCSF Institutional Animal Care and Use Committee, and were in accordance with the ARVO Statement for the Use of Animals in Ophthalmic and Vision Research.

Laser-Induced Ocular Hypertension (LIOH)

Adult albino CD-1 mice were anesthetized with intraperitoneal injection of 90 mg/kg ketamine HCl and 6 mg/kg xylazine. After loss of toe pinch reflex, mice were placed on the platform of a slit lamp biomicroscope equipped with a diode laser (532 nm; Lumenis, Santa Clara, CA). Photocoagulation of limbal and 3 episcleral veins was induced unilaterally (150 mW laser power, 0.2 second duration, 100 μ m diameter spot size) to obstruct aqueous outflow. The translimbal laser treatment was performed over 270-300°, sparing the nasal aspect as well as the long posterior ciliary arteries. In our experience, avoiding the long posterior ciliary arteries greatly reduced ocular

inflammation following laser surgery; the lack of pigmentation in CD-1 was advantageous in facilitating their identification. Laser spots were applied around these vessels which supply the iris from both the nasal and temporal poles, resulting in one major laser-free zone nasally and one minor laser-free zone temporally. Both eyes were kept moist with saline at all times. After surgery, bacitracin antibiotic ointment was administered to the operative eye. Each animal received only one round of laser photocoagulation treatment. The contralateral eye was untreated and served as control.

IOP Measurement

Mice anesthetized with 90 mg/kg ketamine HCl and 6 mg/kg xylazine were placed on an adjustable height platform, and IOP in both eyes was measured with the Tonolab rebound tonometer (Colonial Medical Supply, Franconia, NH) mounted on a ring stand. The probe was triggered with a custom-fitted foot pedal to minimize movement of the instrument body. To control for the diurnal variation in IOP, all measurements were taken between 10 am and noon, and as soon as loss of righting reflex was observed, to avoid the IOP-depressing effect of anesthesia¹²⁷.

Following laser treatment, only eyes with IOP elevation above 21 mm Hg were used in subsequent analysis. Although there is no accepted threshold value of IOP in mice beyond which is indicative of glaucoma, we used the value of 21 mm Hg to gauge the success of inducing ocular hypertension following the defined laser experimental protocol. Mice with overt signs of ocular inflammation were euthanized and excluded from the study.

Retinal Histology and Morphometry

Mice were anesthetized with an overdose of pentobarbital and perfused transcardially with 2% paraformaldehyde (PFA) and 2.5% glutaraldehyde in 0.1 M phosphate buffered saline (PBS, pH 7.4). Eyes were enucleated along with a segment of retrobulbar optic nerve attached. After removal of the anterior segment, lens and vitreous, eye cups consisting of retina and optic nerve were immersion-fixed in the same fixative at 4°C overnight. Samples were embedded in JB-4 plastic (Electron Microscopy Sciences, Hatfield, PA), sectioned at 2 μm , and stained with hematoxylin-eosin. Only sagittal sections through the central ONH were selected to ensure analysis of comparable retinal planes in each sample. Images were collected using a Nikon Eclipse E800 upright microscope equipped with SPOT CCD camera. Measurements of retinal layer thickness were taken from central (250 μm from the ONH), middle (750-1000 μm from the ONH) as well as peripheral (100 μm from the ora serrata) retina. Nuclei in the ganglion cell layer (GCL) were counted in 500 μm segments across the central, middle, and peripheral retinal locations defined above, and expressed as cells/mm to obtain the cell density in the linear dimension along the GCL. One tissue section was analyzed from each of the 10 pairs of control and laser-treated retinas. All measurements were made from both sides of the ONH and averaged.

Paraphenylenediamine (PPD) Staining and Axon Counting

Mice were perfused with 2% PFA and 2.5% glutaraldehyde fixative. Paraphenylenediamine (PPD) was used to stain the myelin sheath of axons as previously described¹²⁸. Briefly, optic nerves were dissected from 1mm behind the globe, and post-fixed in 2% PFA and 2.5% glutaraldehyde at 4°C. Treatment with 1% OsO₄ in PBS for 2 hours at room temperature was followed by three 10-minute washes with 0.1 M sodium acetate buffer. The tissues were then stained with 2% uranyl acetate in sodium acetate buffer for 1 hour at room temperature, washed in buffer, dehydrated in a graded ethanol series (40%–100%), and infiltrated with propylene oxide-812 resin (1005 Embed 812; EMS, Fort Washington, PA). The samples were embedded with fresh 100% 812 resin in molds and polymerized in a 60°C oven for 36 hours. Sections of 1 µm in thickness were cut and stained with 1% PPD in 1:1 methanol/isopropanol for 30 minutes, washed in fresh isopropanol twice, and coverslipped. The axon counting protocol was based on a published method with modifications⁴³. Sections were first imaged under the 20x objective lens on a Nikon TE300 microscope, and the optic nerve cross-sectional areas were traced and calculated. Non-overlapping fields spanning the entire section were then captured with the 100x lens. The images were collected into a layered Photoshop file, and a 20x15 µm box was randomly placed on the topmost image. The software then cropped out the same region in all stacked layers including those invisible to the operator, so as to remove any possibility of inadvertent bias. Manually counted axon numbers in these rectangular boxes were used to calculate myelinated axon densities, which were then averaged and multiplied by the cross-sectional area to obtain the total count of myelinated axons. Unmyelinated axons are not stained by PPD, but these represent only ~10% of the total population of axons in the adult mouse optic nerve¹²⁹. Despite its

limitations, the PPD analysis is less labor-intensive compared to electron microscopy and allows a greater number of nerves and larger areas in each sample to be quantified.

Cryostat Section Preparation

Animals were perfused transcardially with 4% PFA in 0.1 M PBS (pH 7.4). Eyes were dissected as described above, postfixed in 4% paraformaldehyde at 4°C overnight, and cryoprotected with 30% sucrose. Eye cups were then embedded in Tissue-Tek optimal cutting temperature (OCT) compound (Sakura Finetek, Torrance, CA), and 10 µm cryosections were cut along the longitudinal axis through the ONH. Sections were mounted on Super Frost Plus slides (Fisher Scientific, Springfield, NJ) and subjected to immunostaining.

Immunohistochemistry

Cryosections were air-dried at room temperature for 1 hour and washed with 0.1 M PBS, which also served as diluent for all subsequent reagents. Non-specific binding was blocked with 10% normal donkey serum (NDS) for 30 minutes at room temperature. For most experiments, tissue permeabilization was achieved by inclusion of 0.1% Triton X-100 in the blocking solution. Primary antibodies were diluted in 1% normal donkey serum and incubated with the slides overnight at 4°C. After three PBS washes of 10 minutes each, secondary antibodies were applied for 1 hour at room temperature. Slides were then washed in PBS, counterstained with 4',6-diamidino-2-phenylindole (DAPI) to

label nuclei when appropriate, and mounted in 97% 2,2'-thiodiethanol (TDE; Sigma, St. Louis, MO).

The following primary antibodies were used: rabbit anti-tubulin β -III (1:500; Sigma, St. Louis, MO), mouse anti-neurofilament (SMI312; 1:500; Covance Research Products, Denver, PA), goat anti-Brn-3b (1:50; Santa Cruz Biotechnology, Santa Cruz, CA), mouse anti-2',3'-cyclic nucleotide 3'-phosphodiesterase (CNPase; 1:500; Sigma, St. Louis, MO), and rabbit anti-degraded myelin basic protein (dMBP; 1:1000; Chemicon, Temecula, CA). Multi-color labeling was accomplished with secondary antibodies conjugated to tetramethyl rhodamine (TMR; 1:200; Invitrogen, Carlsbad, CA) or cy3, cy2, and cy5 (1:200; Jackson ImmunoResearch, West Grove, PA).

Confocal Microscopy

Fluorescence imaging was performed on an inverted confocal laser microscope (LSM5 Pascal; Carl Zeiss Meditec, Inc., Thornwood, NY), using 20x air, 63x oil or 100x oil objectives. For triple labeling experiments, images were scanned with the 488 nm, 543 nm, and 633 nm lasers to excite cy2, TMR/cy3, and cy5, respectively. Except when goat primary antibodies were used, TMR was chosen in lieu of cy3 because of its lower excitation by the 488 nm laser, thus minimizing potential bleed-through into the green channel. Scans of different fluorescent channels were collected sequentially, and laser power as well as detector gain were adjusted to eliminate bleed-through between channels.

Retinal Whole-Mount

The retinal whole-mount protocol was modified from a published study¹³⁰. Mice were perfused transcardially and eyes harvested as described above. The anterior segment, lens and optic nerve were dissected away, and the retinas were gently freed from the sclera. Care was taken to make sure a short stump of optic nerve (~100 μm) remained attached. Vitreous was removed using a pair of fine forceps. Four radial cuts were made on the retina, which was then flattened onto a small piece of Millipore filter paper. After post-fixation in 4% PFA for 30 minutes - 1 hour, the retinas were rinsed in PBS, and permeabilized with 0.3% Triton X-100 in PBS for 30 minutes. Nonspecific binding was blocked with 10% NDS in PBS containing 0.1% Tween-20 (PBST) for 30 minutes at room temperature. Primary antibody incubation was performed in PBST with 3% NDS at 4 °C overnight. Retinas were washed in PBST three times for 15 minutes each, and incubated with secondary antibodies for 1 hour at room temperature. After gradual equilibration with successively higher concentration of TDE to minimize tissue distortion, samples were mounted in 97% TDE and coverslipped. This mounting medium has the advantage of matching the refractive index of immersion oil, which minimizes spherical aberration when imaging deep into the specimen with confocal microscopy.

To analyze the morphology of pre-lamina ONH, retinal whole-mounts were scanned starting from the nerve fiber layer with the Zeiss LSM5 Pascal confocal microscope, and consecutive optical sections were taken at an interval of 0.5 μm , extending 10-20 μm deep into the ONH. Images were reconstructed as compressed z-stacks. To estimate the density of Brn-3b⁺ RGCs, three random fields of 0.2 mm² were imaged at central, middle and peripheral locations in each retina. Confocal z-stacks were

taken and compressed to account for potential irregularities in the specimen. Labeled RGC nuclei in all 12 fields were counted with the image analysis software ImageJ and then averaged.

Experimental Controls

At least three pairs of eyes or optic nerve heads were examined for every antibody marker (summarized as n number in figure legends). From each sample, at least three tissue sections were analyzed. In experiments comparing signal intensity between different treatment groups, all samples were processed in parallel and imaged under identical microscope settings. Experiments in which the primary antibody was omitted served as negative controls.

Statistical Analysis

IOP measurements and retinal morphometry data were analyzed by two-way analysis of variance (ANOVA). Where a significant main effect was found, post hoc Bonferroni multiple comparison test was conducted. The RGC cell count and axon count data were subjected to one-way ANOVA followed by Tukey's multiple comparison test. Statistical tests were performed using the GraphPad Prism (version 5) software, with a significance level set at $p < 0.05$. Values were reported as mean \pm SEM.

Results

IOP Elevation in CD-1 Mice After Laser Treatment

In this study, we sought to develop an experimental model of laser-induced ocular hypertension in CD-1 mice. After laser photocoagulation of limbal and episcleral veins of the aqueous humor outflow pathway in CD-1 mice, IOP was measured at various time points in the operative eye as well as the contralateral eye, which did not receive laser treatment and served as control. To rule out transient IOP spikes immediately following laser treatment, which could cause global retinal ischemia, we measured short-term IOP changes within the first 12 hours post-operatively (Fig. 2-1A). In a separate group of mice, we characterized the profile of IOP elevation longitudinally by measuring IOP values at 1 day, 2 days, 1 week, and 2 weeks after treatment (Fig. 2-1B). Beginning as soon as 4 hours after laser treatment, the IOPs measured in operative eyes (27.6 ± 2.6 mm Hg, $n = 7$) were significantly elevated above those measured in control eyes (12.3 ± 1.0 mm Hg, $n = 7$) and remained elevated at the second post-operative day (operative 27.1 ± 1.8 mm Hg vs. control 13.4 ± 0.3 mm Hg, $n = 38$). The IOPs measured in laser-treated eyes declined to baseline and were similar to IOPs in control eyes by 1 week (operative 15.4 ± 1.3 mm Hg vs. 12.4 ± 0.6 mm Hg, $n = 30$). The peak IOP measured immediately (29.2 ± 1.4 mm Hg, $n = 38$) and during the first week post-operatively was sufficiently below the mean blood pressure (MBP) of 102 ± 4 mm Hg reported for CD-1 mice¹³¹. Based on the formula that ocular perfusion pressure equals MBP minus IOP¹³², an eye with a 30 mm Hg IOP maintains approximately 70 mm Hg of perfusion pressure, which

is unlikely to result in global retinal ischemia. Histological analysis of retinal sections from laser-treated eyes (see Fig. 2-2 below) also revealed well-preserved tissue cytoarchitecture except in the ganglion cell and nerve fiber layers, consistent with the maintenance of normal retinal perfusion following laser-treatment.

In addition to the cohort of mice used specifically for the longitudinal analysis of IOP profile documented above, the present study consisted of 380 mice that were laser-treated and whose IOP were recorded 12-24 hours post-operation. Of these, 308 (81%) had IOP \geq 21 mm Hg and were used in subsequent analysis; 59 (16%) did not meet the 21 mm Hg criterion. A small number (3%) exhibited signs of surgical complication including hyphema or corneal edema, and were excluded from the study. In our experience with the CD-1 mice LIOH, we never observed cataract or phthisis reported for pigmented mice¹¹².

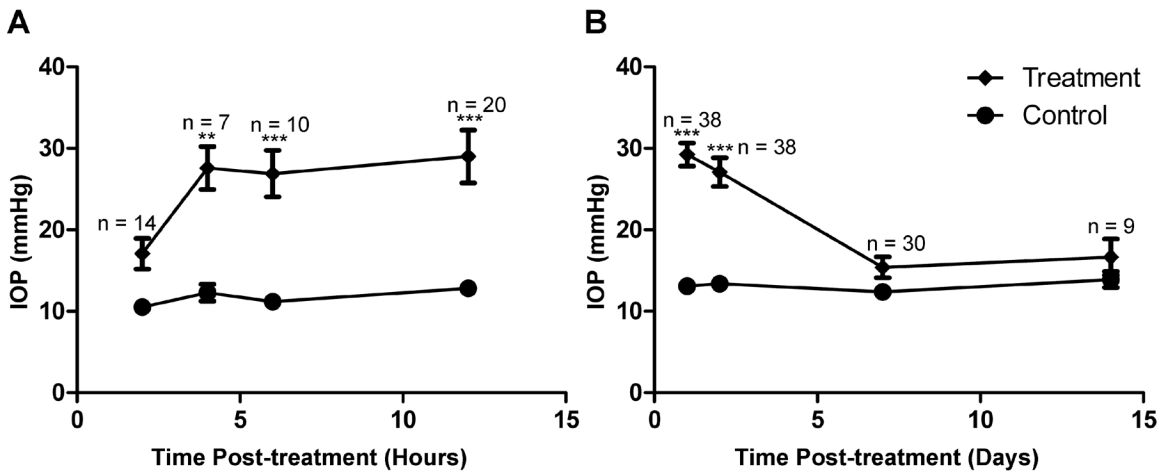


Figure 2-1. Laser treatment induced IOP elevation in CD-1 mice
 (A, B) IOP measurements within 12 hours (A) and over 2 weeks (B) after treatment. IOP significantly increased in laser-treated eyes between 4 hours and 2 days compared to contralateral control eyes. **p < 0.01; ***p < 0.001.

Induced Cell Loss Specific to the Retinal Ganglion Cell Layer

The hallmark of glaucomatous damage is the loss of retinal ganglion cells with relative sparing of other retinal layers. Retinal histology 4 weeks after laser treatment demonstrated prominent cell loss in the ganglion cell layer (GCL) as well as diminution of the nerve fiber layer (NFL) (compare Fig. 2-2A and B). The other retinal layers were not significantly changed in thickness. To quantify the pattern of damage at different retinal eccentricities, we performed morphometric analysis at central, middle and peripheral locations on H&E stained plastic sections (n = 10 for both control and laser-treated retinas). The protocol for defining these regions is illustrated in Fig. 2-2C. Linear density of cells in the ganglion cell layer (GCL) was reduced in the central (by 31%), middle (by 33%) and peripheral (by 34%) regions (Fig. 2-2D). In contrast, the thickness measurements of the inner nuclear layer (INL) and outer nuclear layer (ONL) were not significantly altered at any retinal eccentricity (Fig. 2-2E). It is worth noting that we observed visible thinning of the IPL in some laser-treated samples, consistent with the loss of RGC dendritic arbors. Although the mean IPL thickness values in experimental animals was reduced by 10%, 10%, and 14% for central, middle and peripheral retina, respectively, this was not a consistent finding and did not reach statistical significance. Overall, the pattern of retinal damage in CD-1 LIOH was consistent with the selective degeneration of RGCs, similar to that which occurs in glaucoma.

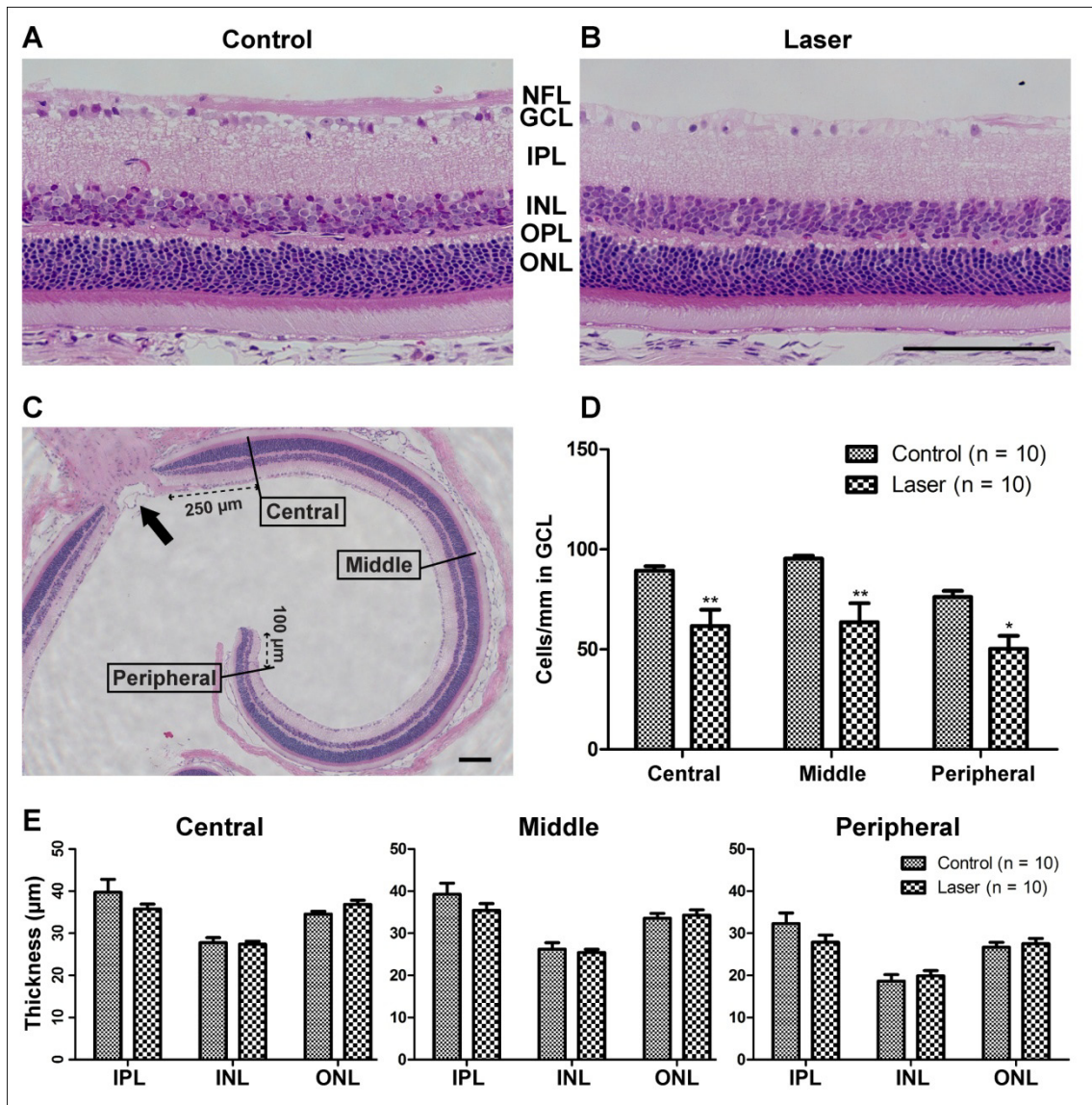


Figure 2-2. Retinal histology and morphometric analysis

(A, B) Representative images of plastic-embedded, H&E-stained retinal sagittal sections 4 weeks after laser treatment, captured 250 μm from the optic nerve head (ONH). The GCL in laser-treated eye (B) was greatly reduced in cell number compared to control (A). Apparent thinning also occurred in NFL containing RGC axons. The other retinal layers appeared relatively intact. (C) Definition of central (250 μm from the ONH), middle (750-1000 μm from the ONH) and peripheral (100 μm from the ora serrata edge) retinal locations. Note that only mid-sagittal sections through the ONH (arrow) were selected for analysis. (D) Linear density of GCL cells expressed as cells/mm was significantly reduced at all retinal locations after laser treatment. (E) The thickness of IPL, INL and ONL were not significantly impacted. NFL = nerve fiber layer. GCL = ganglion cell layer. IPL = inner plexiform layer. INL = inner nuclear layer. OPL = outer plexiform layer. ONL = outer nuclear layer. Scale bar = 100 μm . n = 10 retinas for both control and laser groups. * $p < 0.05$; ** $p < 0.01$.

In addition to histological analysis, immunolabeling was used to enable direct quantification of RGC density. Approximately 40-60% of cells in the mouse GCL are estimated to be displaced amacrine cells^{91,133-135}. Although we did not directly quantify the survival of amacrine cells, no reduction was found in the thickness of INL, which comprises 40% amacrine cells¹³⁴. This observation would argue that amacrine cells are not vulnerable in LIOH, consistent with previous reports in other rodent models of glaucoma^{58,136}. Considering the existence of displaced amacrine cells, the total number of nuclei in GCL does not provide an accurate measure of RGC survival following laser treatment. To overcome this limitation, Brn-3b antibody was utilized to specifically label RGCs in retinal whole-mounts (Fig. 2-3). Brn-3b is a transcription factor expressed in a subset of RGCs^{130,137} distributed uniformly across the retina, allowing for direct visualization and convenient RGC counting in immunostained retinal whole-mounts. Since previous studies demonstrated that no specific class of RGCs is selectively impacted in mouse glaucoma⁵⁸, we used the density of Brn-3b⁺ nuclei as a surrogate measure of the overall density of surviving RGC somas. The results showed that Brn-3b⁺ RGC density at 1 week after laser treatment was not significantly different from control (Fig. 2-3F). However, by two weeks after laser treatment there was a substantial loss of Brn-3b⁺ RGC number by 42% compared to control. By 4 weeks, the average density of Brn-3b⁺ RGCs in laser-treated eyes was reduced by 91% of controls. Thus degeneration of RGC somas as assayed by the loss of Brn-3b expression appeared to commence on average between 1 to 2 weeks after laser treatment. While it is possible that the loss of Brn-3b protein by itself may not mark the death of RGCs, histological evidences of

reduced cell number in the GCL and diminution of the NFL (Fig. 2-2B) indicate that death does occur in at least a proportion of RGCs (see Discussion). In addition, DAPI staining of experimental retinal whole-mounts revealed substantial reduction of cell number (unpublished observation), suggesting that changes in Brn-3b immunolabeling mirrored the overall pattern of RGC degeneration. Furthermore, the loss of Brn-3b⁺ RGCs was non-uniform across the retina and often appeared sectorial in nature (Fig. 2-3E). This pattern of RGC damage in laser-treated CD-1 mice is similar to what has been observed in DBA/2J animals using RGC-specific ROSA3 βGeo reporter or retrograde labeling^{58,60,138}, and is consistent with an insult to discrete axon bundles at the ONH.

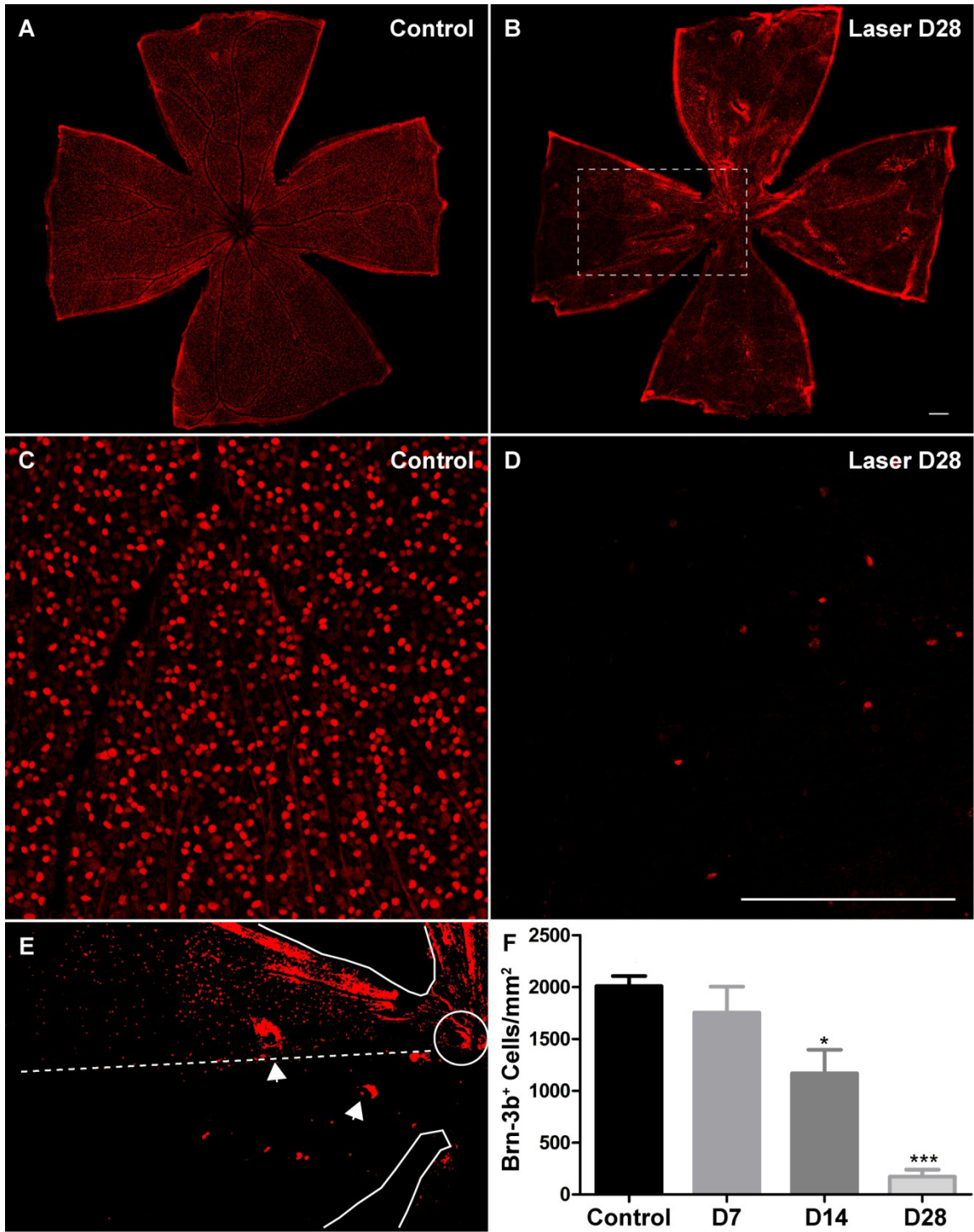


Figure 2-3. Laser treatment resulted in decreased number of Brn-3b⁺ RGCs
(A, B) Low magnification views of whole-mounted retinas immunolabeled with the Brn-3b antibody. (C, D) Representative images used for quantification of Brn-3b⁺ RGC number. (E) Higher magnification, thresholded image of boxed region in (B), highlighting the fan-shaped pattern of RGC degeneration. Solid traces mark the edges of the retinal whole-mount and the ONH. Dashed line denotes an imaginary boundary dividing a sector of relative preservation (above) from a sector of severe loss (below) of Brn-3b⁺ cells. Arrowheads point to occasional tearing of the tissue preparation. (F) The mean density of Brn-3b⁺ RGCs in experimental retinas at 2 weeks was reduced by 42% of that in contralateral control eyes, and at 4 weeks by 91% of control eyes. Scale bar = 200 μ m. For each group, 8 retinas were analyzed. * $p < 0.05$; *** $p < 0.001$.

Axon Degeneration in the Myelinated Optic Nerve

Recent evidence demonstrated that the degeneration of RGC somas and axons in glaucoma may involve distinct processes⁴³. In order to obtain an independent measure of RGC axon survival, we used paraphenylenediamine (PPD) to visualize axons in the myelinated optic nerve. PPD is a dye that uniformly labels myelin sheaths, but differentially stains the axoplasm of degenerating axons darkly⁴³. Fig. 2-4A-D shows examples of PPD-stained optic nerve cross sections harvested at different time points after laser treatment. In addition to axon degeneration indicated by darkly stained axoplasm or myelin debris (arrowheads), axon swelling (arrows) and gliosis (double arrows) were also apparent in experimental nerves. Axon counting revealed that the total axon number was reduced by 47% at 1 week, 68% at 2 weeks and 78% at 4 weeks. These data agreed with our previous findings focused on RGC somas, and confirmed that both RGC axons as well somas were damaged following LIOH.

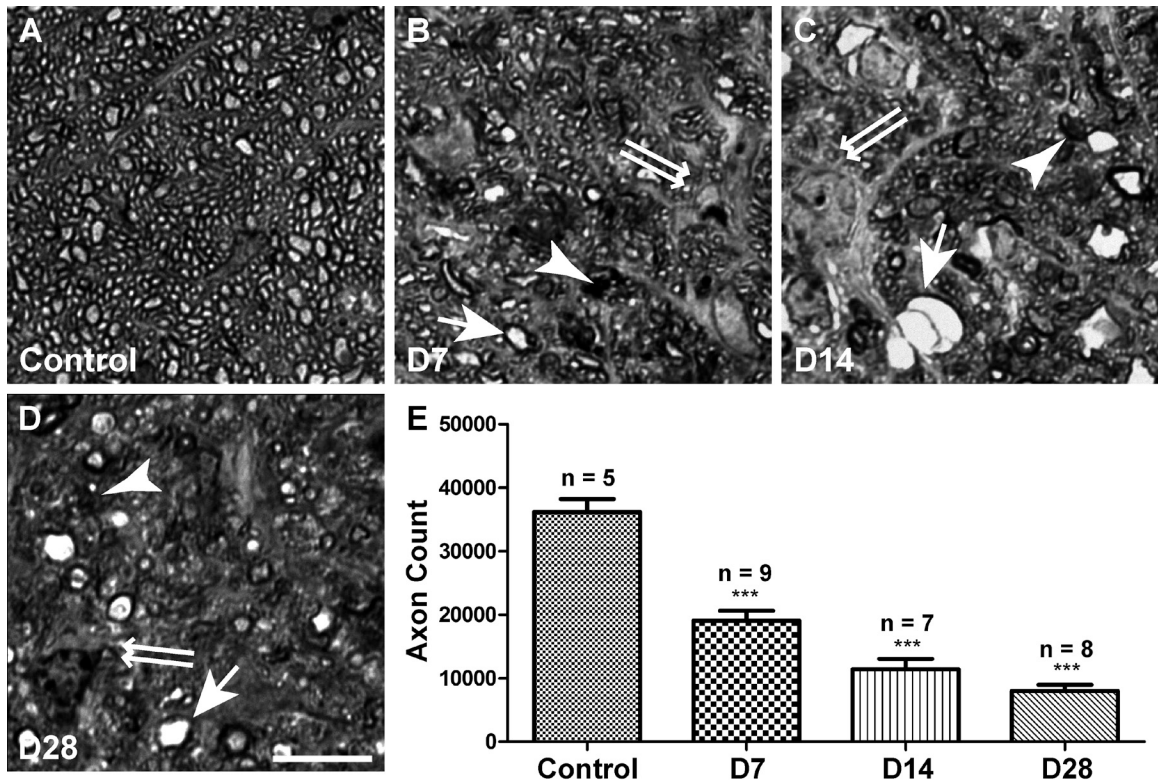


Figure 2-4. Axon degeneration in the myelinated optic nerve

(A-D) Representative images of PPD-stained optic nerve cross sections. Samples were collected from control (A) as well as experimental animals 7 days (B), 14 days (C) and 28 days (D) after laser treatment. Healthy axons had robust and uniform myelin ensheathment surrounding a clear axoplasm (A). Degenerating axons were marked by darkly stained axoplasm or myelin debris (arrowheads). Axon swelling (arrows) and gliosis (double arrows) were also frequently observed in experimental samples. (E) Quantification of total axon count on PPD-labeled sections. The mean axon number was reduced 7 days after laser treatment, and continued to decline at least until 28 days. Scale bar = 10 μ m. *** $p < 0.001$.

Axon Integrity in the Lamina and Pre-Lamina ONH

One major limitation of inbred mice with spontaneous glaucoma is the undefined onset of disease hindering the study of early disease pathology. Using experimental LIOH, we took advantage of the investigator controlled onset of IOP elevation to

examine changes occurring early in the disease process. As RGC axon damage particularly around the ONH region has been proposed to be a contributing factor for RGC death in glaucoma, we investigated how RGC axon integrity in this unmyelinated region may be influenced by laser treatment, especially at early time points. RGC axons were visualized using antibodies against the β -III subunit of tubulin and neurofilament (NF), two key structural components of the axon cytoskeleton. While the axon labeling pattern using the two antibodies were very similar, neurofilament labeling using SMI312 antibody resulted in visualization of the finer axonal processes with greater detail and was used to obtain higher magnification images.

The mouse ONH can be subdivided into the pre-lamina (at the level of retina) and lamina (at the level of sclera) regions⁴⁸. We employed different methodologies to best visualize the morphologies and trajectories of axons within these two regions. Longitudinal cryostat sections subjected to antibody staining (Fig. 2-5) were used to identify axonal changes within the lamina region (dotted bracket in Fig. 2-5A), while retinal whole-mounts (Fig. 2-6) were used to obtain the best visualization of the morphology and trajectories of RGC axons in the pre-lamina region (outlined as white circle in Fig. 2-6A). The morphological changes detected in the lamina and the pre-lamina regions, while initially similar in the first several days after laser treatment, ultimately became qualitatively different over the next 1-2 weeks as described below.

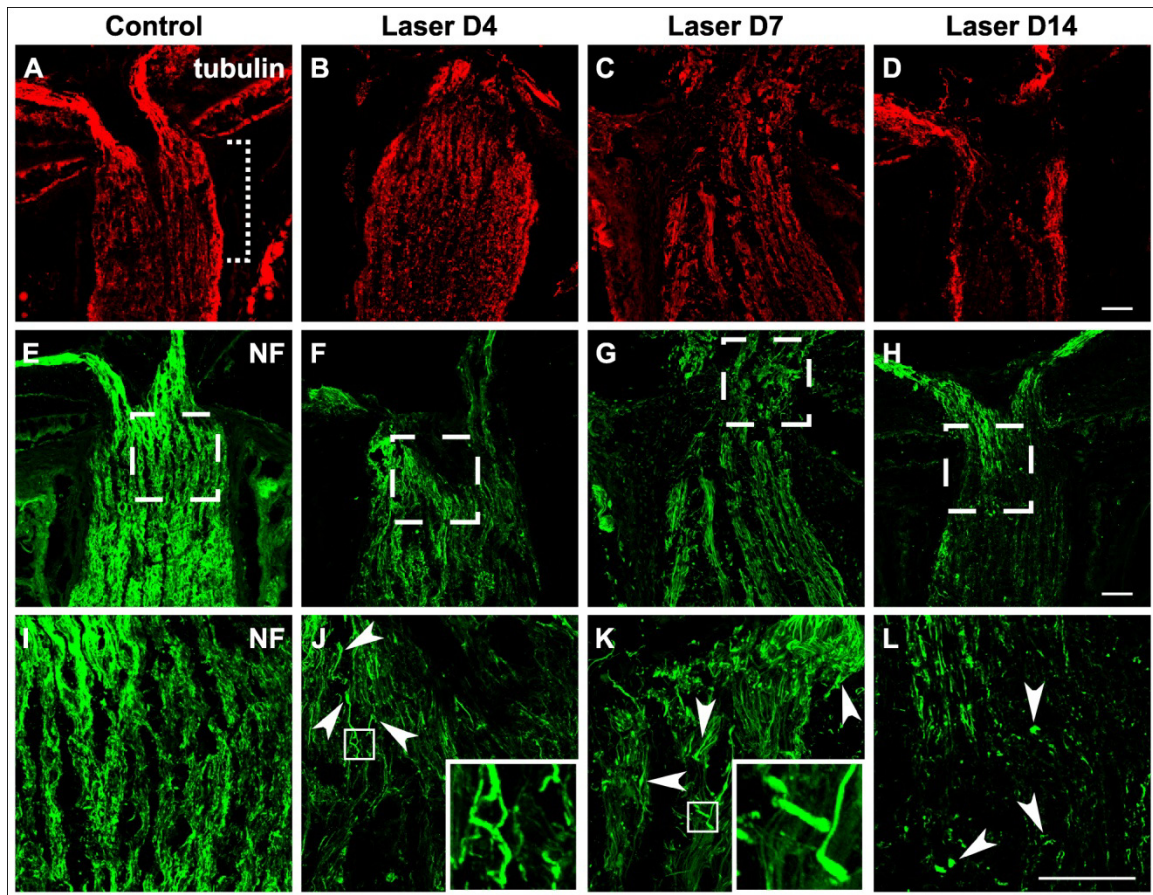


Figure 2-5. Early occurrence of axonal damage in the lamina ONH after laser treatment

Longitudinal cryosections through the ONH were immunostained for tubulin (A-D, red) and neurofilament (E-L, green). The retina is oriented towards the top of each image, and optic nerve towards the bottom. Dotted bracket (A) denotes the location of lamina ONH. Panels I-L correspond to boxed regions in E-H. The uniform staining pattern and parallel organization of axons seen in controls (A, E, I) were disrupted in laser-treated eyes (B-D, F-H, J-L). Pathological changes were observed as early as 4 days (B, F, J) following treatment and became more prevalent after 1 week (C, G, K). Axonal damage was initially manifested as localized enlargement (J, K, arrowheads) and undulating axon trajectory, examples of which are shown in the insets (J, K). The 2-week time point was marked by a loss of cytoskeletal immunoreactivity (D, H, L). Once-continuous axonal profiles were replaced with punctate degenerative debris (L, arrowheads) and regions devoid of axonal staining. Scale bar = 50 μ m. For tubulin staining between 3 and 8 animals were examined at each time point; for NF staining between 3 and 11 animals were examined.

Axon Degeneration in the Lamina ONH Occurs Early After Laser Treatment

In the control optic nerve lamina region, anti-tubulin and anti-NF immunostaining were uniform along the RGC axons (Fig. 2-5A, E, I). In contrast, in laser-treated eyes as early as 4 days after treatment, we observed a small number of axons at the lamina ONH region with localized enlargements (Fig. 2-5J, arrowheads and inset). Over the next few days, the overall staining pattern displayed more heterogeneity, with some axon segments showing intense immunoreactivity interrupted by patchy diminution of signal, consistent with a structural alteration in RGC axons (Fig. 2-5K). The axonal bundles normally aligned in parallel in this region also became distorted and undulating. By 2 weeks, the loss of cytoskeletal immunostaining was more widespread (Fig. 2-5D, H, L), reflecting a loss of intact axons. Concurrently, many small immunoreactive puncta were seen surrounding RGC axons, likely reflecting degenerated debris (Fig. 2-5L, arrowheads).

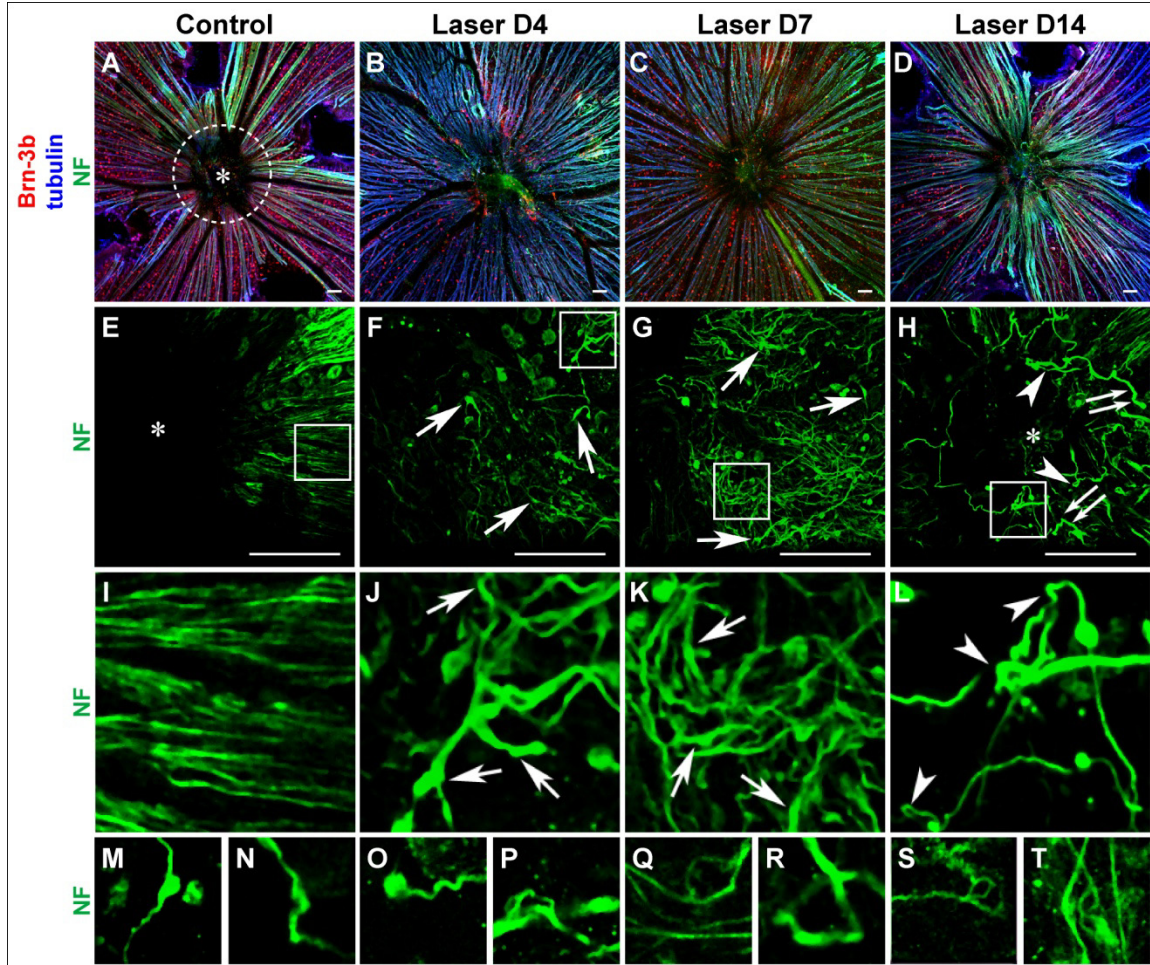


Figure 2-6. Aberrant axon trajectories at the pre-lamina ONH after laser treatment
 Low magnification images (A-D) of retinal whole-mounts immunolabeled with Brn-3b, tubulin and NF are presented to aid orientation and to correlate density of Brn-3b+ RGCs with axon pathology. Dotted white circle in (A) denotes the location of pre-lamina ONH. Defasciculation and localized enlargements (arrows) were observed on axons as early as 4 days after laser treatment (F, J), and continued to become more pronounced at 1 week (G, K). The meandering trajectories of aberrant axons (most apparent in J, K) appeared in stark contrast to the radial organization of RGC axons in control retina (E, I). At 2 weeks, numerous axons were observed to be disconnected and terminated in retraction bulbs (H, double arrows). The aberrant trajectories were heterogeneous and complex, and included twists, turns, and 180-degree loops (H, L, arrowheads). Ectopic axons were found at the center (asterisk) of the pre-lamina ONH (H), which was devoid of axonal staining in controls (E). A gallery exemplifying aberrant axon trajectories in additional retinal samples is shown in M-T. Scale bar = 50 μ m. n = 5 retinas for D4; n > 20 retinas for other time points.

Aberrant Axon Trajectories at the Pre-Lamina ONH

In control retinal whole-mounts, tightly packed axon bundles converged onto the ONH in an orderly radial fashion (Fig. 2-6E, I). Four days after laser treatment, focal enlargements appeared on axons in the pre-lamina ONH region (Fig. 2-6F, J, arrows), similar to those observed in the lamina ONH (Fig. 2-5). Of note, axonal changes in the pre-laminar region, unlike that found in the lamina also included defasciculation of axon bundles (Fig. 2-6J), with individual axons exhibiting aberrant turning trajectories, giving them the appearance of frayed ends of ropes. At 1 week, more axons exhibited enlargements (Fig. 2-6G, K, arrows), defasciculation, and meandering trajectories (Fig. 2-6K). The normal radially directed axon trajectories seen converging at the optic disc were instead replaced by a more randomly directed pattern. By 2-weeks, RGC axons that appeared to be disconnected from their distal portions and terminating in bulbous endings were frequently observed (Fig. 2-6H, double arrows). In addition, numerous axons exhibited tortuous terminal segment trajectories, including axon twisting, turning and even 180° axon loops (Fig. 2-6H, L, arrowheads). More examples of axons with aberrant trajectories are presented in Fig. 2-6M-T. While in control eyes, axons were not found in the central portion of the pre-lamina ONH (asterisk, Fig. 2-6A, E), aberrantly projecting axons were readily observed in the same region in laser-treated eyes (asterisk, Fig. 2-6H). These morphological changes and abnormal trajectories of RGC axons were similar to those encountered in glaucomatous eyes of DBA/2J mice (C.F., D.S., unpublished observation).

This analysis using antibody staining of axon cytoskeletal elements and confocal microscopy revealed that the earliest detectable signs of alterations in RGC axonal

integrity and trajectory occurred approximately 4 days after treatment. While the lamina and pre-lamina regions demonstrated no significant difference at this early time point, by 2 weeks the morphology of axons within these two regions appeared remarkably distinct. The lamina region was marked by axonal degeneration and buildup of debris. On the other hand, the pre-lamina region was characterized by aberrant axon trajectories, exemplified by twisting and looping. Such complex trajectories observed here were reminiscent of the sprouting and reactive plasticity of adult axons proximal to localized traumatic injury in the mouse optic nerve¹³⁹ as well as elsewhere in the CNS¹⁴⁰⁻¹⁴³. Our findings were thus consistent with a model in which an early insult to RGC axons occurs at the lamina ONH causing axon structural breakdown, followed by an initiation of a reactive plasticity-like response in the remaining axon proximal segment in the pre-lamina region. It is worth noting that the early signs of axonal pathology (day 4-7) occurred when RGC somas within the retina were still relatively preserved as shown by Brn-3b labeling (Fig. 2-6B, C), and preceded the decrease in Brn-3b⁺ RGC density that begins approximately 1 to 2 weeks after laser-treatment (Fig. 2-3).

Degeneration of Optic Nerve Myelin

Although axonal demyelination often results secondarily from CNS axon injury¹⁴⁴, demyelinating diseases such as multiple sclerosis can also be the cause of axonal degeneration¹⁴⁵. A recent study of laser-induced ocular hypertension in pigmented mice suggested that oligodendrocyte loss might precede significant RGC death¹¹¹. Here we examined myelin damage in the optic nerve following LIOH in CD-1 mice, and the

chronology of this event in relation to axonal injury. To detect early signs of myelin degeneration, we took advantage of the fact that the degradation of myelin basic protein unmasks an epitope (dMBP) that can be detected by a specific antibody, thus allowing identification of injured white matter¹⁴⁶⁻¹⁴⁷. In control optic nerves, the presence of myelin was clearly demarcated following immunolabeling of mature oligodendrocytes by CNPase (2',3'-Cyclic Nucleotide 3'-Phosphodiesterase) antibody (Fig. 2-7A). As expected there was no detectable signal following immunolabeling of dMBP (Fig. 2-7B). Likewise, in optic nerves from laser-treated eyes, dMBP was also not detectable in the first few days following treatment (Fig. 2-7E). However, beginning at 7 days after laser-treatment, dMBP could be readily identified and occurred primarily along the border of myelinated region with the unmyelinated ONH (Fig. 2-7H). At 2 weeks after laser-treatment, dMBP was detected further distal into the optic nerve (Fig. 2-7K). Higher magnification images (Fig. 2-7I, L, insets) demonstrated that the majority of dMBP immunoreactivity co-localized with cytoplasmic CNPase staining, confirming these degraded proteins were indeed of oligodendrocyte origin. Conversely, some dMBP immunoreactive structures were not found to overlap with CNPase, possibly reflecting oligodendrocyte processes in later stages of degeneration that have lost CNPase expression. Based on the earliest time of detection, alterations in RGC axon cytoskeletal structure at the ONH appeared to precede MBP degradation in the adjacent myelinated optic nerve.

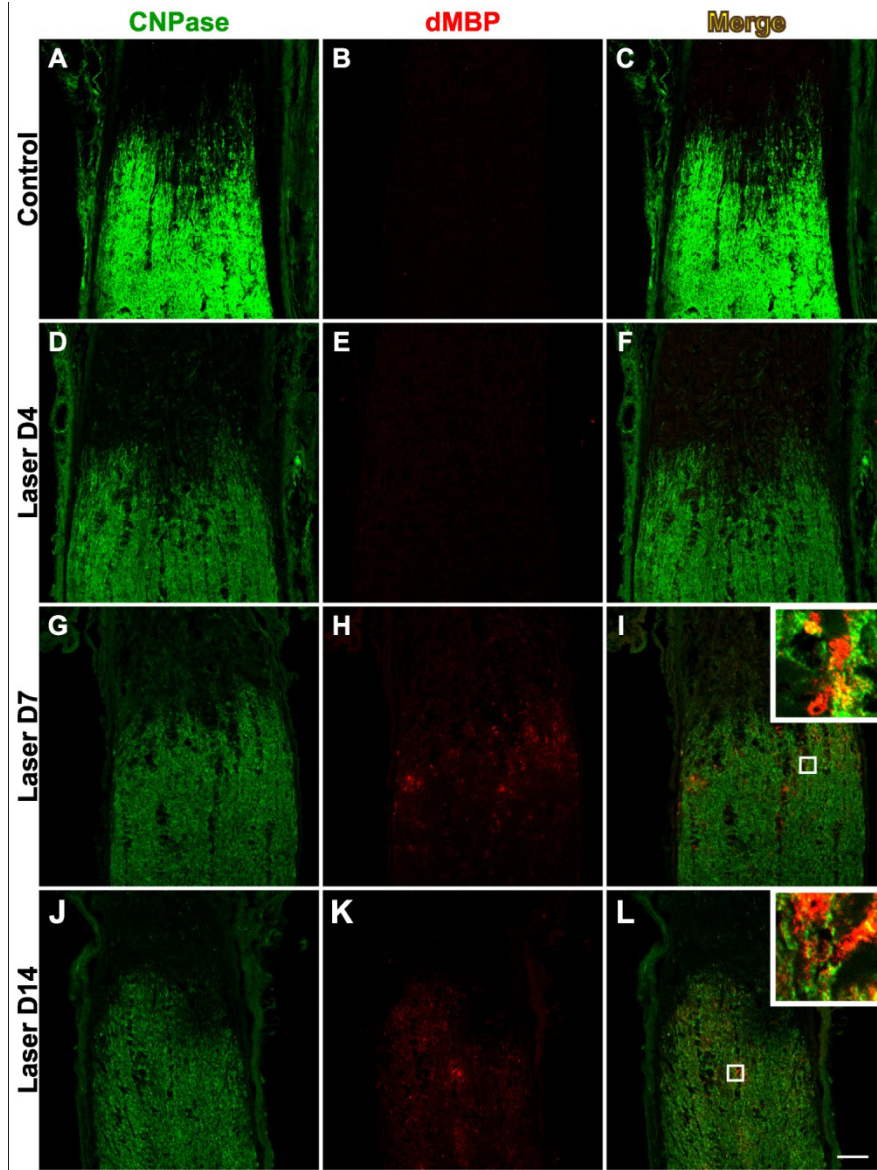


Figure 2-7. Detection of degraded myelin basic protein (dMBP) in the optic nerve
 Oligodendrocytes were labeled with the CNPase marker (A, D, G, J), and dMBP served as an indicator of myelin damage (B, E, H, K). In the control optic nerves (B) and those harvested 4 days (E) after laser treatment, no specific immunoreactivity of dMBP was detected. At day 7, dMBP appeared primarily along the border of myelinated optic nerve with the unmyelinated ONH (H). After 2 weeks, the presence of dMBP could be identified further distal into the optic nerve (K). Merged images of CNPase and dMBP labeling are shown in C, F, I, L, with the insets highlighting examples of both earlier stages of myelin degeneration characterized by co-localization of dMBP (red) and CNPase (green) in oligodendrocytes, and later stages of myelin degeneration often characterized by the presence of dMBP alone. Scale bar = 50 μ m. n = 3 sets of experiments.

Discussion

We demonstrated that IOP elevation can be induced in albino CD-1 mice by laser photocoagulation. Specific damage to RGC somas as well as to RGC axons was observed, while other retinal layers were not significantly affected, consistent with the characteristic pathology of glaucoma. By taking advantage of the defined induction of IOP elevation, we have placed a number of important pathological changes in CD-1 LIOH in a rough temporal sequence. Our results demonstrated that the earliest detected morphological changes in RGC axons occurred at the ONH by day 4 and consisted of localized axonal enlargements and undulating axon trajectories, followed progressively over the next 2 weeks by the accumulation of axonal debris in the lamina region, and aberrant axon trajectories in the pre-lamina region. These early signs of ONH axonal damage substantially preceded evidence of myelin injury (beginning at 7 days) and RGC degeneration (at about 2 weeks), as manifested by the down-regulation of Brn-3b and/or death of Brn-3b⁺ cells within the retina.

Selective RGC Damage After LIOH in CD-1 Mice

The hallmark of glaucomatous disease is the selective damage to and loss of RGCs with relative sparing of other retinal cell types. Several lines of evidence from the present study support the notion that LIOH in CD-1 mice triggers a similar pattern of RGC loss. Brn-3b staining of whole-mounted retina indicated loss of immunoreactive cells over 4 weeks, suggesting progressive degeneration of RGCs. Histological examination of sagittal retinal sections revealed a 33% reduction of cell density in the

GCL, where RGC cell bodies reside. In addition, morphometric analysis showed that the thicknesses of other retinal layers were not affected, arguing against global ischemia. Axon degeneration characteristic of glaucomatous injuries also occurred, as demonstrated by axon counting in PPD-stained optic nerve.

Comparison to Other Animal Models of Glaucoma

While monkeys^{116,124} and rats^{62,117,120,122} have been successfully induced to develop glaucoma, mouse models afford the additional advantages of cost-effectiveness and amenability for genetic manipulation. To date, a number of experimental glaucoma models have been reported in mice, including laser photocoagulation¹¹¹⁻¹¹⁴ and episcleral vein cauterization¹²¹. Compared to these models, LIOH in albino CD-1 offers potential advantages in terms of the accelerated time course and pronounced RGC damage. One study in C57BL/6 mice reported 28% RGC loss at 2 weeks¹¹¹, while another in NIH Black Swiss mice demonstrated 63% axon loss at 12 weeks¹⁴⁸. In contrast, CD-1 mice exhibited 42% reduction of Brn-3b⁺ RGCs at 2 weeks, and 78% reduction of myelinated axons at 4 weeks after LIOH.

It should be noted that since Brn-3b is downregulated in glaucomatous retinas⁶⁰⁻⁶¹, the loss of Brn-3b immunoreactivity alone cannot be concluded as RGC loss. Instead, recent studies⁶⁰⁻⁶¹ interpret the reduction of RGC gene expression as a sign of degeneration, which is expected to mark a disease state preceding cell death itself. In the present study, significant axon degeneration (47%) in the myelinated optic nerve had already occurred 1 week after laser treatment, when loss of Brn-3b⁺ RGC somas was not

yet prevalent. This observation agrees with previous reports that axon injury preceded RGC soma death^{48,60-61,138}. At 2 weeks, both RGC axon and soma count were significantly diminished (68% and 42%, respectively). By 4 weeks, axon number was reduced by 78%, whereas linear cell density in the GCL only suffered a 33% reduction. This may appear inconsistent at first glance; however, a substantial proportion of surviving cells in the GCL is expected to be displaced amacrine cells. Assuming amacrine cells accounted for 40-60% of the GCL cell population^{91,133-135}, and that they were not damaged by experimental glaucoma, the reduction of linear RGC density is estimated to be between 55% and 80% at 4 weeks. On the other hand, a 91% decrease of Brn-3b⁺ cells was observed, possibly reflecting downregulation of this protein in some surviving RGCs. In summary, by any of the three measures employed in this study, the level of RGC injury induced by LIOH is clearly more severe in CD-1 mice compared to pigmented mice.

Characteristics of IOP Elevation in CD-1 LIOH

While the accelerated time course of RGC damage in CD-1 LIOH is advantageous in speeding up experimental analysis, it is necessary to bear in mind that this model is more acute compared to DBA/2J and human glaucoma, and could potentially involve different underlying mechanisms. While the disease present in DBA/2J mice models pigmentary glaucoma, LIOH in CD-1 resulting from an acute blockage of fluid outflow may resemble angle-closure glaucoma more closely. Another major difference from existing published models is the transitory nature of IOP elevation

in CD1 LIOH. IOP rose briefly from a baseline of 12-13 mm Hg to 27-29 mm Hg, and returned to normal between 2 and 7 days after treatment. In our initial attempts at model development, we performed photocoagulation for a full 360° circumferentially around the eye, without avoiding the long posterior ciliary arteries. This treatment protocol typically resulted in acute IOP spikes of > 70 mm Hg within 12 hours of laser treatment that could lead to ischemic changes, and was thus abandoned. Translimbal laser treatment of 270-300° instead of 360° with the avoidance of long posterior ciliary arteries helped to eliminate acute pressure spikes post-operatively. Repeated laser treatments to extend the period of IOP elevation were not consistently effective, and frequently led to substantial additional ocular inflammation. The resulting corneal edema and scarring may then lead to false readings of elevated IOP. Although our laser treatment paradigm only resulted in a transient doubling of IOP for several days, this change in IOP in CD-1 mice was nevertheless sufficient to trigger highly reproducible morphological changes in RGCs and their axons that mimic findings in glaucoma. Although IOP declined to baseline by 1 week, glaucomatous disease clearly progressed beyond that time point. This model therefore offers an opportunity to delineate pathophysiological mechanisms that can operate independently of sustained pressure elevation, which may have relevance to human cases with progressive worsening of glaucomatous disease despite IOP-lowering intervention¹⁴⁹.

Axon Reactive Plasticity in the Pre-Lamina ONH

The aberrant looping trajectories of RGC axons in the pre-lamina ONH are strikingly reminiscent of the sprouting and reactive plasticity of adult RGC axons injured by optic nerve crush¹³⁹. While axonal sprouting has been described following other CNS lesions^{140,142-143} as well as in Alzheimer's disease¹⁵⁰⁻¹⁵¹, aberrant growth of RGC axons in glaucomatous animals has not been previously appreciated. This RGC axon re-growth phenomenon may not be limited to mice, as recent work in a rat laser-induced model of glaucoma has identified a similar phenomenon (N. Marsh-Armstrong, personal communication). Axonal reactive plasticity in the pre-lamina region is most consistent with damage occurring more distally along the axons within the lamina region, and agrees with previous reports in DBA/2J mice^{48,60} identifying the lamina ONH as an initial site of glaucomatous injury. The ultimate fate of RGC axons that exhibit these aberrant trajectories is unknown, although their presence clearly demonstrates the ability of adult axons to maintain a limited growth/remodeling program. In the setting of glaucoma, it would be of interest to examine whether such axons exhibiting reactive plasticity are also present in human glaucomatous eyes and to identify the mechanisms underlying this form of plasticity.

Axonal Damage as an Early Manifestation of Disease

As the onset of IOP elevation in LIOH is controlled by the investigator, this mouse model offers an opportunity to delineate the timing of some pathological events that ultimately result in RGC loss. A finding from this study is the early onset of ONH axon degenerative changes and reactive plasticity after LIOH. Morphological alterations

of axons in the ONH preceded significant degeneration of myelin and RGC somas. These findings indicated that studies of the molecular nature of insults to RGC axons at the ONH and the intra-axonal response mechanisms may provide useful insight into disease. It is important to bear in mind a careful analysis of changes that may occur in the retina was not performed in the present study, and our results do not address the question whether there may also be early events that impact the dendritic and somatic compartments of RGCs that are either independent or related to RGC axonal changes occurring at the ONH. Nevertheless, the evidence of specific early RGC axon responses at the ONH indicates that the study of these events may be fruitful avenues for better understanding glaucoma pathophysiology. In addition, axonal responses to glaucomatous injury could serve as an early readout of the effectiveness of new therapeutic strategies.

Chapter 3

The Role of EphB/ephrin-B Signaling in Experimental Glaucoma

Abstract

Interaction between Eph receptors and ephrin ligands has been well-established to play important roles in wiring the developing nervous system. Growing evidence in recent years suggests that these signaling proteins traditionally known as “axon guidance” molecules are also involved in modulating axonal response to injuries in adulthood. Using the LIOH model in CD-1 mice described in Chapter 2, I demonstrate that upregulation of *EphB/ephrin-B* expression occurs early within a day of IOP elevation. A transient increase of phosphorylation-dependent ephrin-B (pEB) reverse signaling is observed in ONH axons, microglia, and some astrocytes. Morphologically unaffected RGC axons differ from axons with reactive aberrant trajectories by exhibiting increased pEB activation, while pEB levels in morphologically affected axons are comparable to controls. Genetic deficiency of EphB2 or EphB3 causes more severe axonal degeneration in mutant mice treated with LIOH compared to wild-type, while the C-terminal truncation of EphB2 has an intermediate effect. These results indicate that an Eph-ephrin signaling network is activated at the ONH after LIOH in CD-1 mice, either prior to or coincident with the initial morphological signs of RGC axon damage reported previously. Forward as well as reverse signaling confers protection to RGC axons against glaucomatous injury.

Introduction

Potential of Contact-dependent Signaling in Glaucoma

The role of glial activation has been investigated extensively in the context of glaucoma^{77,84}. Many studies demonstrated secretion of diffusible factors by astrocytes or microglia of the glaucomatous ONH, which may play either supportive¹⁵² or detrimental roles^{9,69,111,153} with respect to RGC axons. However, direct cell-cell interaction mediated by membrane-anchored signaling complexes has not been explored in detail. In mouse ONHs, the lack of myelination allows for tight apposition of RGC axons with neighboring glia. Analysis of the morphology and spatial arrangement of ONH astrocytes reveals that these cells form closely-packed “glial tubes” that ensheath axon bundles^{48,58}. It would be of interest to examine how direct cellular interactions modulate the process of axonal degeneration in glaucoma.

Previous work in our lab has linked specific upregulation of *Eph* and *ephrin* signaling molecules in ONH glia to the presence of RGC axon damage in DBA/2J glaucomatous mice¹²⁸. In light of recent evidence implicating the Ephs and ephrins in CNS injury, these contact-dependent signaling proteins emerge as attractive candidates that could mediate axon-glia and axon-axon communication in response to glaucomatous insults.

The Eph and ephrin Protein Families

Eph proteins constitute a large family of receptor tyrosine kinases that bind to ligands called ephrins¹⁵⁴⁻¹⁵⁶. The Eph and ephrin protein families are each divided into A and B subclasses based on sequence homology, membrane anchorage, and binding preference for each family member. There are 10 EphA and 6 EphB receptors known at present, while 6 ephrin-A and 3 ephrin-B proteins have been identified. Ephrin-A proteins are attached to the cell membrane by a glycosylphosphatidylinositol (GPI) anchor, while ephrin-B proteins have a transmembrane region and a short, highly conserved cytoplasmic tail with a PDZ (postsynaptic density-95/Discs large/zona occludens-1)-binding domain¹⁵⁷⁻¹⁵⁹. Eph receptors consist of a highly conserved N-terminal extracellular ligand binding domain, followed by a cysteine-rich domain, two fibronectin III repeats, a juxtamembrane region, and an intracellular kinase domain with a PDZ binding motif^{157,160}.

Diverse Eph/ephrin Functions in Development and Adulthood

In the nervous system, Ephs and ephrins have been most extensively studied for their developmental roles in axon guidance, cell adhesion, neuronal migration, and pattern formation¹⁶¹⁻¹⁶². One of the most well-established examples is topographical mapping of RGC axons within the optic tectum (in chicken and frog) or superior colliculus (SC; in mammals). EphA proteins are expressed along the nasal-temporal axis in the retina in a gradient complementary to ephrin-A expression along the anterior-posterior (A-P) axis of tectum/SC. Temporal axons express the highest levels of EphA, which makes them most sensitive to the inhibitory properties of ephrin-A in the

tectum/SC. Since the ephrin-A gradient is organized with the highest level in the posterior pole¹⁶³, RGC axons from temporal retina project to the anterior part of the target, while RGC axons originating from nasal retina project posteriorly. The reliance of retinotectal mapping on the expression of EphA and ephrin-A proteins in complimentary gradients has been verified in studies where levels of EphA/ephrin-A protein expression were experimentally perturbed¹⁶⁴⁻¹⁶⁵. In addition, complimentary gradients of EphB and ephrin-B have been demonstrated to mediate retinotectal mapping along the dorsal-ventral (D-V) axis¹⁶⁶⁻¹⁶⁸. Another visual target, the lateral geniculate nucleus (LGN), also depends on Eph/ephrin gradient for topographic mapping¹⁶⁹⁻¹⁷⁰. The general strategy of Eph/ephrin proteins as graded position cues appears to hold true for the connection between thalamic nuclei and cortical areas for specific sensory modalities, including mapping from LGN to visual cortex¹⁷¹, as well as thalamocortical/corticothalamic projections between ventrobasal complex and somatosensory cortex¹⁷²⁻¹⁷⁴. Furthermore, analogous mechanisms have been implicated in establishing vomeronasal¹⁷⁵, hippocamptoseptal¹⁷⁶⁻¹⁷⁷ and auditory circuits¹⁷⁸⁻¹⁸⁰.

However, Ephs and ephrins are not merely developmental molecules. They also have significant functions in the adult nervous system. Compelling evidence has ascribed to Eph/ephrin signaling many essential roles in regulating synaptic structure and plasticity. The widespread patterns of Eph and ephrin expression in the developing nervous system are down-regulated in the adult except in regions of the CNS that continue to undergo extensive renewal and remodeling such as the hippocampus, olfactory system and subventricular zone (SVZ)¹⁸¹. Evidence points to a role for Eph and ephrins in modulating synaptic function via the regulation of dendritic spine formation¹⁸²⁻

¹⁸⁴, NMDA receptor clustering and potentiation of calcium influx¹⁸⁵⁻¹⁸⁶. Eph and ephrin function has also been implicated in long term potentiation (LTP) in both Schaffer collateral-CA1 and mossy fiber-CA3 synapses¹⁸⁷⁻¹⁹⁰, as well as in the modulation of synaptic efficacy between nociceptive afferents and spinal cord dorsal horn neurons, leading to NMDA receptor-dependent hyperalgesia¹⁹¹. Another intriguing function that has emerged in recent years is the involvement of both A and B Eph/ephrin proteins in the proliferation and survival of adult neural progenitor cells in neurogenic regions. Besides regulating brain size by controlling apoptosis of embryonic cortical progenitors¹⁹², Eph/ephrin signaling also modulates neurogenesis in the adult SVZ, where new neurons continue to be born. The mechanism is complex, as both positive¹⁹³ and negative¹⁹⁴⁻¹⁹⁶ effects on SVZ progenitor proliferation and apoptosis have been reported, involving either forward or reverse signaling. A promotion of neuronal fate has also been documented *in vitro*^{193,197}.

In addition, Eph and ephrin families are used by cells outside of the nervous system in both health and disease. ephrin-B2 on arterial and EphB4 on venous endothelial cells mediate embryonic vascular assembly and arteriovenous differentiation¹⁹⁸⁻¹⁹⁹. In adulthood, ephrin-B2 and EphA2 have also been linked to neovascularization and tumor angiogenesis²⁰⁰⁻²⁰⁴. Many Eph/ephrin family members are found in tumors including those of the breast, lung, colon, prostate, and in glioblastoma as well as melanoma²⁰⁵, where their levels of expression to some degree correlate with malignancy. It is thought that Eph/ephrin promotes tumor metastasis by negatively regulating cell adhesion and enhancing neovascularization²⁰⁶⁻²⁰⁷.

Features of Eph/ephrin Signaling

One of the most intriguing aspects of Eph/ephrin biology is the existence of bidirectional signaling upon protein binding²⁰⁸. Ephrin binding to Eph causes autophosphorylation of the Eph tyrosine kinase domain and triggers signaling cascades that may involve Ras and Rho²⁰⁹⁻²¹¹. By convention, this activation of Eph proteins is known as forward signaling. However, EphB proteins binding to ephrin-B proteins can also trigger the phosphorylation of tyrosine residues in the ephrin-B cytoplasmic domain²¹²⁻²¹³. By convention, this type of signaling resulting from Eph proteins acting as “ligands” and ephrins serving as “receptors” is called reverse signaling. Even though ephrin-A proteins do not have an intracellular domain, they can also participate in reverse signaling^{175,214-215}. The bidirectional nature of Eph/ephrin signaling represents a highly efficient mechanism for cell-to-cell communication.

Ephrin-A proteins preferentially bind to the EphA subclass, while ephrin-B proteins bind to the EphB subclass²¹⁶. Interactions between Eph and ephrin proteins of the same A or B subclass are promiscuous in that ephrin-A ligands can bind to any EphA receptor, and ephrin-B ligands can bind to any EphB receptor, albeit with varying degrees of affinity²¹⁷. Binding between subclasses is also observed in the form of EphA4 binding to ephrin-B proteins²¹⁸, and ephrin-A5 binding to EphB2²¹⁹.

Co-expression of ligands and receptors in *cis* is another unusual feature of the Eph/ephrin system. Analysis of the developing visual system demonstrated that *cis* interactions do occur within the same axon between Ephs and ephrins, and that this interaction appeared to be of functional significance. Over-expression of ephrin-As on

RGC axons, to maximize the opportunity for *cis* interactions between EphA and ephrin-A, resulted in desensitization of the normal axonal avoidance response to ephrin-A²²⁰. On the other hand, reciprocal silencing of co-expressed EphA and ephrin-A molecules did not occur in spinal motor axons, possibly because the proteins were segregated to distinct membrane micro-domains²²¹.

Eph/ephrin in CNS Injury

In recent years, a sizable body of evidence has documented the expression of Eph and ephrins after CNS damage in the brain²²²⁻²²³, optic nerve¹³⁹, and spinal cord²²⁴⁻²²⁸. Following spinal cord transection, hemisection, or contusion, EphB2, EphB3, Eph A4, ephrin-B2 have been identified at the lesion site by in situ hybridization, and to a more limited extent by immunolabeling^{224-226,228}. Similarly, optic nerve crush injury results in the local expression of EphB3 at the site of injury¹³⁹. The expression of Ephs and ephrins occurs as early as 2-3 days after injury¹³⁹ and may continue for up to 14-18 days^{139,224}. The temporal pattern of Eph and ephrin expression is consistent with these molecules playing a role in a multitude of pathological processes.

Two key studies used transgenic mice to demonstrate the important functions of Eph/ephrin signaling in modulating axonal and/or glial responses in CNS injury. After spinal cord hemisection, damaged corticospinal tract axons express EphA4 and are surrounded by astrocytes expressing ephrin-B2. Experiments using EphA4 knockout mice²²⁹ showed that EphA4-deficient axons crossed the lesion site in greater numbers than in wild-type controls, and the animals exhibited a higher degree of functional

recovery. In addition, reactive astrocytic response was dampened by EphA4 deletion, and the glial scar was reduced in size. Therefore, EphA4 could impede spinal cord axonal regeneration either by sensing repulsive cues, or by mediating the formation of glial scar. In optic nerve crush injury, EphB3 was found to be upregulated by macrophages at the lesion site. Injured RGC axons in EphB3 null mice exhibited a reduced sprouting response, suggesting that EphB3 promotes RGC axonal plasticity and initial axon attempts at re-growth after injury¹³⁹.

Investigating Eph/ephrin Signaling in Mouse Glaucoma

We previously demonstrated that *EphB2* and *ephrin-B2* upregulation was tightly associated with RGC axon pathology in DBA/2J mice, and was not detected in age-matched non-glaucomatous animals. However, the functional consequence of this mRNA upregulation has not been addressed. It also remained unclear whether *Eph* and *ephrin* upregulation is a fundamental feature of glaucoma across animal models, and how the spatial and temporal characteristics of Eph/ephrin signaling relate to pathologies of RGCs and their axons.

To better understand the potential role of Eph/ephrin signaling in glaucoma, we have undertaken a detailed analysis of *Eph/ephrin* expression, signaling activation, cellular origin, and functions, using the laser-induced ocular hypertension (LIOH) mouse model described in Chapter 2. In this model, the onset of IOP elevation is under investigator control, thus allowing examination of the early pathological events that impact RGCs and their axons. In mice subjected to LIOH, similar to DBA/2J mice, an

early morphological sign of glaucomatous damage is observed in RGC axons at the ONH. After laser treatment, axon response/damage at the ONH is present by 4 days, and by 7 days, two morphologically distinct populations of RGC axons can be observed. One population has yet to exhibit overt morphological responses to glaucomatous damage and appears as structurally intact, straight axons through the ONH. The second population consists of axons that have already lost a distal segment and exhibit reactive plasticity characterized by abnormal looping and meandering trajectories of the proximal segment. While all RGC axons at the ONH are potentially exposed to glaucomatous damage, the presence of these two clearly recognizable axon populations offers an opportunity to identify events specifically occurring within RGC axons early in the injury process prior to overt morphological responses.

In the present study, we describe *EphB/ephrin-B* mRNA upregulation and the presence of an ephrin-B reverse signaling network involving axons, microglia, and astrocytes at the ONH during early stages of disease. We further demonstrate that ephrin-B signaling was preferentially associated with RGC axons that have yet to exhibit morphological evidence of damage, but is down-regulated in RGC axons at later stages of injury that have responded with reactive plasticity changes including aberrant trajectories in the pre-lamina ONH region. Using mouse mutants deficient in EphB2 or EphB3, we provide functional evidence that EphB/ephrin-B signaling promotes axon survival in experimental glaucoma.

Materials and Methods

Animals

CD-1 mice used in the first part of the study were purchased from Charles River Laboratories (Wilmington, MA). The generation of *EphB2*^{-/-230}, *EphB2*^{lacZ/lacZ230} and *EphB3*^{-/-231} mice has been described previously. Mutant mice were generous gifts from Dr. Mark Henkemeyer from University of Texas, and were maintained on a CD-1 background.

Laser-Induced Ocular Hypertension (LIOH)

LIOH on CD-1 mice was performed using the procedures outlined in Chapter 2.

Cryostat Section Preparation

Mice were anesthetized with an overdose of pentobarbital and perfused transcardially with 4% paraformaldehyde (PFA) in 0.1 M phosphate buffered saline (PBS, pH 7.4). Eyes were enucleated along with a segment of retrobulbar optic nerve attached. The anterior segment, lens and vitreous were dissected away from the eye cup, consisting of the retina and optic nerve. The eye cups were then immersion-fixed in the same fixative at 4°C overnight, cryoprotected with 30% sucrose, and embedded in Tissue-Tek optimal cutting temperature (OCT) compound (Sakura Finetek, Torrance, CA).

Cryosections 10 μm in thickness were cut along the longitudinal axis through the ONH, mounted on Super Frost Plus slides (Fisher Scientific, Springfield, NJ), and subjected to either immunostaining or *in situ* hybridization. For *in situ* hybridization, DEPC-treated PBS was used for all steps during sample processing to maximize preservation of RNA integrity.

Immunohistochemistry

Immunohistochemical studies were performed as previously described.²³² Briefly, cryosections were washed with 0.1 M PBS and blocked with 10% normal donkey serum (NDS) for 30 minutes at room temperature. For most experiments, tissue permeabilization was achieved by inclusion of 0.1% Triton X-100 in the blocking solution. For detection of phospho-ephrin-B, however, Triton X-100 was omitted because detergent treatment had the tendency to extract this antigen from the membrane or cause its lateral dispersion, resulting in a diminution of punctate staining. Tissue sections were instead permeabilized by incubation with methanol containing 20% DMSO for 30 minutes at room temperature. After primary antibodies were incubated overnight at 4°C followed by PBS washes, secondary antibodies were applied for 1 hour at room temperature. Slides were counterstained with 4',6-diamidino-2-phenylindole (DAPI) to label nuclei when appropriate, and mounted in 97% 2,2'-thiodiethanol (TDE; Sigma, St. Louis, MO).

The following primary antibodies were used: rabbit anti-tubulin β -III (1:500; Sigma, St. Louis, MO), mouse anti-neurofilament (SMI312; 1:500; Covance Research

Products, Denver, PA), rat anti-glial fibrillary acidic protein (GFAP; 1:200; Zymed, South San Francisco, CA), rabbit anti-S100 (1:200; Sigma, St. Louis, MO), rabbit anti-Iba-1 (1:50; Wako Chemicals USA, Richmond, VA), rabbit anti-NG2 (1:400; Chemicon, Temecula, CA), rabbit anti-phospho-ephrin-B (1:100; Cell Signaling Technology, Beverly, MA), rat anti-CD11b (1:50; Serotec, Indianapolis, IN). Multi-color labeling was accomplished with secondary antibodies conjugated to tetramethyl rhodamine (TMR; 1:200; Invitrogen, Carlsbad, CA) or cy3, cy2, and cy5 (1:200; Jackson ImmunoResearch, West Grove, PA). Confocal microscopy was performed on an LSM5 Pascal microscope (Carl Zeiss Meditec, Inc., Thornwood, NY) as previously described²³².

***In situ* Hybridization**

Digoxigenin-labeled RNA probes specific for EphB2, EphB3, ephrin-B1, ephrin-B2 and ephrin-B3 were prepared as previously described²³³. Probe hybridization was carried out at 60 °C overnight, and detected with fluorescence microscopy following application of the TSA-plus fluorescein system (PerkinElmer Life Sciences, Wellesley, MA). Since EphB2, EphB3, and ephrin-B3 demonstrated the most robust and reproducible upregulation, we focused our analysis using these probes. To identify the cellular origin of mRNAs, fluorescence in situ hybridization was followed by immunohistochemistry with cell type-specific antibody markers.

Real-time Polymerase Chain Reaction

The ONH region was dissected from laser-treated and contralateral control eyes. Total RNA was isolated using Qiagen RNeasy Micro Kit (Valencia, CA). The amount of RNA was measured using ND-1000 UV-Vis Spectrophotometer (NanoDrop Technologies, Wilmington, DE). At least 50 ng RNA was reverse-transcribed into cDNA using BioRad iScript Select cDNA Synthesis Kit. Sequence-specific primers for extracellular domains of mouse *EphB2*, *EphB3* and *ephrin-B3* were designed by Primer3 (www.primer3.com) and synthesized by Integrated DNA Technology (Coralville, IA). The following primer sequences were used to amplify *EphB2*, *EphB3*, and *ephrin-B3*, respectively: forward 5'-GAT GGT ACA TCC CCC ATC AG-3', reverse 5'-ACG CAC CGA GAA CTT CAT CT-3'; forward 5'-GCT GGT GAG TTT GGG GAA GTG-3', reverse 5'-GTG ACC CCA ATC CTT AGC AG-3'; and forward 5'-GAC GGC GGG CCA AGC CTT CGG AGA G-3', reverse 5'-ATA GCC AGG AGG AGC CAA AGA G-3'. Glyceraldehyde-3-phosphate dehydrogenase (*GAPDH*) was used as a reference gene to normalize the level of mRNA expression of *EphB2*, *EphB3* and *ephrin-B3*. Sequence-specific primers for mouse *GAPDH* were: forward: 5'-GCA CAG TCA AGG CCG AGA AT-3', reverse: 5'-GCC TTC TCC ATG GTG GTG AA-3'. Real-time PCR was performed with iCycler system MyiQ following the manufacturer's protocol (Bio-Rad). Briefly, cDNA and 1mM MgCl₂ were mixed with iQ SYBR Green Supermix in a total volume of 20 µl. The thermo cycle was 95°C for 3 minutes followed by 40 cycles at 95°C for 10 seconds and 60°C for one minute. Real-time PCR was performed in triplicates. Melting-curves were created to verify the specificity of the product. The melting curve was established at 95°C for 1 minute followed by 55°C for 1 minute with 0.5°C increments for 80 cycles. Serial dilutions were run for *GAPDH* to generate standard

curves for each sample. PCR products were confirmed on 2% agarose gel. Data was obtained with MyiQ Optical System software (BioRad Hercules, CA). Since the expression of *EphB/ephrin-B* mRNAs was most concentrated in the ONH region based on *in situ* hybridization findings, a correction was performed to exclude the dilution effect on mRNA signals from the myelinated optic nerve segment carried over during dissection. Briefly, a dilution factor (DF) was calculated by dividing the total RNA of each sample by the amount of RNA used for quantitative PCR. A corrected Ct value was obtained by applying formula $Ct(\text{corrected}) = Ct(\text{read}) - \text{Log}(\text{DF})/\log E$, where E was the amplification efficiency. The corrected Ct was further normalized to *GAPDH* from the same sample. The relative expression levels of *EphB2*, *EphB3* and *ephrin-B3* in experimental eyes were compared to contralateral untreated eyes by using the Pfaffl method²³⁴.

Quantification of Phosphorylated ephrin-B (pEB) Expression

On whole-mounted retinas, one image from each quadrant adjacent to the optic disc was acquired using the 63x oil immersion lens on a confocal microscope. Fluorescent labelings of neurofilament (NF) and pEB were assigned to the green and red channel, respectively. Quantification was carried out using Photoshop CS2 (Adobe). First with the red channel masked, the green channel (NF) was used to visualize axon profiles and guide selection of regions of interest (ROIs). In each LIOH retina, three aberrant axon segments that deviated from the normal radial course were outlined and defined as ROIs. Within these “aberrant” ROIs, the mean fluorescent intensity in the red channel

representing pEB was then quantified. Morphological normal axons were tightly bundled, making it difficult to outline individual axons. The same ROI shapes used for aberrant axons in the same retina were therefore loaded, and overlaid on healthy axon bundles to quantify their mean pEB intensity. Similarly, pEB levels in the contralateral control retina were determined with the same set of ROIs as its partner experimental eye. This protocol ensured that comparable sizes were analyzed for each condition (Control, Laser Normal, and Laser Aberrant) in a pair of retina from the same animal. Fluorescence intensities in each retinal pair were then averaged and normalized by the value of Control. Six pairs of retinas were analyzed at 7 days after laser photocoagulation, because this represented the earliest time point at which reactive plasticity was consistently and robustly present.

Statistical Analysis

The RT-PCR results were analyzed by two-way analysis of variance (ANOVA), followed by post hoc Bonferroni multiple comparison test. The pEB quantification data were subjected to one-way ANOVA followed by Tukey's multiple comparison test. Statistical tests were performed using the GraphPad Prism (version 5) software, with a significance level set at $p < 0.05$. Values were reported as mean \pm SEM.

Results

Upregulation of *Eph* and *ephrin* mRNAs at the Laser-Treated ONH

In a previous study in the DBA/2J inbred strain of glaucomatous mice¹²⁸, we identified a number of *EphB* and *ephrin-B* genes at the ONH whose specific upregulation appeared to be highly correlated with the presence of RGC axon loss. In the present study, we used fluorescent *in situ* hybridization (FISH) to determine whether *EphB* and *ephrin-B* genes were likewise upregulated after laser-induced experimental ocular hypertension in CD-1 mice. The results showed that *EphB2*, *EphB3*, and *ephrin-B3* mRNAs were consistently upregulated at the ONH following laser treatment, compared to a modest level of baseline expression in controls (Fig. 3-1). A few other family members including *ephrin-B1* and *ephrin-B2* also demonstrated moderate but variable increases in expression (data not shown). The upregulation of *EphB2*, *EphB3*, and *ephrin-B3* was observed as early as 1-2 days post-laser treatment (Fig. 3-1B, F, J), and was initially most notable in the perivascular region of the pre-lamina ONH (Fig. 3-1B, F, J, arrows). At the later time points examined, *EphB2*, *EphB3*, and *ephrin-B3* cells were found throughout the lamina region of the ONH. Their upregulation peaked around day 4, and persisted for at least 1 week. Although we did not systematically examine the expression profile at later time points, the upregulation was maintained for as long as 3 weeks in some LIOH samples (data not shown).

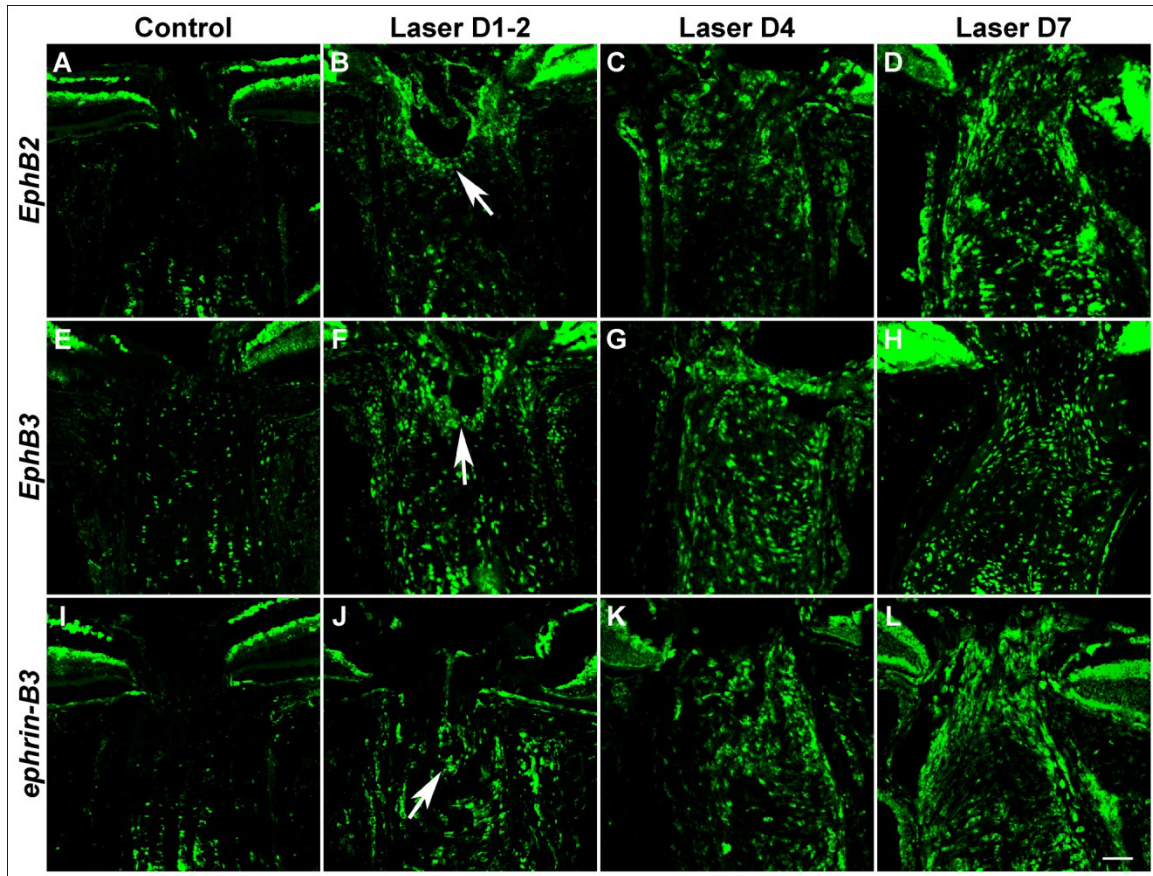


Figure 3-1. Upregulation of *Eph* and *ephrin* mRNAs at the laser-treated ONH
 Fluorescent *in situ* hybridization (FISH) demonstrated that the mRNA levels of *EphB2*, *EphB3* and *ephrin-B3* were increased above baseline (A, E, I) at 1-2 days (B, F, J), 4 days (C, G, K) and 7 days (D, H, L) after treatment. The initial upregulation tended to occur around the ONH perivascular region (B, F, J, arrows). Scale bar = 50 μ m. For each *Eph* and *ephrin* probe, FISH was repeated three times at each time point. An additional 3 or more FISH studies were performed with LIOH D4 samples. Subsequent FISH and antibody co-labeling experiments to determine cellular identities all utilized D4 samples unless otherwise stated.

To examine the upregulation of *EphB2*, *EphB3*, and *ephrin-B3* mRNAs more quantitatively, we performed real-time polymerase chain reaction (RT-PCR) on ONH tissues harvested 4 days after laser treatment and calculated their relative expression level compared to contralateral control samples (Fig. 3-2). *EphB2*, *EphB3*, and *ephrin-B3* mRNA exhibited 11.9-fold, 7.4-fold and 7.4-fold increase in experimental samples over

control levels, respectively. Two-way ANOVA analysis found no significant difference between the three mRNAs, suggesting that *EphB2*, *EphB3*, and *ephrin-B3* were upregulated to comparable extents in the laser-treated ONH. In summary, quantitative RT-PCR findings were consistent with *in situ* hybridization results in supporting the upregulation of *EphB/ephrin-B* mRNAs following LIOH in CD-1 mice.

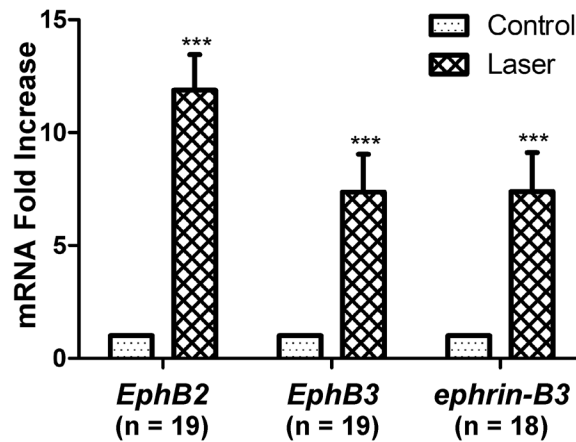


Figure 3-2. RT-PCR analysis of *EphB2*, *EphB3* and *ephrin-B3* mRNA expression
The mRNA level of laser-treated ONH samples was normalized to the contralateral control eye from the same animal. Nineteen pairs of eyes were used for the analysis of all three genes. One sample was lost in the *ephrin-B3* experiment, resulting in a sample size of 18.

ONH Expression of *Ephs* and *ephrins* in a Subset of Astrocytes

Eph/ephrin signaling has been shown to produce different outcomes depending on the cellular context²³⁵⁻²³⁶. Therefore, identification of the cell types that express these molecules is a necessary step in delineating their function. In the optic nerve, axons of RGCs are surrounded by astrocytes and microglia, which normally provide structural and

homeostatic support to axons and are known to respond to traumatic injuries to the nerve²³⁷.

To determine the cellular origin of *Eph/ephrin* expression at the ONH following laser treatment, we performed immunohistochemistry using cell-specific antibodies following *in situ* hybridization to detect *Eph* and *ephrin* mRNAs. GFAP is a widely accepted intermediate filament marker for astrocytes, also used elsewhere in this study. However, since antibodies against GFAP labeled astrocytic processes most intensely but cell bodies only weakly, it does not co-localize well with the predominantly somatic *in situ* hybridization signal, even if the two shared a common cellular origin. To circumvent this problem, we resorted to double-labeling with S100, another well-established astrocyte antigen, which stains the soma of astrocytes more robustly than GFAP²³⁸⁻²³⁹. The results showed that a subset of *EphB2*, *EphB3*, and *ephrin-B3* expressing cells at the ONH were also positive for S100 (Fig. 3-3C, F, I, insets and arrows). Not all *Eph/ephrin*⁺ cells (green) co-localized with S100 (arrowheads), and not all S100⁺ cells (red) expressed *Eph/ephrin* mRNA. In summary, *EphB2*, *EphB3* and *ephrin-B3* were present in ONH astrocytes following laser treatment, although they did not account for all the cells that express these mRNAs. In turn, *EphB2*, *EphB3* and *ephrin-B3* expressing astrocytes represented only a subset of the astrocytes present at the ONH following laser treatment.

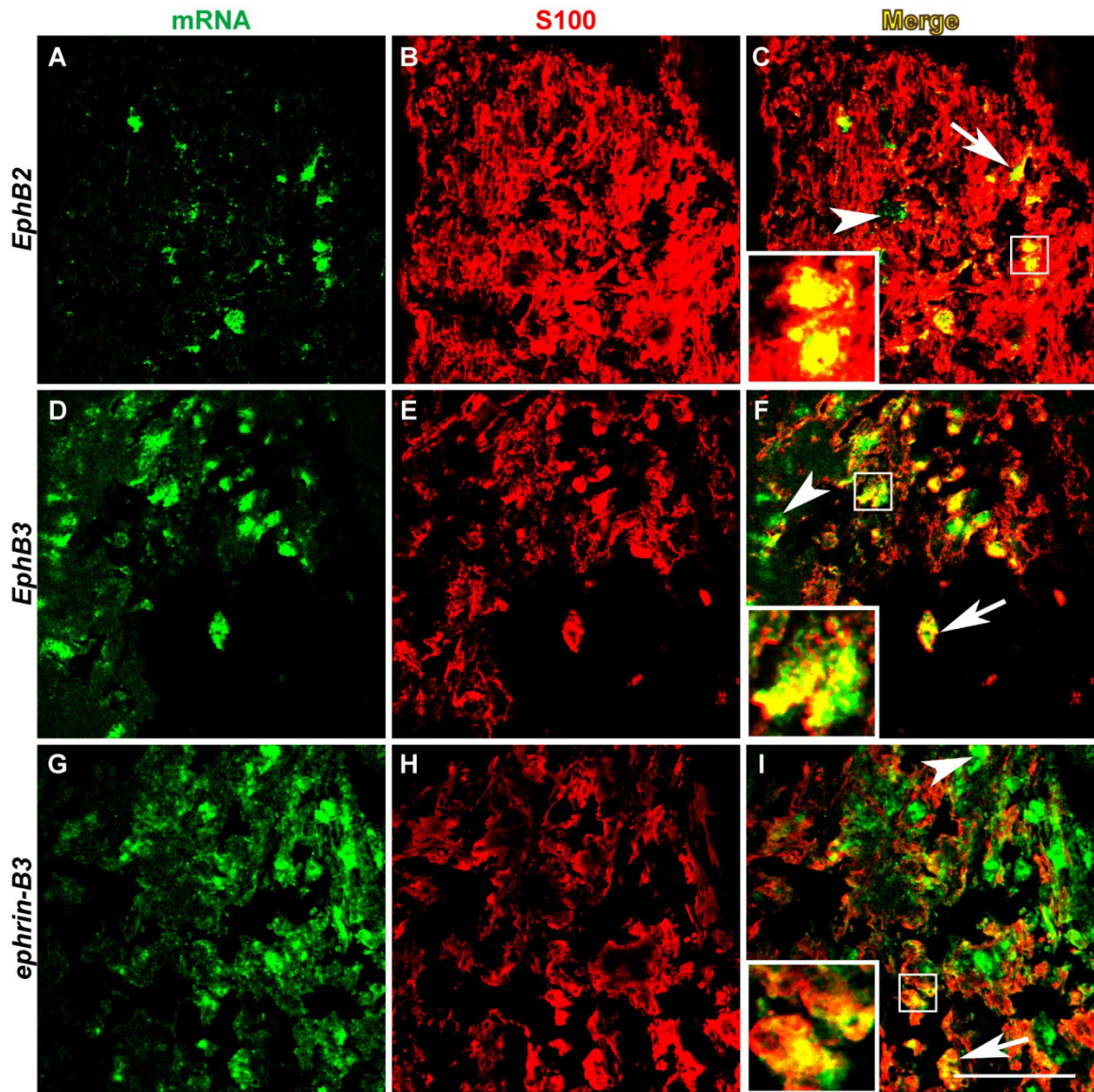


Figure 3-3. *Eph/ephrin* mRNAs were expressed in a subset of ONH astrocytes
In situ hybridization of EphB2, EphB3 and ephrin-B3 mRNAs (A, D, G) was followed with immunohistochemistry using S100 (B, E, H) as a marker for astrocytes. In merged images (C, F, I), the co-localization of *in situ* hybridization signal with S100 was indicated by yellow pixels (arrows and insets). Some cells expressing Eph/ephrin mRNAs were not immunoreactive for S100 (arrowheads). Scale bar = 50 μ m. n = 4 LIOH animals.

ONH Expression of *Ephs* and *ephrins* in Microglia

In a previous study, we found that *ephrin-B2* expression in DBA/2J glaucomatous mice was co-localized with ONH microglia. We thus sought to address whether microglia activation also occurred at the ONH after IOP elevation induced by laser treatment, and whether these cells contributed to the upregulation of *Eph/ephrin*. Our results demonstrated that the number of ONH cells labeled with the microglial marker Iba-1²⁴⁰ increased dramatically after laser photocoagulation (Fig. 3-4A-D). These cells did not appear to bear ramified processes as in controls (Fig. 3-4A inset) but were instead amoeboid in shape (Fig. 3-4B inset), suggesting that they have undergone activation. We also corroborated these findings with two other commonly used microglial markers, CD11b and isolectin GSA-IB4 (data not shown). Double-labeling with *EphB* or *ephrin-B* *in situ* hybridization and Iba-1 immunohistochemistry (Fig. 3-4E-P) revealed that a subset of cells that expressed *EphB2*, *EphB3* and *ephrin-B3* mRNAs were of the microglial lineage (Fig. 3-4H, L, P). Conversely, most of the Iba-1⁺ microglial cells present at the ONH after laser treatment appeared to express *EphB2*, *EphB3* and/or *ephrin-B3*.

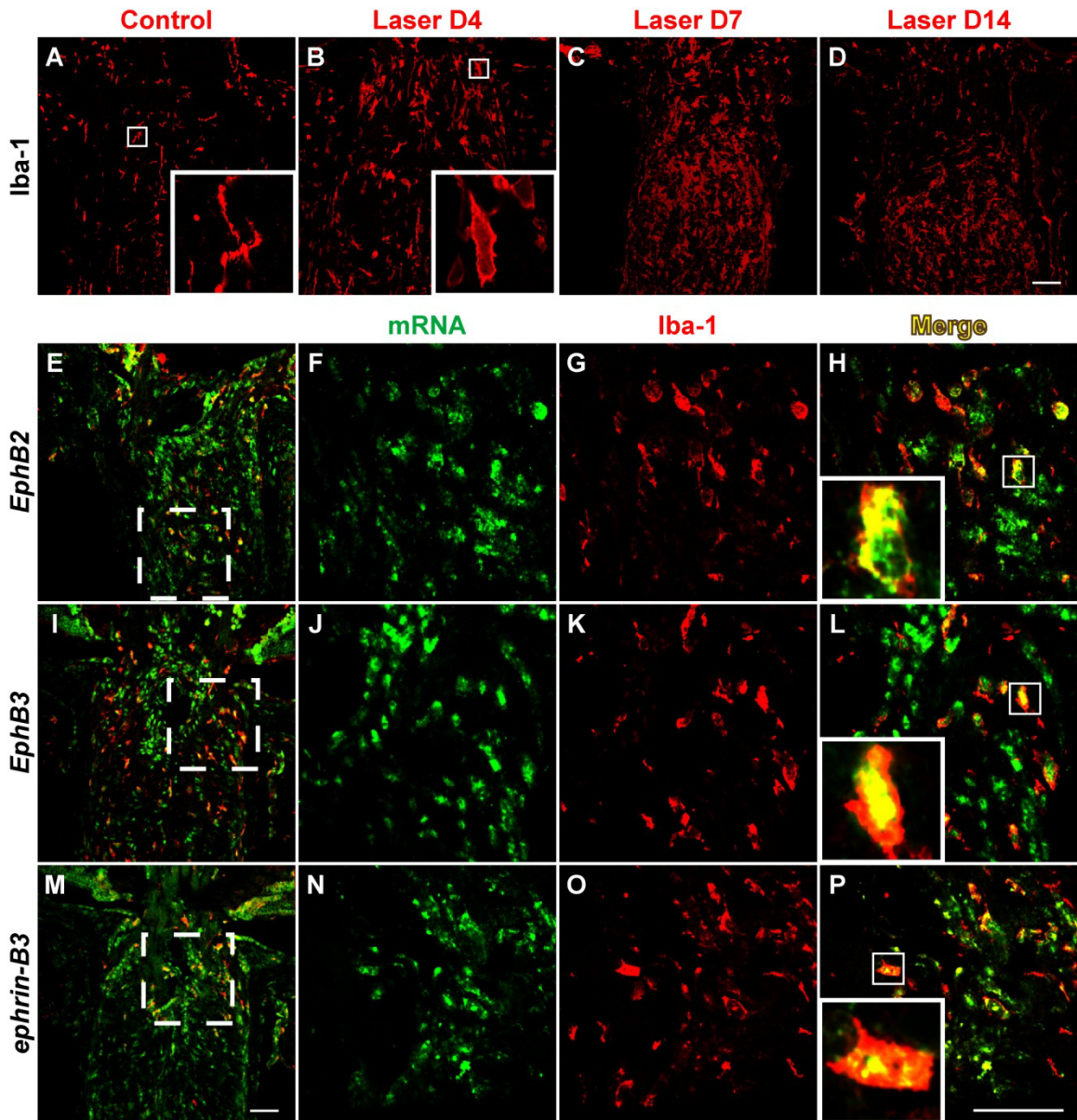


Figure 3-4. Microglia accumulation at the ONH after LIOH and expression of Eph/ephrin mRNAs

In the control optic nerve, microglia labeled with the Iba-1 antibody were present sparsely and appeared ramified (A, inset). After LIOH, an accumulation of microglia was observed (B-D), and these cells became more amoeboid in morphology (B, H, L, P, insets). Double-labeling of in situ hybridization (F, J, N) and Iba-1 immunostaining (G, K, O) demonstrated that many Iba-1+ microglia expressed EphB2 (E, H), EphB3 (I, L) or ephrin-B3 (M, P) mRNAs. Panels E, I, M are low magnification overviews in which higher magnification images were taken from the boxed regions. Scale bar = 50 μ m. n = 4 LIOH animals.

ONH Expression of *Ephs* and *ephrins* in Ectopic NG2⁺ Cells

A well recognized feature of the ONH is its lack of myelination and the specific exclusion of oligodendrocytes and NG2⁺ putative oligodendrocyte precursor cells (OPCs)²³⁷. In the course of studies examining the cellular origin of *EphB* and *ephrin-B* mRNA expression, we found that this cellular exclusion was compromised in laser-treated CD-1 mice, which manifested as the presence of ectopic NG2⁺ cells in the ONH region. The proteoglycan NG2 is normally expressed by a population of stellate-shaped cells (Fig. 3-5A-D, arrowheads) in the myelinated portion of the optic nerve, but is not found in the unmyelinated ONH region except for occasional staining of the vasculature (Fig. 3-5A, arrow). In ocular hypertensive eyes, cells expressing NG2 were ectopically located within the ONH (Fig. 3-5B, double arrow) beginning around 4 days after laser treatment. This phenomenon was also observed in DBA/2J mice exhibiting signs of optic disc cupping (Fig. 3-5D, double arrow) but not in age-matched histologically normal controls (Fig. 3-5C), consistent with a link between the appearance of NG2⁺ cells and glaucomatous damage. NG2⁺ cells found at the ONH tended to be more amoeboid-shaped (see top inset of Fig. 3-5B and insets in Fig. 3-5G, J, M), unlike the NG2⁺ cells with ramified processes observed in the myelinated regions of the optic nerve (bottom insets of Fig. 3-5A, B). *In situ* hybridization and anti-NG2 double-labeling studies (Fig. 3-5E-M) showed that ectopic NG2 cells contributed in part to the expression of *EphB2*, *EphB3* and *ephrin-B3* mRNAs at the ONH (Fig. 3-5G, J, M).

We focused our co-localization studies 4 days after LIOH, because the early onset was an important characteristic of *Eph/ephrin* upregulation, consistent with potential roles in disease development. Similar patterns were also observed at later time points. We

further examined additional cell-specific immunohistochemical markers, including PECAM-1 for endothelial cells²⁴¹, CD4 for T cells²⁴², and CD69 for activated lymphocytes²⁴³. No CD4 or CD69 immunoreactivity was detected in laser-treated samples indicating that T cell infiltration was not a feature of the ONH glaucomatous changes induced by laser treatment. PECAM-1 exhibited the typical staining of microvasculature, which was similar between treatment and control and did not overlap with the pattern of *Eph/ephrin* mRNA expression (data not shown).

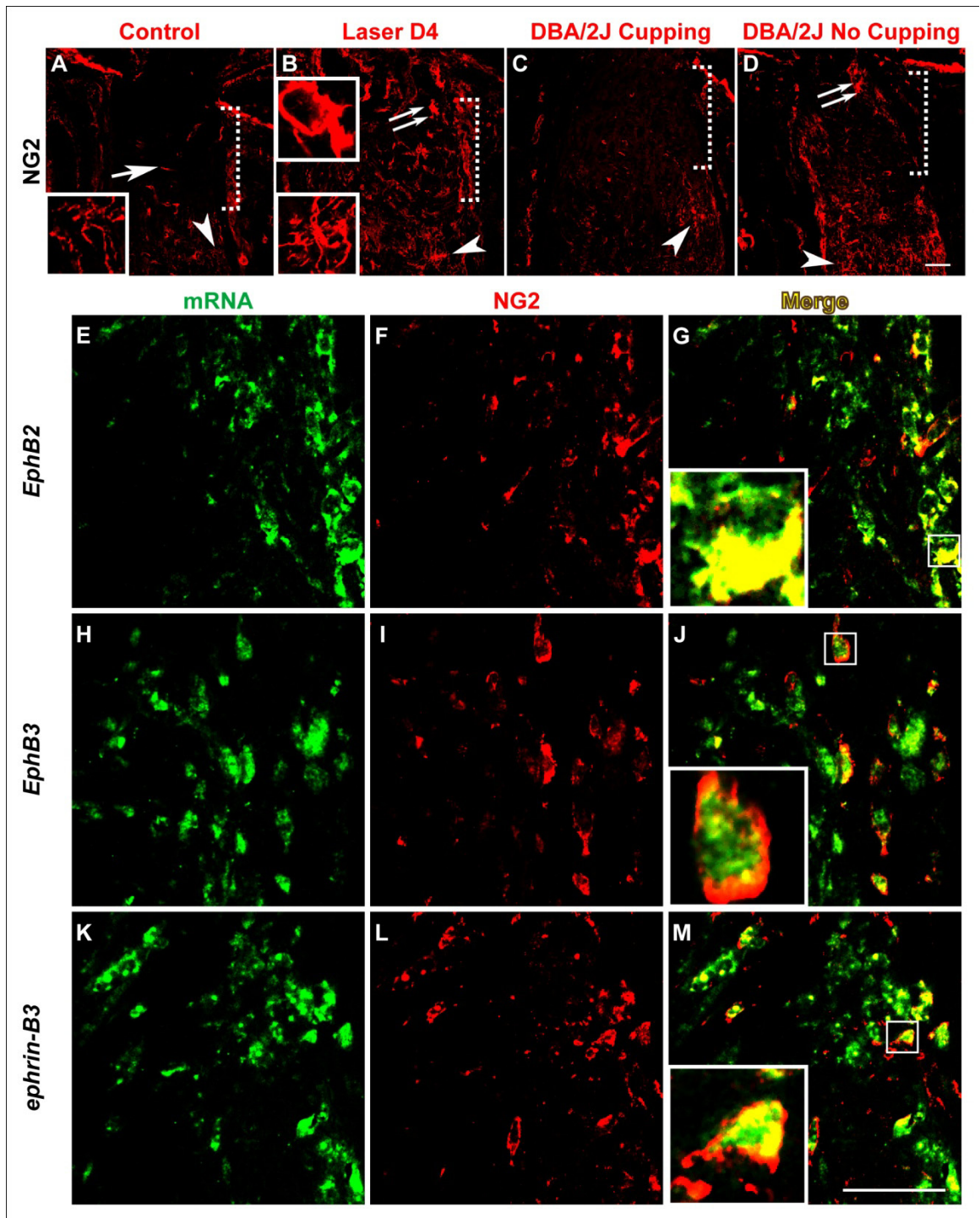


Figure 3-5. Ectopic NG2⁺ cells at the ONH expressed *Eph/ephrin* mRNAs

The NG2 marker labeled cells in the myelinated portion of optic nerve in all samples (A-D, arrowheads). In control CD-1 (A) and non-glaucomatous DBA/2J eyes without ONH cupping (C, DBA/2J No Cupping), no substantial NG2 immunoreactivity was detected at the unmyelinated ONH (demarcated by the dotted square bracket), except for minor vascular staining (A, arrow). In laser-treated CD-1 (B) and DBA/2J exhibiting signs of glaucomatous ONH cupping (D, DBA/2J Cupping), cells expressing NG2 were ectopically located within the ONH (double arrow). NG2⁺ cells normally found in the myelinated optic nerve were stellate in morphology bearing ramified processes (A and B, bottom insets), whereas those ectopically present at the ONH tended to be more amoeboid-shaped (top inset in B, insets in G, J, M). *In situ* hybridization of *EphB2*, *EphB3* and *ephrin-B3* mRNAs (E, H, K) was combined with anti-NG2 immunolabeling (F, I, L). Merged images (G, J, M) showed that ectopic NG2 signal at the ONH overlapped with a portion of *EphB2*, *EphB3* and *ephrin-B3* expressing cells. Scale bar = 50 μ m. n = 4 LIOH animals.

Together, these results indicate that there is broad-based cellular expression of *EphB2*, *EphB3*, and *ephrin-B3* in multiple cell types including astrocytes, microglia, and NG2⁺ cells at the ONH following experimental glaucoma induced by laser photocoagulation in CD-1 mice. This gene upregulation compared to untreated control is in part due to an increase in the number of Iba-1⁺ microglia and ectopically located NG2⁺ cells, possibly reflecting a disruption of the local cytoarchitecture. While the majority of Iba-1⁺ microglia and NG2⁺ cells express *EphB2*, *EphB3*, and *ephrin-B3*, only a subset of astrocytes upregulated these mRNAs following laser-induced ocular hypertension.

Upregulation of ephrin-B Reverse Signaling After Laser Treatment

The Eph and ephrin system can engage in bidirectional signaling, sending information in both the forward direction into Eph receptor expressing cells, or in the reverse direction into ephrin ligand expressing cells²⁴⁴. In both cases, binding of Eph molecules with ephrins on an opposing cell leads to the clustering and subsequent

tyrosine phosphorylation of Ephs and ephrins. Therefore, detection of phosphotyrosine residues on Eph/ephrin proteins serves as an indication of receptor activation and signaling. To determine whether the upregulation of *Eph* and *ephrin* mRNA observed in laser treated eyes resulted in increased Eph and ephrin signaling, we examined ephrin-B activation using an antibody that specifically recognizes ephrin-B1, B2 and B3 proteins that are phosphorylated at tyrosine 324/329, but does not bind to the non-phosphorylated forms of these proteins. Phospho-ephrin-B (pEB) was constitutively expressed at low levels at the control ONH (Fig. 3-6A). The pEB immunoreactivity was substantially enhanced between 4 to 7 days (Fig. 3-6E, I) after laser treatment and subsided after 2 weeks (Fig. 3-6M). Of note, pEB immunoreactivity was localized to discrete patches within the ONH. The relationship between pEB immunoreactivity and astrocytes (visualized using GFAP) as well as axons (visualized using tubulin) is presented at low magnification in Fig. 3-6. High magnification images taken from the lamina ONH (Fig. 3-7) revealed that the cellular identity of patches containing increased pEB immunoreactivity was heterogeneous. In some areas, pEB was co-localized mainly within RGC axons (Fig. 3-7E-H, arrowheads and arrows) or within microglia (Fig. 3-7I-K). In others, pEB co-localized substantially with astrocytes (Fig. 3-7A-D, arrowheads). Upon inspection at higher magnification, immunostaining of pEB appeared as puncta of 0.1-1 μm in size (Fig. 3-7D, H, arrowheads), consistent with the known clustering of Eph/ephrin receptor after activation²⁴⁵. In addition, there were also larger pEB immunoreactive units that spanned the entire axon width and stretched over several microns in length (Fig. 3-7H, arrows), possibly reflecting aggregation of EphB/ephrin-B signaling complexes into higher order clusters¹⁵⁶. The expression of ephrin-B protein by

normal adult RGC axons has been previously demonstrated with *in vivo* EphB-Fc binding assays¹²⁸. Taken together, these results demonstrated the upregulation of *Eph* and *ephrin-B* mRNA expression that occurred as early as 1-2 days after laser treatment led to increased Eph-ephrin signaling, and this signaling appeared to involve multiple cellular elements including astrocytes, microglia, and RGC axons.

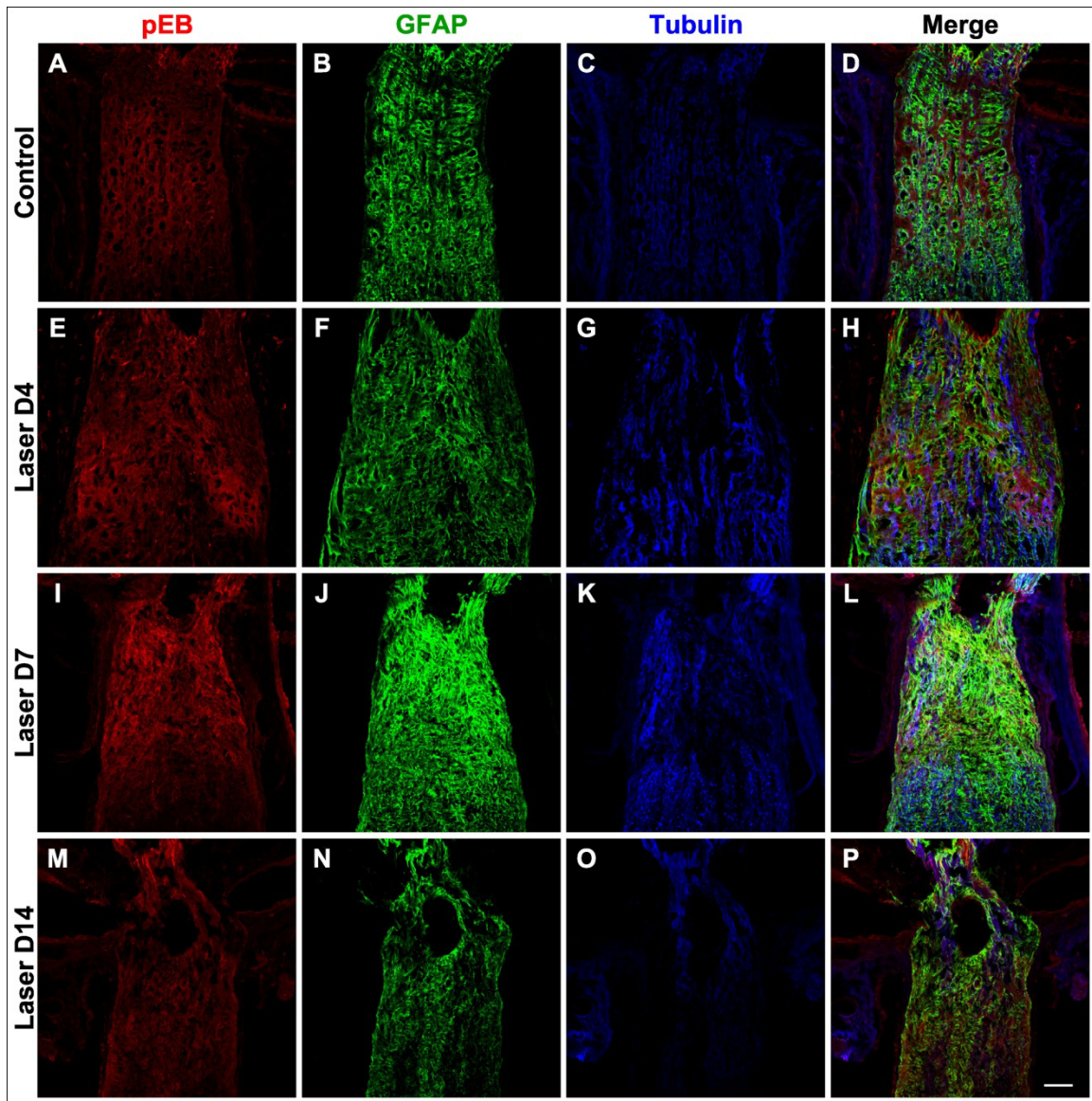


Figure 3-6. Upregulation of phosphorylated ephrin-B (pEB) protein

A constitutive baseline expression of pEB was observed at the ONH of control samples (A). The intensity of immunoreactive signal was substantially increased at 4 days (E) and 7 days (I) following laser treatment, and declined by 2 weeks (M). Co-labeling of astrocytes with GFAP (B, F, J, N), axons with tubulin (C, G, K, O), and merged images (D, H, L, P) were presented at low magnification to provide a survey view of the spatial relationship between these markers. Scale bar = 50 μ m. n = 3 sets of experiments.

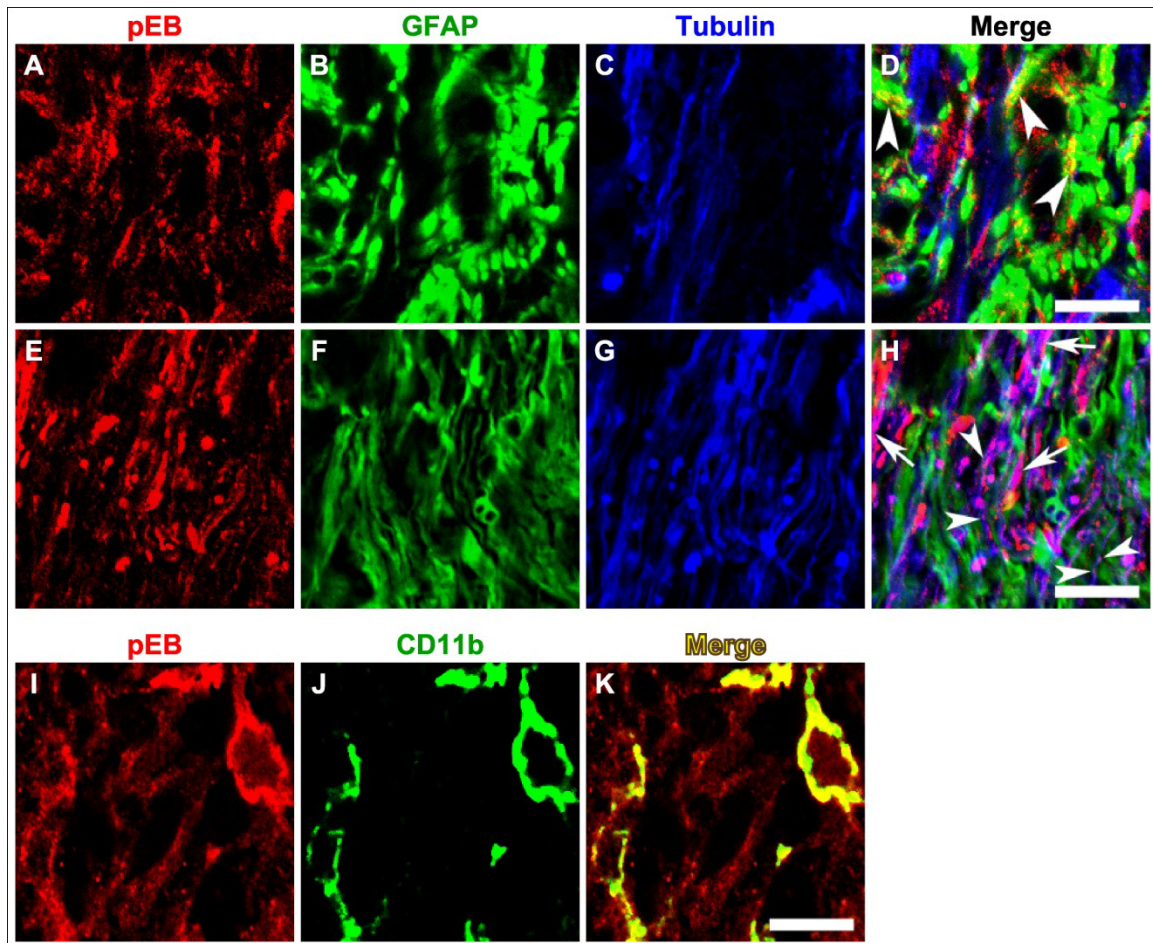


Figure 3-7. Expression of phospho-ephrin-B in astrocytes, axons and microglia at the lamina ONH

Phospho-ephrin-B (A, E, I) was co-labeled with GFAP for astrocytes (B, F), tubulin for axons (C, G), or CD11b for microglia (J). The expression of pEB was found to co-localize predominantly with astrocytes in some patches (D, arrowheads), and axons in others (H, arrowheads for small puncta and arrows for large puncta possibly reflecting high order clusters). Microglia also expressed pEB (K). Scale bar = 10 μ m.

ephrin-B Reverse Signaling Differentiates Axons with Radial versus Aberrant Trajectories

To better understand the potential basis of the heterogeneity of pEB signaling particularly in RGC axons, we examined the relationship between pEB expression and axonal morphology. A feature of axon responses to IOP elevation in the pre-lamina ONH in CD-1 mice is the display of axonal reactive plasticity characterized by defasciculation, axonal enlargement, and aberrant meandering axon trajectories²³². However at the population level, axons are heterogeneous as some exhibit morphological characteristics of reactive plasticity while others have yet to be affected and maintain their normal appearance. For example, at 7 days after laser treatment, a number of axons exhibited defasciculation and aberrant meandering trajectories (Fig. 3-8D, G, top insets), in contrast to the tightly bundled axons in control retinal whole-mounts (Fig. 3-8A). Concurrently, other axons have yet to display overt signs of damage and retained their radially directed course to the ONH (Fig. 3-8D, G, bottom insets). Immunohistochemical detection demonstrated marked enhancement of pEB expression in retinal whole-mounts harvested 7 days after laser treatment (Fig. 3-8E, H) compared to the control group (Fig. 3-8B), consistent with findings at the lamina ONH (Fig. 3-6). Of note however, the overall increase of pEB expression was mainly observed in axons that appeared morphologically normal, tightly bundled and radially oriented (Fig. 3-8D-F and G-I, bottom insets). In contrast, the majority of RGC axons with aberrant meandering or undulating trajectories that deviated from the normal radial course had no significant pEB expression above background (Fig. 3-8D-F and G-I, top insets). This apparent lack of pEB immunoreactivity may reflect either a reduction in total protein expression or decreased

ephrin-B reverse signaling. The level of pEB fluorescence was quantified in six pairs of retinas (Fig. 3-8J). In LIOH samples, the intensity of pEB on normal axon bundles was higher than both the contralateral control and aberrant axon segments. In contrast, pEB expression by aberrant axons was not significantly different from axons present in control retinas. In summary, following LIOH induction, ephrin-B reverse signaling appeared to be transiently increased in the population of RGC axons that have yet to exhibit overt morphological signs of altered physiology such as defasciculation, and meandering or undulating trajectories.

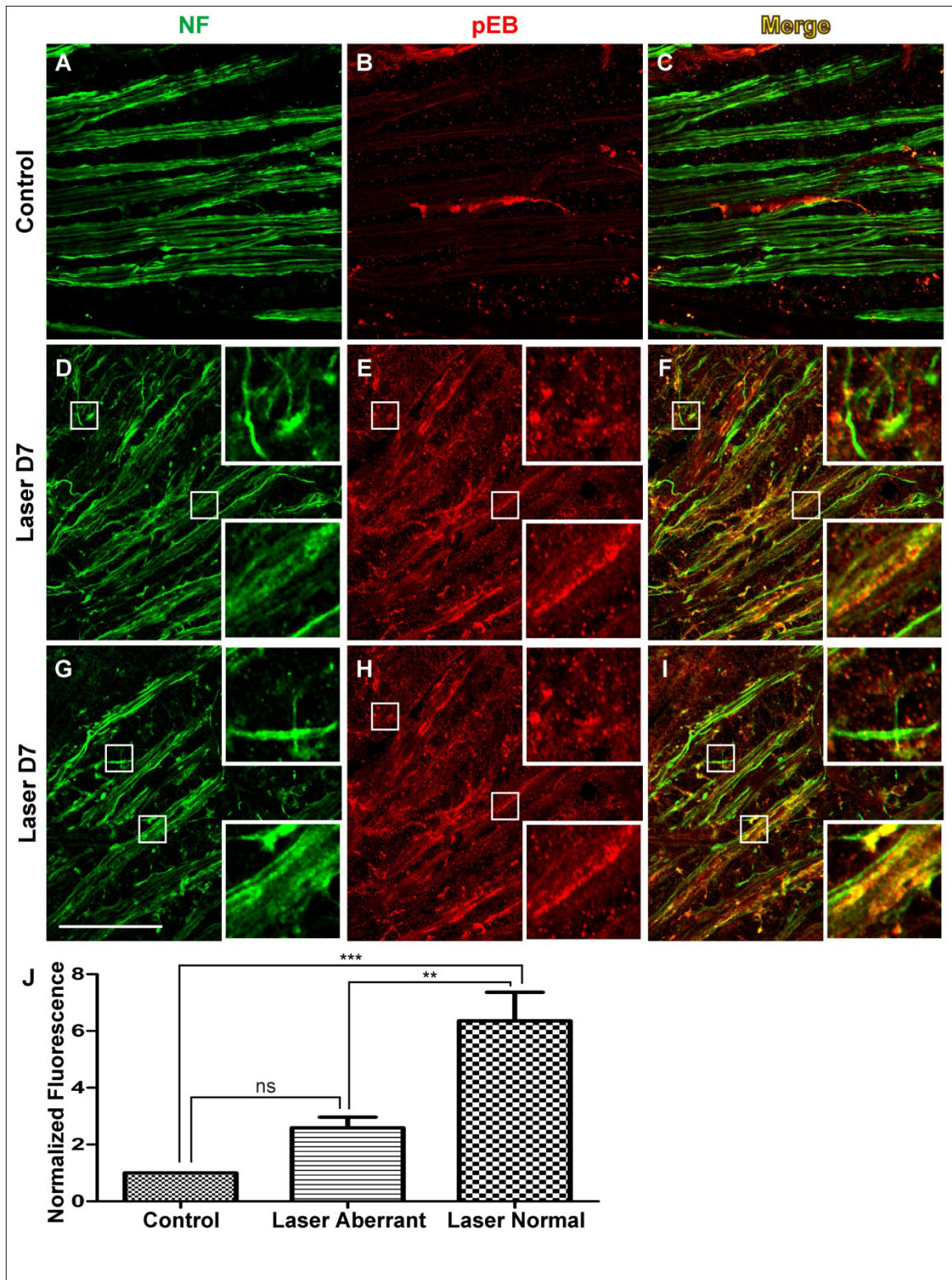


Figure 3-8. Heterogeneity of phospho-ephrin-B expression in the LIOH retina
Retinal whole-mounts were processed for immunolabeling of pEB (**B, E, H**) and NF (**A, D, G**) to identify axons. Shown here are examples from one control retina (**A-C**) and two D7 LIOH retinas (**D-F** and **G-I**) processed in parallel. Significant upregulation of pEB was observed after laser treatment (**E, H**) compared to controls (**B**). In LIOH samples, axons that remained in tight radial bundles expressed high levels of pEB (**D-F** and **G-I**, bottom insets), while pEB was markedly lower in axons with aberrant trajectories (**D-F** and **G-I**, top insets). Scale bar = 50 μm . (**J**) Quantification of pEB expression. The pEB fluorescence intensities of morphologically normal and aberrant axons in laser-treated retinas were determined and normalized to the contralateral control eye (see Materials and Methods). Morphologically normal LIOH axons expressed pEB at higher levels than axons in untreated control retinas (normalized fluorescence value was significantly greater than 1). Morphologically aberrant axons in the same samples did not significantly differ from control. $**p < 0.01$; $***p < 0.001$. $n = 6$ LIOH animals.

EphB Deficiency Aggravates Glaucomatous Axonal Degeneration

To investigate the functional significance of EphB/ephrin-B signaling, we performed LIOH in several mutant lines of mice: *EphB2*^{-/-230}, *EphB2*^{lacZ/lacZ230} and *EphB3*^{-/-231}. The *EphB2*^{-/-} and *EphB3*^{-/-} are protein null alleles, whereas *EphB2*^{lacZ/lacZ} encodes a fusion protein in which the tyrosine kinase and C-terminal domains of EphB2 are replaced by β -galactosidase (β -gal). This EphB2- β -gal fusion receptor is deficient in forward signaling due to the lack of catalytic tyrosine kinase domain and PDZ-binding motif. All these lines have been maintained in the CD-1 background.

The mutant mice were subjected to LIOH together with wild-type littermates. Axonal count in PPD-stained optic nerve cross sections were obtained one week after treatment. Control mice across genotypes contained comparable numbers of RGC axons (Fig. 3-9F). In wild-type, LIOH (Fig. 3-9B) reduced axon count to 62% of untreated controls (Fig. 3-9A) of the same genotype. *EphB2*^{-/-} (Fig. 3-9C) and *EphB3*^{-/-} mice (Fig. 3-9E) exhibited significantly more severe axonal degeneration compared to wild-type

littermates (quantified in Fig. 3-9F). In these mice, the number of surviving axons was reduced to 21% and 28% of genotype-matched controls, respectively. These data indicate that EphBs normally protect axons against glaucomatous injury. In addition, the C-terminally truncated *EphB2^{lacZ/lacZ}* mice (Fig. 3-9D) were also significantly more susceptible to LIOH than wild-type, although not as much as the protein null mutant *EphB2^{-/-}*. The 40% axon reduction observed in *EphB2^{lacZ/lacZ}* was intermediate between wild-type and *EphB2^{-/-}*, suggesting that the intracellular C-terminus and extracellular N-terminus each accounts for part of the protective effect of EphB2. Taken together, these data are consistent with a role of bidirectional EphB/ephrin-B signaling in promoting axon survival in experimental glaucoma.

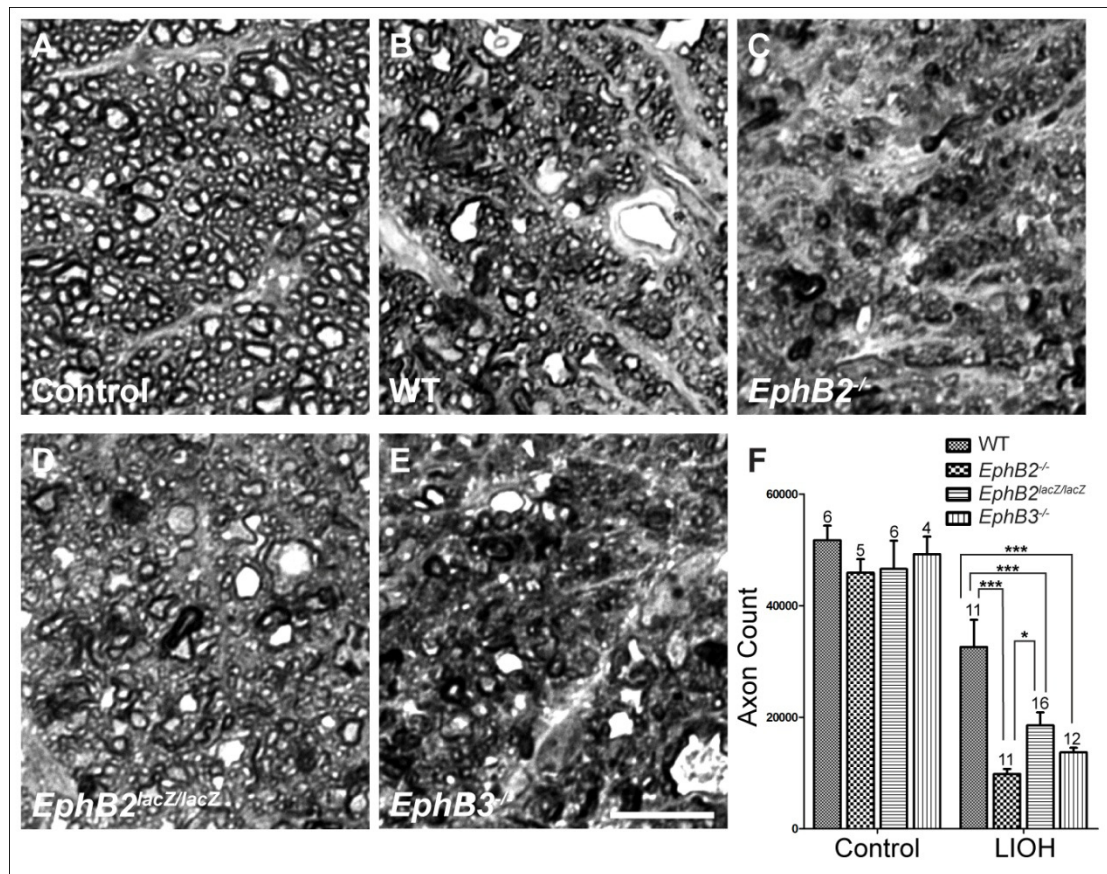


Figure 3-9. EphB mutants exhibit more severe axonal degeneration in experimental glaucoma

(A-E) Representative PPD-stained optic nerve cross sections used for analysis. (A) Since axon counts are not statistically different across genotypes, a control nerve from a wild-type mouse is shown here. (B) Wild-type, one week post-LIOH. (C) *EphB2*^{-/-}, LIOH. (D) *EphB2*^{lacZ/lacZ}, LIOH. (E) *EphB3*^{-/-}, LIOH. (F) Quantitative analysis of axon count in control and LIOH samples of different genotypes. LIOH treatment results in significant axon loss compared to genotype-matched control mice. Both *EphB2*^{-/-} and *EphB3*^{-/-} mutants show more aggravated axonal degeneration compared to wild-type. The *EphB2*^{lacZ/lacZ} line is also significantly more affected than wild-type, although its phenotype is not as severe as *EphB2*^{-/-}. Scale bar: 10 μm. The n number of each experimental group is indicated above the bar graph. **p* < 0.05; ****p* < 0.001.

Discussion

Shared Eph and ephrin Upregulation in Human Glaucoma and Animal Models

The present data in CD-1 LIOH agree with previous findings of EphB/ephrin-B upregulation in DBA/2J¹²⁸ as well as primate and human glaucomatous tissues²⁴⁶, indicating that it may be a basic characteristic of disease. Intriguingly, distinct sets of *Eph/ephrin* molecules are expressed in CD-1 LIOH compared to previous reports, and the distribution of *Eph/ephrin* expressing cells are relatively more dispersed compared to the focal pattern observed in DBA/2J. These distinctions might be due to differences in species, strain background, stage of disease, or could be a consequence of the different forms of glaucoma mimicked by the various models. The chronic progressive nature of DBA/2J glaucoma versus the more compressed time course of CD-1 LIOH could also underlie differences in the expression of particular family members. Nevertheless, the upregulation of Ephs and ephrins at the ONH in human glaucoma as well as three animal models of disease is consistent with a potential role of these molecules in modulating the development and/or progression of glaucoma.

Early Response of Eph/ephrin System after IOP Elevation

We have previously demonstrated that pathological changes in RGC axons at the ONH occurred by day 4 after IOP elevation in CD-1 mice²³². Here we report that the upregulation of *EphB2*, *EphB3* and *ephrin-B3* mRNA was observed 1-2 days following

LIOH, and thus its occurrence was coincident with or possibly prior to overt signs of axon damage, suggesting potential involvement early in axon response to IOP elevation. The increase of *EphB/ephrin-B* mRNA expression was reflected in a transient increase of phosphorylation-dependent ephrin-B reverse signaling between 4-7 days, involving astrocytes, microglia and RGC axons. Drawing on data from this study and our previous characterization of the LIOH model²³², a summary figure (Fig. 3-10) illustrates how the temporal *EphB/ephrin-B* upregulation and signaling may fit into the approximate sequence of pathological events after LIOH.

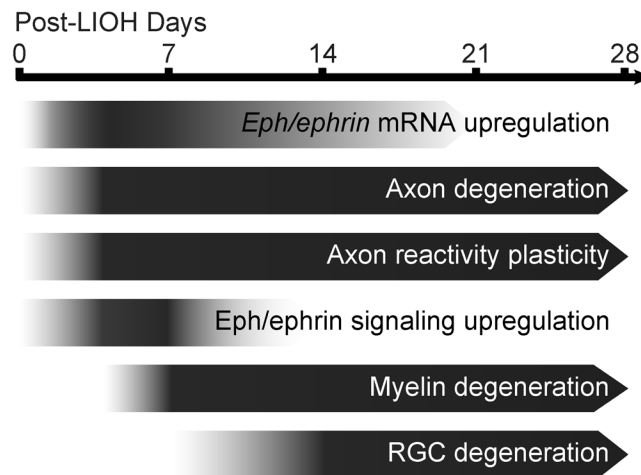


Figure 3-10. Approximate timeline of pathological events after LIOH

Eph/ephrin mRNA upregulation occurred around 1-2 days following laser treatment, coinciding with or preceding the earliest manifestation of axonal injury. By day 4, evidence of axon damage, degeneration and reactive plasticity at the ONH were apparent. Phosphorylation-dependent ephrin-B signaling was transiently upregulated around this time, and declined to baseline during the second week. Signs of myelin degradation were first detected after 1 week, and significant reduction of Brn-3b⁺ RGC density occurred after 2 weeks.

A Broad-Based Axonal/Glial Network of Eph/ephrin Signaling

A notable finding in the present study is the expression of *EphB2*, *EphB3* and *ephrin-B3* in multiple ONH cell types including microglia, astrocytes, and ectopic NG2⁺ cells. This shared upregulation suggests a common mechanism governing the response of multiple glial cell types to elevation in IOP and perhaps to other local ONH changes.

The upregulation of *EphB/ephrin-B* genes resulted in increased phosphorylated ephrin-B proteins in RGC axons, microglia, and astrocytes, indicating the enhancement of active ephrin-B mediated reverse signaling. Although we did not directly examine EphB proteins due to the lack of specific antibodies, their presence is evidenced by the activation of ephrin-B. Adult RGC axons express both EphBs and ephrin-Bs¹²⁸, rendering them competent to respond to the complementary receptor/ligand on neighboring cells.

Astrocytes²⁴⁷ and microglia²⁴⁸ have long been implicated in CNS injuries and neurodegenerative diseases. A number of studies reported increased proliferation or altered gene expression profile of microglia in glaucoma^{8,111,249-251}, and inhibition of microglia activation could be neuroprotective in DBA/2J⁶. However, most of these studies focused on the characterization of glaucomatous retina, while microglial response at the ONH has not been investigated prior to the present work. NG2⁺ cells have been shown to contribute to inhibitory scar formation after spinal cord lesion²⁵²⁻²⁵³, and have been demonstrated to possess stem cell potential in the adult CNS²⁵⁴⁻²⁵⁵. Although one study examining NG2⁺ pericytes did not detect significant alteration in glaucoma-susceptible DBA/2J retina²⁵¹, our observation of ectopic NG2⁺ cells warrants exploration of their involvement at the glaucomatous ONH. The mouse ONH is unmyelinated, where

axons are intimately associated with a dense meshwork of astrocytes⁴⁸. In this unique environment, glial cells have the potential to engage in reciprocal contact-dependent signaling, as well as to exert direct effects on axons. Therefore, the activation of ephrin-B reverse signaling in multiple ONH cell types may reflect communication along the glia-glia, glia-axon or axon-axon axes.

Transient ephrin-B Reverse Signaling in RGC Axons

The transient increase of axonal ephrin-B reverse signaling in CD-1 LIOH is of note for several reasons. First, activation of ephrin-B reverse signaling is present in axons within both the lamina and the pre-lamina regions of the ONH, corresponding to the sites of the earliest detectable morphological change in both the LIOH model and in DBA/2J glaucomatous mice^{48,232}. Second, ephrin-B reverse signaling is active during the first week after IOP elevation, coinciding with the initial appearance of apparent morphological signs of axon damage and axon reactive plasticity. Third, ephrin-B reverse signaling appears to be active preferentially in RGC axons that are early in their response to glaucomatous injury rather than in axons that appear to be further along in the pathological cascade as evidenced by their morphological reactive plasticity. To our knowledge, this is the first report to link the activated form of a signaling molecule with specific RGC axon response states in glaucomatous disease. It is unclear whether the aberrant axons with apparently low pEB expression were prevented from ephrin-B reverse signaling, or whether they had previously undergone transient ephrin-B signaling and subsequently downregulated pEB expression. In either case, the observation that

diminution of ephrin-B signaling is associated with axonal pathology would be consistent with the aggravated glaucomatous degeneration in EphB mutants.

Bidirectional Eph/ephrin Signaling in Axonal Protection

Using EphB mutants, we have demonstrated that deletion of EphB2 or EphB3 results in more severe axonal degeneration after induction of ocular hypertension. These findings provide evidence for a neuroprotective role of EphB receptors in glaucoma. The observation that either EphB2 or EphB3 deficiency produces a detectable change argues that the effect of EphB proteins is dose-dependent. Although redundancy of different Eph and ephrin family members in development has been reported by many studies^{156,182,256}, a pathological situation in adulthood might behave differently. In this context, EphB and ephrinB expression at the normal adult ONH is low, and only becomes upregulated after induction of ocular hypertension. The relatively short-term exposure to glaucomatous injury in this experimental model may not allow for significant compensatory action between EphB family members. Furthermore, mice carrying the C-terminally truncated EphB2 exhibits a phenotype intermediate between wild-type and *EphB2*^{-/-}. This suggests that on one hand, deletion of the EphB2 C-terminal domains renders the animals more susceptible to glaucomatous insults, possibly due to the loss of forward signaling. On the other hand, the remaining ectodomain is able to mediate part of the protective function of EphB2, likely via reverse-signaling through ephrin-Bs.

EphB forward signaling principally depends on the catalytic kinase domain, which can act through autophosphorylation as well as phosphorylation of other proteins.

A plethora of effector molecules can be recruited to the receptor to mediate downstream signaling cascades, including Src family kinases and guanine nucleotide exchange factors (GEFs), which in turn activate the Ras/Rho-family GTPases^{244,257}. The C-terminal region can also signal via kinase-independent mechanisms, including protein association with its PDZ-binding motif. For example, the ability of EphB2 to cluster the alpha-amino-3-hydroxy-5-methyl-4-isoxazolepropionic acid (AMPA) receptors appears to depend on its PDZ-domain-binding but not kinase catalytic activities²⁵⁸. The ephrin-B reverse signaling pathway also involves tyrosine phosphorylation of the C-terminus by Src family kinases, or protein association with the PDZ-binding domain. EphB ectodomain can activate reverse signaling without the participation of its intracellular portion, which may account for the partial effect of EphB2- β -gal in *EphB2^{lacZ/lacZ}* mice. Alternatively, EphB ectodomain may also interact with other molecules in *cis*^{244,259}. The facilitation of N-methyl-D-aspartate (NMDA) receptor clustering at synapses is kinase-independent and mediated by the extracellular N-terminus of EphB2¹⁸⁶. In addition, extensive interplay between Eph/ephrin family members and components of other signaling pathways has been described¹⁵⁶. The possibility remains that the observed function of EphB proteins could be mediated by either *cis* or *trans* interaction with other pathways. In conclusion, the data presented in this study are consistent with a model in which the EphB/ephrin-B system promotes axonal survival via bidirectional signaling, or crosstalk with additional signaling pathways. Precisely what downstream mechanisms are involved in this effect awaits future investigation.

Chapter 4

The Role of Vesicular Glutamate Release and Glutamate Signaling in Experimental Glaucoma

Abstract

Substantial evidence suggests that the optic nerve head (ONH) is an important site of initial damage to retinal ganglion cell (RGC) axons in glaucoma, and axonal degeneration involves pathways distinct from soma apoptosis. The localized pathogenic mechanisms that selectively insult RGC axons at the ONH are still being delineated. Here we demonstrate that glutamatergic synaptic vesicle-like structures accumulate within RGC axons at the ONH in a mouse experimental model of glaucoma. These ectopic vesicles are fusion-competent and can release glutamate. Glutamate receptor activation is increased at the glaucomatous ONH, and blocking glutamate signaling pharmacologically correlates with a reduction in apparent axon damage *in vitro* and *in vivo*. Using the *Cre-loxP* recombination system, we show that restricted deletion of the vesicular glutamate transporter VGLUT2 or the obligatory N-methyl-D-aspartate (NMDA) receptor subunit NR1 in RGCs promotes axon survival in experimental glaucoma *in vivo*. These findings present a novel mechanism of localized excitotoxicity likely causing focal axonal injuries, which is consistent with the sectorial pattern of RGC loss observed in glaucoma. The demonstration that ectopic release of excitatory neurotransmitter could mediate neuronal injury without clearly defined post-synaptic specializations may also bear on questions of the pathophysiology seen in other neurodegenerative disorders such as Alzheimer's disease.

Introduction

There are some remarkable parallels between the axon damage seen following glaucoma and other neurodegenerative disorders, particularly Alzheimer's disease (AD)²⁶⁰⁻²⁶¹. High occurrence rate of glaucoma has been reported among patients with AD²⁶²⁻²⁶⁴. Evidence is accumulating that amyloid- β (A β) deposition, a hallmark of AD²⁶⁵, also occurs in glaucoma. In vitreous samples from human glaucoma patients, a decrease in the A β level was documented, similar to the characteristically reduced A β in the cerebrospinal fluid of AD patients²⁶⁶. A β was shown to accumulate and co-localize with apoptotic RGCs in experimental glaucoma^{46,267}, and targeting components of the A β formation and aggregation pathway *in vivo* reduced RGC apoptosis²⁶⁷. In the DBA/2J model, A β immunoreactivity was also found at higher intensity in the retina as well as optic nerve of older compared to younger animals²⁶⁸. These observations suggest that glaucoma and AD may share common pathophysiological pathways.

While characterizing axonal morphology in the LIOH model, I became intrigued with the striking reactive plasticity axons exhibit at the glaucomatous ONH, which is reminiscent of the sprouting phenomenon described in AD. Axonal sprouting has been observed in many forms of nerve damage, including entorhinal lesion, optic nerve crush, and sciatic nerve transection^{139,269-271}. Compared to these acute injuries, the pathology of AD may be more relevant to glaucoma as a chronic neurodegenerative disease. Studies in the 1990's have documented extensive sprouting of GAP-43-positive neurites in the hippocampus as well as neocortex of AD patients^{150,272-274}. Many of these appeared to be abnormal dystrophic processes, and were found abundantly associated with A β -containing senile plaque. Although the synaptic pathology in AD is characterized by an

overall loss of synapses, many of the aberrant sprouting neurites are positive for several pre-synaptic markers including Synaptophysin^{151,274-276}. Aberrant neurites were not only localized to axon termination zones, but were also found at ectopic locations including white matter tracts¹⁵¹. The functional significance of these findings has not been followed up in recent years, but they raise the question whether similar synaptic pathologies can also be observed in aberrant axons in glaucoma.

I started investigating this question by immunohistochemical localization of pre-synaptic markers in the LIOH model. Dramatic accumulation of several synaptic vesicle (SV) markers is found at the glaucomatous ONH, a non-synaptic region in normal animals. Ultrastructural analysis by immuno-electron microscopy demonstrates that Synaptophysin-positive translucent vesicles are present in ONH axons after LIOH. The ectopic vesicles contain glutamate, co-localize with components of the SNARE complex and active zone cytomatrix protein Bassoon, and undergo exocytosis *in vitro* and *in vivo*. Acute preparations of glaucomatous ONH can release glutamate *ex vivo*. Immunohistochemical and functional studies indicate that glutamate receptors are expressed on ONH axons and glia, and are more active in LIOH compared with controls. Pharmacological antagonism of glutamate receptors is protective to RGC axons *in vitro* and *in vivo*. Selective disruption of the vesicular glutamate transporter VGLUT2 or obligatory NMDA receptor subunit NR1 in RGCs promotes RGC axon survival in experimental glaucoma *in vivo*. Taken together, these data provide evidence for a previously unappreciated mechanism of excitotoxicity via excessive vesicular release of glutamate in glaucoma. Although I did not identify evidence of highly specialized assembly of ectopic synapses, the data suggest RGC axons can respond to excessive

extracellular glutamate without post-synaptic density-like specializations. Therefore, neurotransmission-related pathology may involve not only the loss of synapses but also ectopic activity of unpaired neurotransmitter release apparatus. This idea may bear wide-ranging implications for other neurodegenerative diseases, and warrants further exploration.

Materials and Methods

Mouse Lines

Mice carrying floxed *NMDAR1* (*NR1*; *Grin1*) gene were described previously²⁷⁷. The *loxP* sequences flank a region of the *NR1* gene that encodes the transmembrane domains and the entire C-terminal sequence of its protein product. The mice (referred to in this study as NR1-f) were originally maintained in a C57BL/6 background, and were generously donated by Dr. Richard Palmiter at University of Washington.

A conditional allele of the mouse *Slc17a6* gene encoding VGLUT2 was generated by engineering two *loxP* sites surrounding exon 2²⁷⁸. The mice (referred to in this study as VGLUT2-f) were generated by Dr. Tomas Hnasko while in Dr. Richard Palmiter's lab at University of Washington. The breeding pair in C57BL/6 background used to establish our colony was a gift from Dr. Robert Edwards at UCSF.

The B6-albino mice, B6(Cg)-*Tyr^{c-2J}*/J, were purchased from the Jackson Laboratory (Bar Harbor, ME; stock number 000058). They are identical to C57BL/6J except for a mutation in the tyrosinase gene (*Tyr^{c-2J}*). These mice were bred to the black NR1-f and VGLUT2-f mice for two generations to obtain albino floxed transgenics. F2 animals homozygous for both the albinism and floxed loci (*Slc17a6^{loxP/loxP}*; *Tyr^{c-2J/c-2J}* and *NR1^{loxP/loxP}*; *Tyr^{c-2J/c-2J}*) were identified based on coat color and genotyping results.

CD-1 mice were purchased from Charles River Laboratories (Wilmington, MA). All experiments were performed in under protocols approved by the UCSF Institutional Animal Care and Use Committee, and were in accordance with the ARVO Statement for the Use of Animals in Ophthalmic and Vision Research.

Laser-Induced Ocular Hypertension (LIOH)

LIOH was performed in CD-1 mice as described in Chapter 2. For B6-albino mice, 50 μm instead of 100 μm spot size was used to photocoagulate the episcleral veins, while all other aspect of the protocol remained identical. In most studies, one eye is treated and the contralateral eye served as control. In the *in vivo* glutamate antagonist experiments and AAV experiments, LIOH was performed in both eyes in order to compare the effect of different reagent applications. IOP was measured with the Tonolab rebound tonometer (Colonial Medical Supply, Franconia, NH).

Immunohistochemistry

Samples were processed as described in the preceding chapters, unless otherwise stated. The primary antibodies used in this study are listed with manufacturers as follows. From Synaptic Systems (Goettingen, German) I obtained rabbit anti-VGLUT2 (1:400), rabbit anti-Synaptotagmin-1, lumenal and cytoplasmic domains (1:100). From Developmental Studies Hybridoma Bank (University of Iowa) I obtained mouse anti-SV2 (1:200). From Millipore (Bedford, MA) I obtained rabbit anti-Synaptophysin (1:300), rabbit anti-glutamate (1:50), rabbit anti-GluR1 (1:500), mouse anti-GluR2 (1:500), rabbit anti-NR1 (AB1516, 07-362-MN, 1:100), rabbit anti-AGB (1:300), mouse anti-NeuN (1:500). From Sigma (St. Louis, MO) I obtained mouse anti-GFAP (1:400). From Molecular Probes (Eugene, OR) I obtained rabbit anti-green fluorescent protein (GFP) (Alexa Fluor 488-conjugated, 1:100). From Covance Research Products (Denver, PA) I obtained mouse anti-neurofilament (SMI312, 1:500), mouse anti-tubulin β -III (Tuj, 1:500), mouse anti-SNAP-25 (1:500). From Abcam (Cambridge, MA) I obtained rabbit anti-VAMP2 (1:500).

Quantification of Fluorescence in Confocal Images

Confocal images were acquired as described in Chapter 2. In experiments comparing signal intensity between different treatment groups, all samples were processed in parallel and imaged under identical microscope settings. The mean pixel intensity over randomly selected ROIs was measured using ImageJ (NIH) and averaged across at least three sections for each sample.

Immuno-Electron Microscopy

Mice were anesthetized and perfused with 4% paraformaldehyde and 2% glutaraldehyde in 0.1 M phosphate buffer (PB; pH7.4). ONH tissues were dissected, postfixed in 2% osmium tetroxide for 1h followed by 2% uranyl acetate, dehydrated in an ascending series of alcohol washes, and embedded in epoxy resin. Ultrathin sections (80 nm) were collected on nickel grids covered with a Butvar support film, and stained with Synaptophysin antibodies (1:300; Millipore, Bedford, MA). Bound primary antibodies were detected with goat anti-rabbit IgG conjugated to 10 nm gold particles (Aurion, Wageningen, The Netherlands). Sample embedding, sectioning and processing for immunogold labeling were performed at the UCSF Electron Microscopy Lab by Larry Ackerman. Sections were examined and photographed with a JEOL 100CX-II microscope (JEOL Ltd., Tokyo, Japan) at 80 kV accelerating voltage.

Synaptotagmin Labeling Assay

Mice were euthanized with pentobarbital overdose, and the eyeballs with optic nerve attached were removed and placed into ice cold HEPES-buffered artificial cerebrospinal fluid (aCSF) containing (in mM): 140 NaCl, 3 KCl, 1 MgCl₂, 1 CaCl₂, 10 HEPES, 10 glucose, pH 7.4. The relatively long segment of optic nerve was dissected intact to minimize antibody reaching ONH via diffusion through the axonal cut end. The meninges encasing the nerve was carefully dissected away to enable reagent penetration. The cornea and iris were removed, while the lens was left in place to maintain the shape of eye cup until after fixation. Dissected tissues were transferred into

pre-equilibrated bicarbonate-buffered aCSF containing (in mM): 126 NaCl, 3 KCl, 2 CaCl₂, 2 MgSO₄, 1.25 NaH₂PO₄, 26 NaHCO₃, 10 glucose, pH 7.4. The samples were incubated in a standard 37°C cell culture incubator for 1 h. In the no stimulation experiment, normal aCSF was used. In the high K⁺ condition, NaCl was replaced with 40 mM KCl. K⁺/0-Ca²⁺ solution was made from this buffer by omitting CaCl₂ and adding 1 mM EGTA. In the hypertonic sucrose condition, 800 mM sucrose was added. After incubation, the samples were washed in HEPES-aCSF, and incubated with luminal domain or cytoplasmic domain Synaptotagmin antibodies (SYT-lum or SYT-cyto; 1:100; Synaptic Systems, Germany) in HEPES-aCSF on ice for 8 h. This temperature was chosen to minimize uptake of antibodies into the axons by endocytotic means. Following washing, labeled tissues were fixed in 4% PFA at room temperature for 30 min, and processed for cryosectioning as previously described. The eye cups were cut into 12 µm longitudinal sections, and every third one was collected onto the same slide. Only sections through the optic nerve head were kept, yielding 5 per slide to be analyzed. Non-specific binding was blocked by 10% NDS for 1 h at room temperature, without detergent permeabilization. Detection of bound Synaptotagmin antibodies was carried out by incubation with cy3-conjugated secondary antibodies (Jackson ImmunoResearch, West Grove, PA). As negative controls, tissues were incubated with secondary antibodies or dextran (3000 MW) conjugated tetramethylrhodamine (TMR) to rule out non-specific uptake of reagents into the axoplasm. No staining was found in negative controls.

Fluorescence images were acquired by confocal microscopy and analyzed with ImageJ (NIH). Some non-specific staining of blood vessels at the ONH was observed, which was clearly distinguishable from axonal labeling. Four 50x50 µm regions of

interest (ROIs) were placed over each image, avoiding inclusion of blood vessels in the analysis. Mean pixel intensity was measured and averaged across the ROIs. In most cases, 5 sections were analyzed and averaged for each eye sample. To allow for direct comparison of different experiments, data in each experiment were normalized against the SYT-cyto control (no LIOH) sample for Fig. 4-6E and F. For Fig. 4-6G, only LIOH samples were studied using SYT-lum, and data were normalized against the no stimulation condition.

Pilot experiments were performed with secondary antibody detection in whole-mounted ONH following primary antibody incubation and PFA fixation. Confocal reconstruction of the ONH tissue in *z*-stacks (*n* = 7) demonstrated Synaptotagmin labeling only with the SYT-lum antibody, similar to results obtained from cryosections. These pilot data were not included in the quantification due to relatively poor signal-to-noise ratio.

Glutamate Detection with NADH Assay

ONH tissues were quickly dissected in HEPES-buffered aCSF, and cut into halves along the longitudinal axis. One half of the tissue was immobilized with a slice anchor in the imaging chamber, and bathed in an enzymatic assay solution composed of (in mM) 120 NaCl, 2.6 KCl, 1 MgCl₂, 2.5 CaCl₂, 1 D-aspartic acid, 10 HEPES, 10 glucose, and supplemented with NAD (4 mM) and GDH (60 mM, Roche Applied Science; Indianapolis, IN), pH 7.4. Imaging experiments were performed at room temperature on an inverted microscope (TE300; Nikon, Tokyo, Japan) equipped for epifluorescence

microscopy. Excitation from a xenon arc lamp was filtered through an ultraviolet filter set (UV-2E/C; Nikon). Fluorescence images were captured at 1 min intervals using a CCD camera (Retiga EXi; QImaging, Surrey, BC, Canada) controlled by SimplePCI software (Hamamatsu, Sewickley, PA). After equilibration of tissue in the enzymatic solution for ~3 min, baseline fluorescence images were collected for 5-6 min, followed by bath stimulation with an assay solution containing high K⁺ (substituting NaCl in the previous buffer with 100 mM KCl) or hypertonic sucrose (addition of 800 mM sucrose). Image acquisition continued for another 10 min after stimulation. Data were processed using the NIH ImageJ software. In pilot studies, considerable photobleaching of fluorescence signal was observed. Raw images were thus corrected for bleaching using the “bleach correction” plugin for ImageJ. The exponential decay constant was calculated from control experiments in which tissues were imaged without stimulation. Following background subtraction, five regions of interest (ROIs) were randomly selected over the ONH in each image. The mean pixel intensity in these ROIs was measured and averaged. In order for experiments conducted on different days to be compared, the change in fluorescence was expressed as $\Delta F/F_0$, in which F_0 was the baseline fluorescence and ΔF was the change in fluorescence intensity at each time point after stimulation²⁷⁹. Statistical analysis was performed using two-way ANOVA followed by Bonferroni posttests.

Agmatine (AGB) Activation Assay

Anesthetized mice received bilateral 20 μ l injection of 25 mM AGB (Agmatine; Sigma, St. Louis, MO) into the subconjunctival space. This method delivered AGB to the

ONH to examine ionotropic glutamate receptor activation *in vivo*. After 2 h of survival time, eye cups were quickly dissected, washed briefly in HEPES-buffered aCSF, and fixed in 4% PFA with 0.01% glutaraldehyde in 0.1 M phosphate buffer (PB; pH 7.4) for 30 min at 4°C. After washing for 15 min in PB at room temperature with shaking, the eye cups were processed for immunohistochemistry. Cryosections were blocked in 6% NDS with 0.5% Triton X-100 for 1 h at room temperature, followed by primary antibody (anti-Agmatine; 1:300; Millipore, Bedford, MA) incubation in 3% NDS and 0.5% Triton X-100 at 4°C overnight.

Fluorescence confocal images were analyzed with ImageJ (NIH). Identical parameters were used to set the threshold of fluorescence for the control and treatment groups. Area of the AGB signal in each ONH section was then measured and averaged. Data from the LIOH-treated ONHs were normalized against the contralateral control sample from the same animal. For the AAV experiments, only AGB signal in axons were quantified. To do this, sections were co-immunostained for AGB and tubulin. The image channel containing tubulin immunoreactivity was binarized and used to create a mask, within which AGB-positive area was measured. The data were then calculated as area of AGB immunoreactivity divided by tubulin immunoreactivity, to obtain a measure of the extent of AGB activation within axons. Results from each pairs of AAV-injected eyes were normalized against the AAV-GFP condition.

Organotypic Culture of Optic Nerve Explants

Optic nerve explants were cultured with retinas attached, so that RGC axons were not severed from their cell bodies, prolonging survival *in vitro*. In addition, the cellular architecture and potential interactions within the optic nerve were preserved by this approach, providing a more physiologically-relevant environment. The mouse eyeball with its connected optic nerve was quickly removed, and the anterior segment, sclera, and meninges were dissected away in cold HEPES-buffered aCSF. Complete removal of meninges around ONH required great care so as not to damage the nerve. The explant was rinsed briefly with pre-equilibrated growth media containing Neurobasal-A supplemented with B-27 and Penicillin-Streptomycin (Invitrogen, Carlsbad, CA), and transferred onto a Millicell organotypic culture insert (Millipore, Bedford, MA). One primary cut was made from the retinal periphery to the ONH, and the retina (GCL facing up) was spread out flat on the Millicell insert with a custom-made ball-headed instrument. To ensure sufficient gas exchange, this tissue was arranged so that the optic nerve is not covered by the retina, while being kept moist during the entire procedure. After removal of excessive growth media, the insert was placed into a 6-well plate filled with growth media. Culture was inspected everyday to make sure a thin film of media remained over the explant, and media change occurred every two days.

Control optic nerves were used for the *in vitro* glutamate application experiment. Growth media were supplemented with different concentrations of glutamate or vehicle. After 3 days *in vitro*, the explants were fixed in 4% PFA, cryosectioned, and stained with anti-neurofilament (SMI312; 1:500; Covance Research Products, Denver, PA).

In the glutamate antagonist treatment experiment, optic nerves were explanted 2 days after LIOH, along with the contralateral controls. A cocktail of NBQX (50 μ M;

(Tocris Bioscience, Ellisville, MO) and MK-801 (50 uM; Tocris) or Tetrodotoxin (TTX; 30 uM; Tocris) was added to the growth media. Samples were harvested after 5 days *in vitro* and processed for immunohistochemistry.

Fluorescence images were analyzed with ImageJ, and the thresholded area of neurofilament immunoreactivity was determined as a measure of axon survival.

***In vivo* Glutamate Antagonist Treatment**

Mice were anesthetized one day after LIOH treatment. The conjunctiva was surgically opened, and the optic nerve was exposed by retracting intraocular muscles with blunt forceps. A small piece of gelfoam soaked in 3 ul of reagents was locally delivered to the ONH, and held in place underneath intraocular muscle fibers. One eye was treated with a drug cocktail containing NBQX (500 uM; Tocris), MK-801 (500 uM; Tocris) and Tetrodotoxin (TTX; 300 uM; Tocris), whereas vehicle was delivered to the fellow eye. Bacitracin antibiotic ointment was administered after surgery. Eyes with postoperative infection were excluded from the study. Optic nerves were harvested 6 days post-surgery, and analyzed by counting axons in PPD-stained cross sections.

Recombinant AAV Vectors

The Cre- or GFP-expressing recombinant adeno-associated virus (rAAV) vectors were generous gifts from Dr. Zhigang He at Harvard Medical School. They were constructed by inserting *Cre* recombinase or *GFP* cDNA into the pAAV-MCS plasmid

containing AAV2 inserted terminal repeats (Stratagene), as described previously²⁸⁰. Viral particles were produced, purified, and titered by the University of North Carolina Vector Core Facility.

Intravitreal Injection

Albino floxed mice were anaesthetized with ketamine and xylazine. One eye was injected intravitreally with 1 ul of AAV-Cre (2×10^{12} particles per ml), and the fellow eye was injected with AAV-GFP (1.5×10^{12} particles per ml) control. The eye was first punctured lightly with a 30 gauge hypodermic needle just behind the ora serrata. A custom-made 32 gauge needle (1'' long, pt4) attached to a 10 ul syringe (Hamilton, Reno, NV) was then inserted into the vitreous cavity, and angled carefully to avoid damage to the lens. Viral particles were dispensed slowly over one minute, after which the needle was left in place for an additional minute to allow for diffusion of the virus. Three weeks following viral injection, LIOH was performed on both eyes of the injected mice.

Statistical Analysis

The Synaptotagmin assay, and *in vitro* glutamate application data were evaluated with one-way analysis of variance (ANOVA) followed by Tukey's multiple comparison test. Data from the NADH assay, *in vitro* glutamate antagonist treatment, and axon counting in AAV experiment were analyzed with two-way ANOVA followed by post hoc Bonferroni multiple comparison test. Results from the AGB assay, *in vivo* glutamate antagonist treatment, and VGLUT2/glutamate level in AAV experiment were evaluated

with t-test. Statistical analysis was performed using the GraphPad Prism (version 5) software, with a significance level set at $p < 0.05$. Values were reported as mean \pm SEM.

Results

Ectopic Accumulation of Synaptic Vesicle Proteins at the Glaucomatous ONH

The ONH is a normally a non-synaptic region; however, after the induction of experimental glaucoma, several well-established synaptic vesicle makers were found to exhibit a striking accumulation at the ONH. As shown in Fig. 4-1A and D, SV2 and Synaptophysin were strongly expressed in the control retinal IPL and OPL layers as expected²⁸¹⁻²⁸², while showing only faint and diffuse staining in the normal optic nerve. In contrast, dramatic increase of immunoreactivity was observed at the ONH after LIOH in CD-1 mice (Fig. 4-1B and 1E). Comparable levels of staining in the retinas of control and LIOH samples confirm that matching parameters were used to acquire the images. RGCs are glutamatergic neurons, which require vesicular glutamate transporters (VGLUTs) to fill their synaptic vesicles with glutamate²⁸³. Previous studies have shown that VGLUT2 is the major isoform expressed by RGC somas in the retina^{281,284-289}, and is present on RGC axon terminals in the lateral geniculate nucleus (LGN)^{286,290-291}. In control CD-1 mouse retina, VGLUT2 immunohistochemistry faintly labeled the IPL and OPL, consistent with previous reports of weak expression in Muller glia and cone photoreceptors^{281,285-289,291}. Similar to SV2 and Synaptophysin, VGLUT2 immunostaining was largely absent from the normal ONH (Fig. 4-1G), but became strongly upregulated after LIOH (Fig. 4-1H). To determine whether these observations hold true in an alternative glaucoma model, I also examined 10-month old DBA/2J mice

that exhibited optic nerve degeneration (“cupping”). Similar patterns of ectopic expression by all synaptic vesicle markers were also documented (Fig. 4-1C, F, and I).

These experiments had been repeated extensively in LIOH, and the ectopic accumulation of synaptic vesicle proteins could be consistently observed as early as 2 days after treatment, and persisted beyond 2 weeks. The immunostaining was remarkably concentrated at the ONH region, although in the most extreme cases it could extend somewhat into the myelinated optic nerve. The intensity of labeling tended to diminish after 1 week, as axonal degeneration progressed. Most experiments in this study were performed on samples harvested between 2 and 4 days after LIOH.

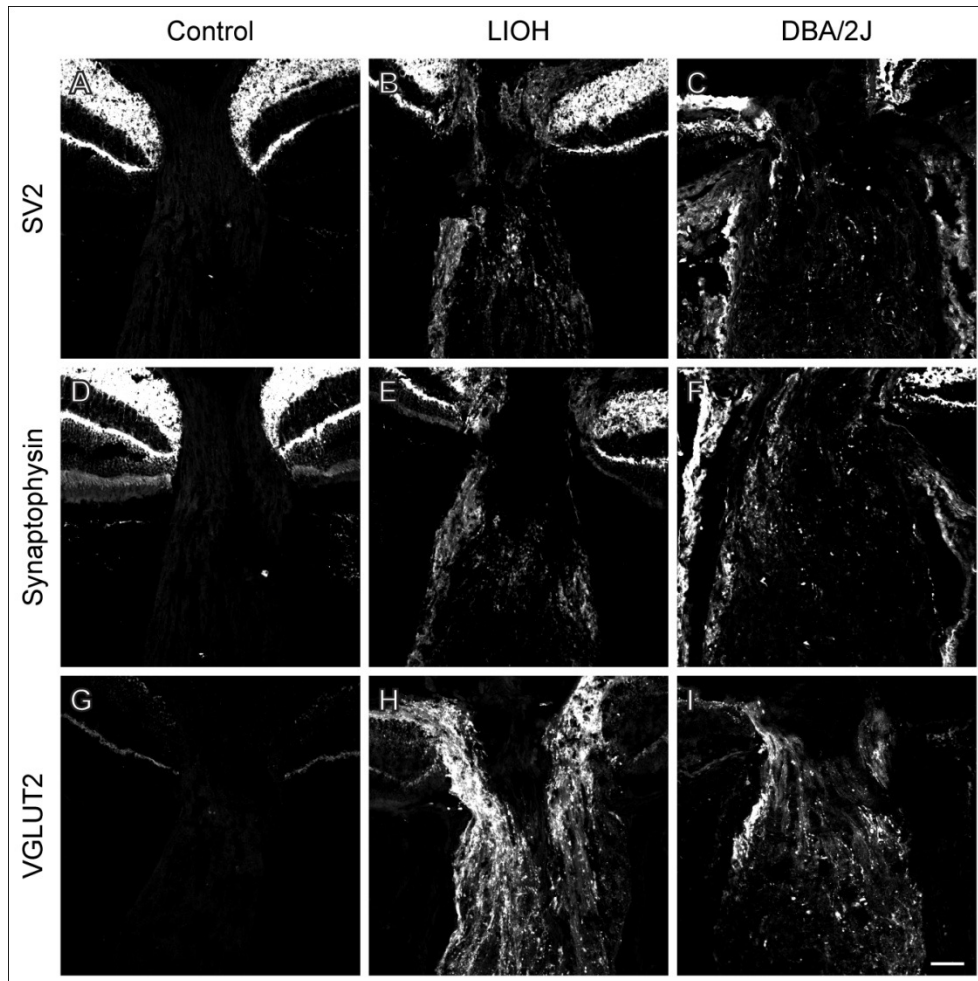


Figure 4-1. Ectopic accumulation of synaptic vesicle markers at the ONH after LIOH

Frozen sections of control and LIOH eye cups were immunostained with antibodies against synaptic vesicle proteins, including SV2 (**A-C**), Synaptophysin (**D-F**), and VGLUT2 (**G-I**). All three markers show only faint and diffuse staining in the optic nerve of controls (**A, D, G**), but exhibit dramatic accumulation at the ONH of LIOH samples (**B, E, H**; shown here at 4 days post-treatment). Comparable levels of labeling in the retina confirm that the control and LIOH samples were processed identically. DBA/2J eye cups that demonstrate signs of degenerative “cupping” are also found to display similar accumulation of all three markers at the ONH (**C, F, I**). Scale bar: 50 μm . Experiments were repeated > 60 times for SV2, > 20 times for Synaptophysin and > 30 times for VGLUT2.

Ectopic Synaptic Vesicle Proteins Are Localized to RGC Axons But Not Astrocytes

To determine the cellular origin of ectopic synaptic vesicle proteins at the glaucomatous ONH, triple labeling experiments were performed for VGLUT2 (Fig. 4-2A), GFAP (Fig. 4-2B, astrocytic marker), and tubulin β -III (Fig. 4-2C, axonal marker). VGLUT2 immunoreactivity co-localized with tubulin (Fig. 4-2D, arrowheads) but not GFAP (Fig. 4-2D, arrows), suggesting that ectopic VGLUT2 accumulation after LIOH was present in RGC axons rather than astrocytes. Ectopic SV2 and Synaptophysin were found to have the same patterns of cellular localization (Supplemental Fig. 4-15).

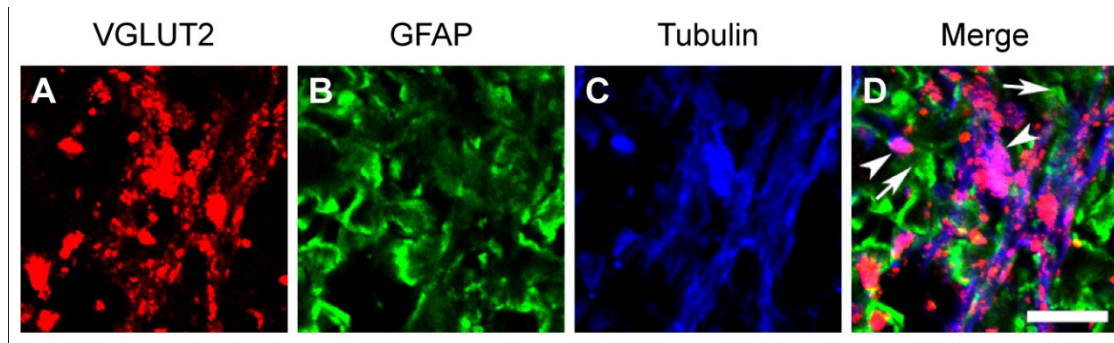


Figure 4-2. Ectopic VGLUT2 is present in axons but not astrocytes at the glaucomatous ONH

Eye cup sections collected 4 days after LIOH were immunostained for VGLUT2 (A), GFAP (B), and tubulin β -III (C). Regions within the ONH were imaged. VGLUT2 co-localizes with the axonal marker tubulin (D, arrowheads) but not the astrocytic marker GFAP (D, arrows). Scale bar: 50 μ m. n = 6 experiments.

Ultrastructural Detection of Synaptophysin-positive Vesicles in Axons at the Glaucomatous ONH

Post-embedding immuno-electron microscopy (immuno-EM) was performed to examine the ultrastructural localization of ectopic synaptic vesicle proteins observed at the light microscopy level. Synaptophysin was chosen as a representative marker based on the robustness of our available antibody reagent. Contrary to the orderly array of tightly packed RGC axons in the control ONH (Fig. 4-3A), LIOH resulted in disorganization of axon fibers and appearance of large swellings with massive accumulation of membrane-bound organelles. The contents of these enlargements were heterogeneous and variable. In Fig. 4-3B, mitochondria (M), multilamellar bodies (MLB), translucent vesicles (V), and dense core vesicles (DCV) could be observed. Fig. 4-3C shows another swollen axonal segment, which mainly contained densely packed translucent (V) and dense core (DCV) vesicles in close apposition to the axolemma. The

translucent vesicles were strongly labeled with immunogold particles, suggesting that they contain Synaptophysin (Fig. 4-3E, F, H). Only sparse gold particles were observed on control sections (Fig. 4-3D). Translucent vesicles were occasionally found in the control axons, in association with immunogold labeling (Fig. 4-3G, arrow); however, these instances occurred at much lower frequency compared to the LIOH samples. Some Synaptophysin-positive translucent vesicles are shown in higher magnification in Fig. 4-3H. The cluster of vesicles clearly abutted the axolemma (arrows). There appeared to be patches of electron-dense materials along the plasma membrane, reminiscent of the cytomatrix of active zones (Fig. 4-3H, arrowheads; also in Fig. 4-3F). The extracellular space between the swollen axon and its neighboring cell was narrow, but the membranes were often not precisely aligned. Underlying the juxtaposed membrane, we did not find clear indication of specializations analogous to a post-synaptic density area. Intense immunogold labeling was also observed along the axolemma of some axons (Fig. 4-3I, arrows), consistent with fusion of Synaptophysin-positive vesicles with the plasma membrane.

In summary, immuno-EM confirmed the presence of SV protein-expressing vesicles at the ONH following LIOH, in accordance with the previous immunofluorescence studies. The morphology of these organelles appears different from the small vesicles found at classical synapses. Synaptic vesicles mature in the axonal terminals, and they are often spherical and uniformly-sized. In contrast, the ectopic vesicles are more variable in size and shape, measuring 64.0 ± 15.9 nm in length and 50.2 ± 13.0 nm in width. These may represent SV protein-containing precursors during axonal transport (see Discussion).

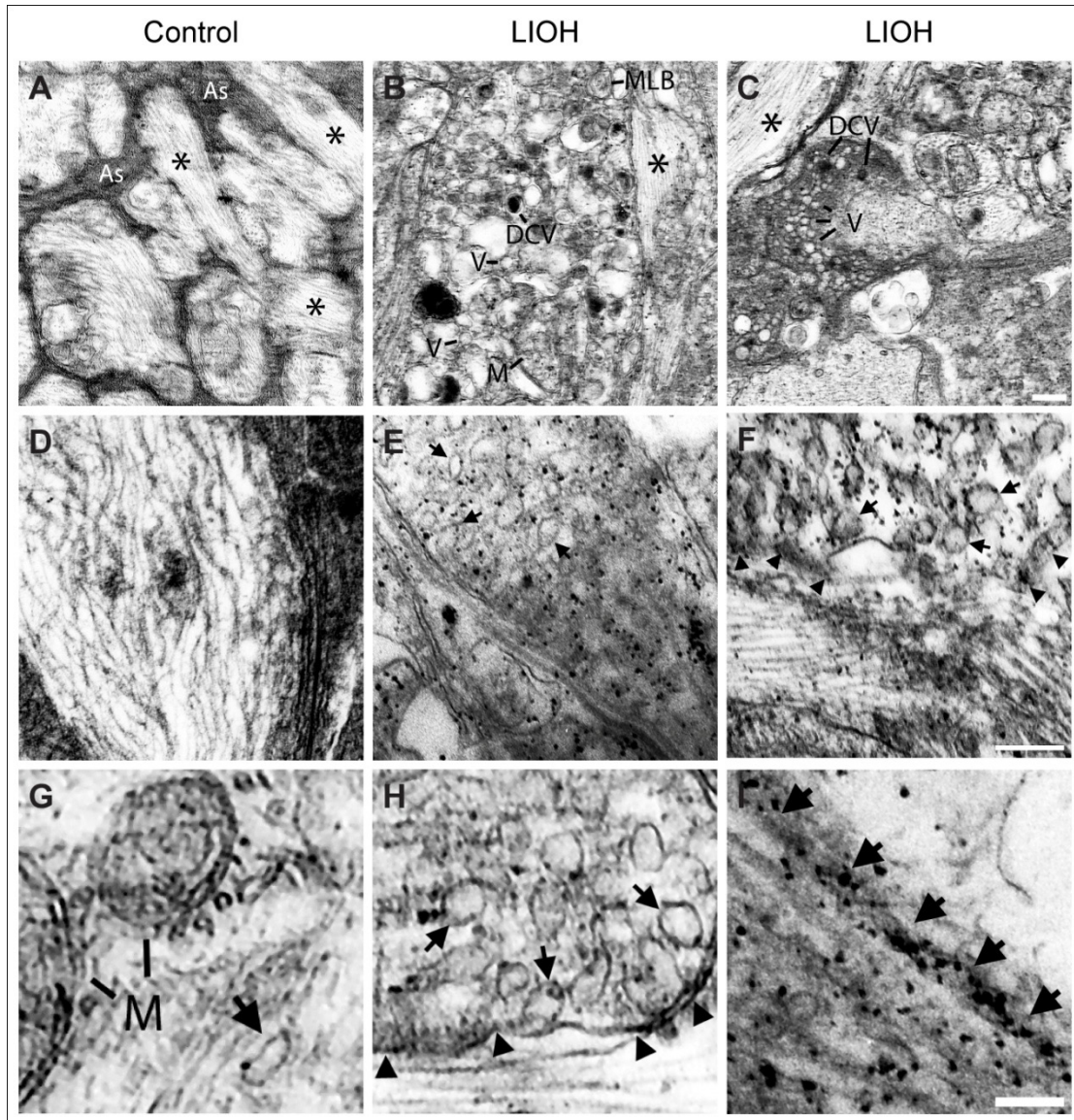


Figure 4-3. Ultrastructural analysis reveals the presence of Synaptophysin-positive vesicles at the ONH after LIOH

ONH tissues harvested 2 days after LIOH were processed for electron microscopy along with the control. Antibodies directed against Synaptophysin were used in post-embedding immunogold labeling. (A) Control ONH. Unmyelinated RGC axon fibers (asterisks) are highly organized and in close association with astrocyte processes (As). (B, C) LIOH ONH. Axon fibers become disorganized, and often display swollen regions densely packed with membrane-bound organelles, including mitochondria (M), multilamellar bodies (MLB), translucent vesicles (V), and dense core vesicles (DCV). The translucent vesicles are sometimes scattered among other organelles (B) and sometimes aggregated in close apposition to the axolemma (C). Asterisks indicate neighboring axons that appear similar to the normal fibers in control. (D-I) Higher magnification electron micrographs to visualize immunogold labeling. (D) Only sparse gold particle labeling is

seen in the control. (E, F) Intense labeling over translucent vesicle clusters (arrows) in LIOH. Arrowheads in F point to electron dense areas in association with the vesicles. (G) Vesicles are occasionally observed in control axons (arrow). (H) Another example of Synaptophysin-positive vesicles (arrows), demonstrating electron dense regions (arrowheads) along the abutting axolemma. (I) Heavy immunogold staining along the axolemma of one axon (arrows). M, mitochondria; MLB, multilamellar bodies; V, translucent vesicles; DCV, dense core vesicles. Scale bars: A-C, 300 nm; D-F, 200 nm; G-I, 100 nm.

Glutamate Is contained in Ectopic Vesicles and Upregulated at the Glaucomatous

ONH

Glutamate is the major excitatory neurotransmitter in the retina, mediating transmission in the vertical pathway from photoreceptors, bipolar cells, and RGCs²⁹². The accumulation of ectopic SV protein-expressing vesicles in glaucomatous RGC axons raises the question whether they contain glutamate like their normal counterparts. An immuno-detection study was performed on frozen eye cup sections using polyclonal antibodies raised against glutamate. Control optic nerves exhibited only weak and diffuse staining (Fig. 4-4A). After LIOH, glutamate immunoreactivity was markedly upregulated at the ONH (Fig. 4-4D). Double-staining with SV2 as a marker for ectopic vesicles demonstrated that glutamate and SV2 extensively co-distribute (Fig. 4-4F). Higher magnification of an ONH region (Fig. 4-4F inset) revealed that similar to SV2, glutamate was not evenly distributed within RGC axons, but was instead concentrated in discrete “hotspots” intensely immunolabeled. While a few SV2-positive (SV2⁺) “hotspots” were devoid of glutamate (Fig. 4-4F inset, arrow), most were indeed found to co-localized. Interestingly, glutamate-positive (glutamate⁺) “hotspots” were often slightly larger than the corresponding SV2⁺ hotspots (arrowheads). There were also glutamate

immunoreactive regions that were not stained with SV2 (open arrowhead). These observations would be consistent with a scenario in which glutamate could be released from the ectopic vesicles, and enter the extracellular space.

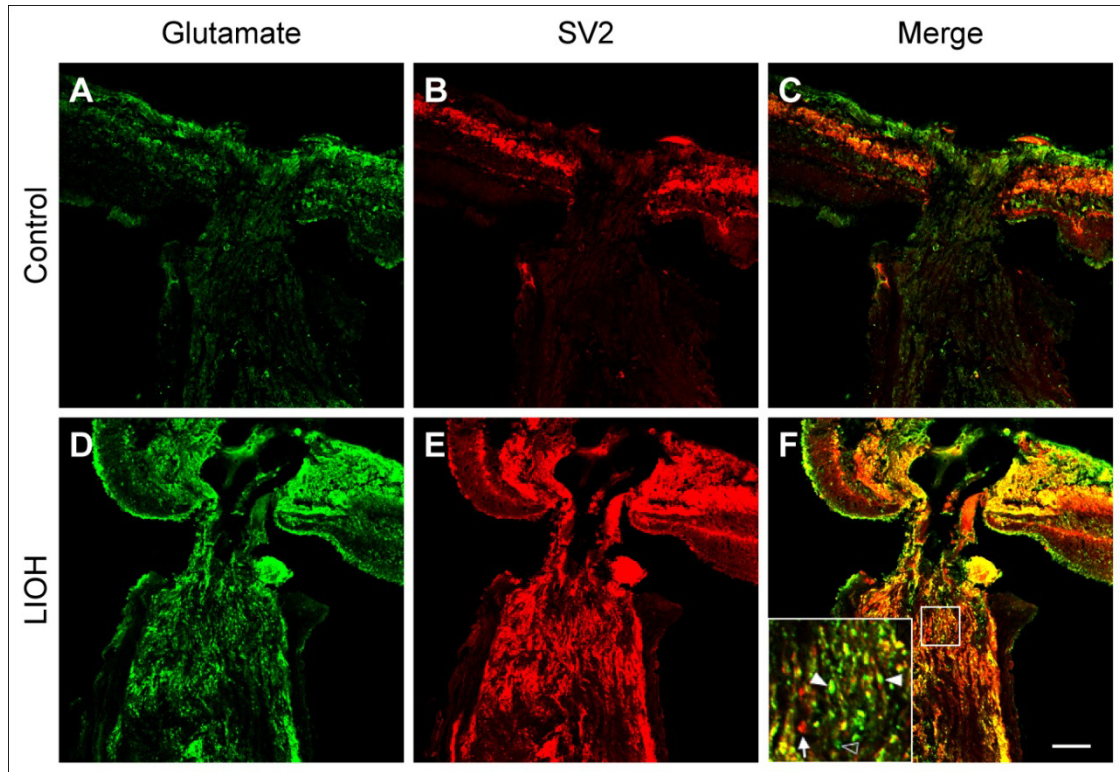


Figure 4-4. Immuno-detection of glutamate at the ONH

In control samples, glutamate (A) and SV2 (B) immunoreactivities are similarly weak and diffuse. LIOH treatment results in dramatic ONH accumulation of both glutamate (D) and SV2 (E), which are co-localized extensively (F). High magnification inset taken from the boxed region demonstrates that glutamate and SV2 are found in “hotspots” along the RGC axons. Although a few of these “hotspots” are only labeled with SV2 (arrow) or glutamate (open arrowhead), in most instances the two markers overlap, with the glutamate “hotspots” being slightly larger (arrowheads). Scale bar: 50 μ m. n > 13 pairs of CD-1 eyes. A LIOH day 4 sample is shown here.

Ectopic Vesicles Partially Co-localize with SNAP-25 and Bassoon

Exocytosis of synaptic vesicles requires the presence of membrane fusion machineries, including the soluble *N*-ethylmaleimide-sensitive factor attachment protein (SNAP) receptor (SNARE) complex²⁹³. Formation of the SNARE complex involves three core components: v-SNARE protein synaptobrevin (vesicle-associated membrane protein; VAMP) located on the synaptic vesicles and t-SNARE proteins associated with the target membrane including syntaxin-1 and SNAP-25. I examined the expression of SNAP-25 in RGC axons at the ONH where ectopic vesicles are accumulated, to address the question whether they might be competent for exocytosis. In addition to strong labeling in both synaptic layers in the retina, SNAP-25 was also robustly and uniformly expressed in RGC axons within the control optic nerve (Fig. 4-5A). After LIOH, the optic nerve expression of SNAP-25 was largely preserved, although the immunolabeling pattern became somewhat patchy, reflecting the disorganization of glaucomatous axons (Fig. 4-5B). Co-labeling of VGLUT2 with SNAP-25 in LIOH ONH samples showed that the majority of ectopic VGLUT2 immunoreactivity overlapped with SNAP-25 (Fig. 4-5G, arrowheads). SNAP-25 appeared to be more widely distributed, consistent with its uniform expression in control RGC axons (arrows in Fig. 4-5G pointing to regions expressing SNAP-25 but not VGLUT2). Occasional spots of VGLUT2 immunoreactivity were not co-labeled with SNAP-25 (Fig. 4-5G, open arrowheads), perhaps corresponding to severely degenerating axonal segments.

At a mature synapse, the presynaptic terminal is organized into a highly specialized active zone to facilitate neurotransmitter release. A large scaffolding protein called Bassoon has been identified as a key component of the cytomatrix at the active zone (CAZ)²⁹⁴. It associates with the cytoskeleton and participates in anchoring proteins

to the active zone and regulating neurotransmitter release in some synapses²⁹⁵⁻²⁹⁷. Immuno-staining of Bassoon labeled the retinal IPL and OPL as shown previously^{296,298}, but only gave rise to weak signal in the control optic nerve (Fig. 4-5C). LIOH treatment led to an accumulation of Bassoon immunoreactivity at the ONH (Fig. 4-5D). The labeling pattern was heterogeneous like the ectopic SV proteins, with immunoreactive patches ranging in size from intensely stained large axon bundles (Fig. 4-5D, rectangular dashed box), to smaller “hotspots” interspersed along the axons like “beads on a string” (Fig. 4-5D, oval dashed box). The majority of Bassoon and VGLUT2 labeling co-localized (Fig. 4-5J, see arrowheads in inset); however, “hotspots” predominantly immunoreactive for VGLUT2 (Fig. 4-5J inset, arrow) or Bassoon (Fig. 4-5J inset, open arrowhead) were also found.

I also examined the distribution of VAMP2, a neuronal isoform of v-SNARE. The immuno-staining pattern of VAMP2 was indistinguishable from SV2 and Synaptophysin in both control and LIOH ONHs. Extensive co-localization of VAMP2 with SNAP-25 was also observed (Supplemental Fig. 4-16).

These data suggest that at least a portion of the VAMP2-expressing ectopic vesicles co-localize with SNAP-25 and Bassoon, and thus may have access to SNARE and CAZ machineries that could facilitate their fusion with the axolemma.

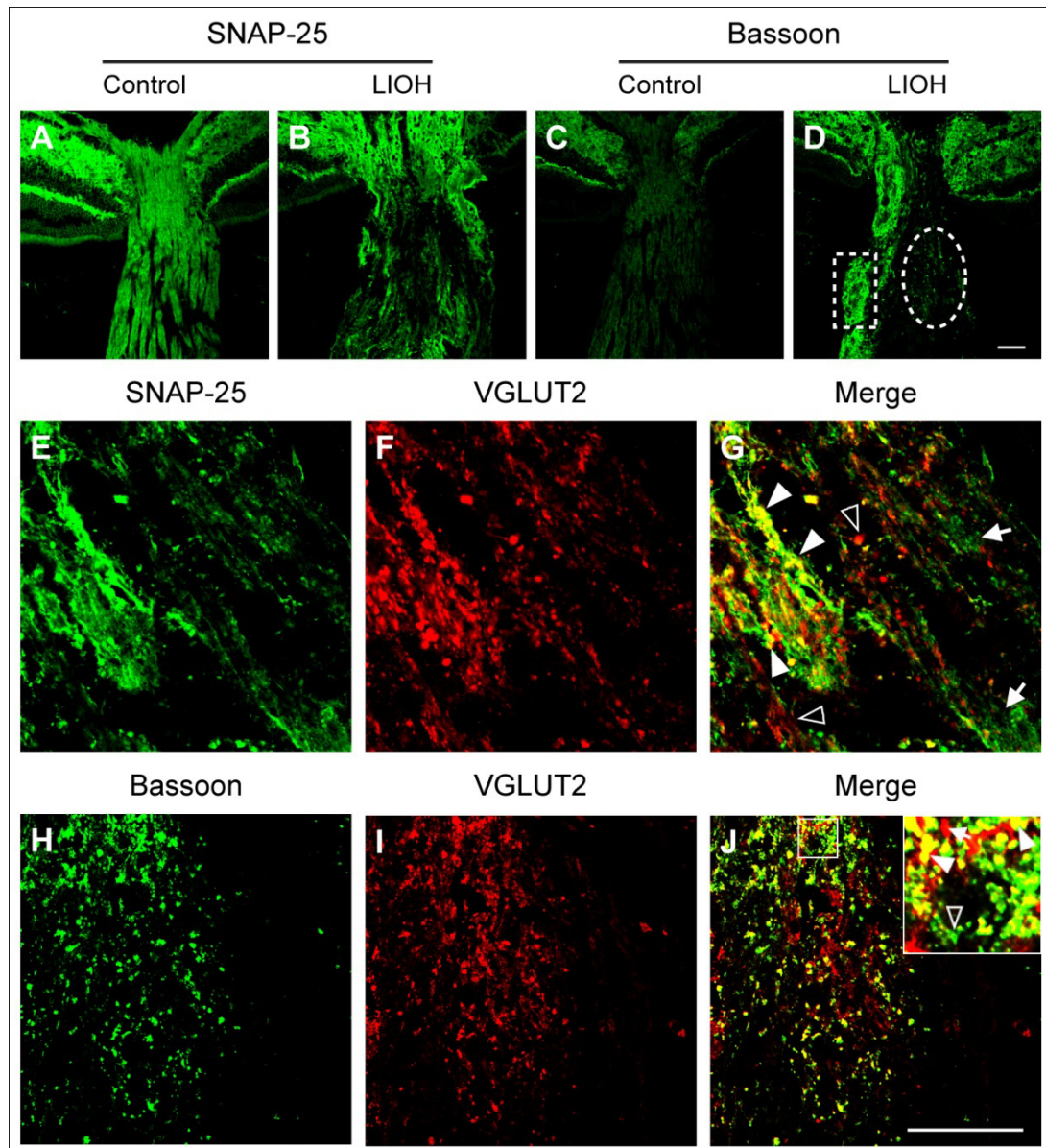


Figure 4-5. SNAP-25 and Bassoon are present at the LIOH ONH and partially overlap with VGLUT2

(A, B) SNAP-25 immunohistochemistry. SNAP-25 is expressed in both control (A) and LIOH (B) optic nerve. (C, D) Bassoon immunohistochemistry. Bassoon labeling is weak in the control optic nerve (C), but becomes strongly upregulated after LIOH (D). Rectangular and oval dashed boxes denote large immunoreactive axon bundles and smaller “hotspots,” respectively. (E-G) Co-labeling of SNAP-25 (E) and VGLUT2 (F). The two markers are extensively co-localized (G, arrowheads), although some areas are only labeled for SNAP-25 (arrows) or VGLUT2 (open arrowheads). (H-J) Co-labeling of Bassoon (H) and VGLUT2 (J) imaged from an ONH region similar to the oval dashed box in (D). A large proportion of Bassoon and VGLUT2 immunoreactive “hotspots” overlap (J). Inset in (J) is a high magnification image taken from the boxed region,

showing examples of co-localization (arrowheads), as well as “hotspots” predominantly labeled for VGLUT2 (arrow) or Bassoon (open arrowhead). Scale bar: 50 μm . n = 12 for SNAP-25 and n = 6 for Bassoon.

Ectopic Vesicles Can Undergo Exocytosis

To demonstrate that exocytosis of ectopic vesicles actually occurs, I took advantage of a pair of antibody reagents directed against the SV protein synaptotagmin-1, which serves as a Ca^{2+} sensor for exocytosis. Synaptotagmin-1 is composed of a N-terminal luminal domain, a transmembrane region, and two cytoplasmic C2 domains²⁹⁹. Polyclonal antibodies (commercially available) were raised against the luminal (SYT-lum) or cytoplasmic (SYT-cyto) domains of synaptotagmin-1. Following SV exocytosis in live neurons, the luminal epitope is exposed to the extracellular environment, and consequently becomes accessible to the SYT-lum antibodies. On the contrary, the cytoplasmic epitope remains inaccessible to the SYT-cyto antibodies without permeabilization. This approach has been described in previous studies to investigate SV recycling in cultured neurons, using the extent of antibody labeling as a measure of exocytotic events³⁰⁰⁻³⁰¹. I adapted the protocol for acute preparations of whole eye cup tissue, in order to study the potential exocytosis of ectopic vesicles at the ONH following LIOH. Both the SYT-lum and SYT-cyto antibodies exhibited similar patterns of ectopic accumulation at the glaucomatous ONH in detergent-permeabilized frozen sections, which mirrored the other SV protein markers tested (data not shown). In the live labeling assay, freshly dissected eye cups (including the retina and a stretch of optic nerve) were incubated at 37°C in either normal aCSF, high K^+ aCSF, high $\text{K}^+/\text{0-Ca}^{2+}$ aCSF, or hypertonic sucrose aCSF. The tissues were then labeled with either SYT-lum or SYT-

cyto antibodies on ice, and processed for cryosectioning. The bound synaptotagmin antibodies were detected with cy3-conjugated secondary antibodies without detergent permeabilization of the cryosections. A representative experiment performed with high K^+ aCSF is shown in Fig. 4-6A-D. SYT-cyto antibodies exhibited minimal staining at either the control (Fig. 4-6C) or LIOH (Fig. 4-6D) ONH, except for occasional non-specific blood vessel labeling (open arrowhead). These control conditions confirmed the specificity of SYT-cyto antibodies to the cytoplasmic domain, integrity of the live tissues, and absence of antibody diffusion into the cut-end of optic nerves. SYT-lum labeling at the control ONH was similarly minimal (Fig. 4-6A), whereas a dramatic increase of staining was observed at the LIOH ONH (Fig. 4-6B), suggesting that the synaptotagmin luminal epitope was exposed on the plasma membrane by vesicular fusion. These experiments were repeated and quantified (Fig. 4-6E-G). In Fig. 4-6E and F, The measured fluorescence intensity in each condition was normalized against the SYT-cyto sample in the same experiment, so that results across different days could be compared. The K^+ stimulation experiments (Fig. 4-6E) demonstrated that a significant level of exocytosis took place at the LIOH ONH in response to depolarization, which was not present in controls. Interestingly, the unstimulated LIOH ONH (Fig. 4-6F) also exhibited significant SYT-lum labeling above the control level, indicating that at least some exocytotic events had occurred *in vivo*. Fig. 4-6G shows a separate group of experiments conducted to compare the effect of K^+ and sucrose stimulation, and the Ca^{2+} -dependence of ectopic vesicle fusion. Only SYT-lum labeling in LIOH samples were investigated, and results were normalized against the unstimulated condition. K^+ depolarizes the neuronal membranes, and hypertonic sucrose has been shown to induce fusion of the

readily-releasable pool of synaptic vesicles³⁰²⁻³⁰³. Both K^+ and sucrose stimulation resulted in higher SYT-lum staining than normal aCSF. It suggests that in addition to exocytosis already occurring at the glaucomatous ONH *in vivo*, more vesicles are competent for fusion in response to stimulation. The ability of hypertonic sucrose to trigger exocytosis is consistent with the idea that at least some ectopic vesicles interact with the axolemma in a way similar to the “docked” configuration of classical synaptic vesicles. Eliminating Ca^{2+} from the high K^+ aCSF reduced SYT-lum labeling down to the unstimulated level, indicating that depolarization-evoked exocytosis was dependent on extracellular Ca^{2+} . The Ca^{2+} -dependence of ectopic vesicle fusion *in vivo* is not addressed by this experimental design, because presumably many fusion events had already taken place by the time the ONH tissue was harvested. To explore the relationship between exocytosed SYT-lum and SV2, co-labeling was performed following unstimulated experiments (Fig. 4-6H-J). Since the SV2 antibodies were directed against a cytoplasmic epitope, permeabilization was carried out on cryosections to enable immuno-detection. As a result, the SV2 staining presumably accounts for both un-fused and fused vesicles. Some of these un-fused vesicles were represented by SV2 immunoreactive regions devoid of SYT-lum staining (Fig. 4-6J, arrowhead). Most of the SYT-lum labeling overlapped with SV2 (Fig. 4-6J, arrows), indicating the exocytosed portion of vesicles. A few SYT-lum⁺ areas were SV2⁻ (Fig. 4-6J, open arrowhead), which either suggests not all SV proteins co-exist on the same ectopic vesicles, or reflects the differential sensitivity of antibody reagents.

Over all, these results indicate that at least a portion of ectopic vesicles can be exocytosed *in vivo*, as well as undergoing evoked fusion *ex vivo*.

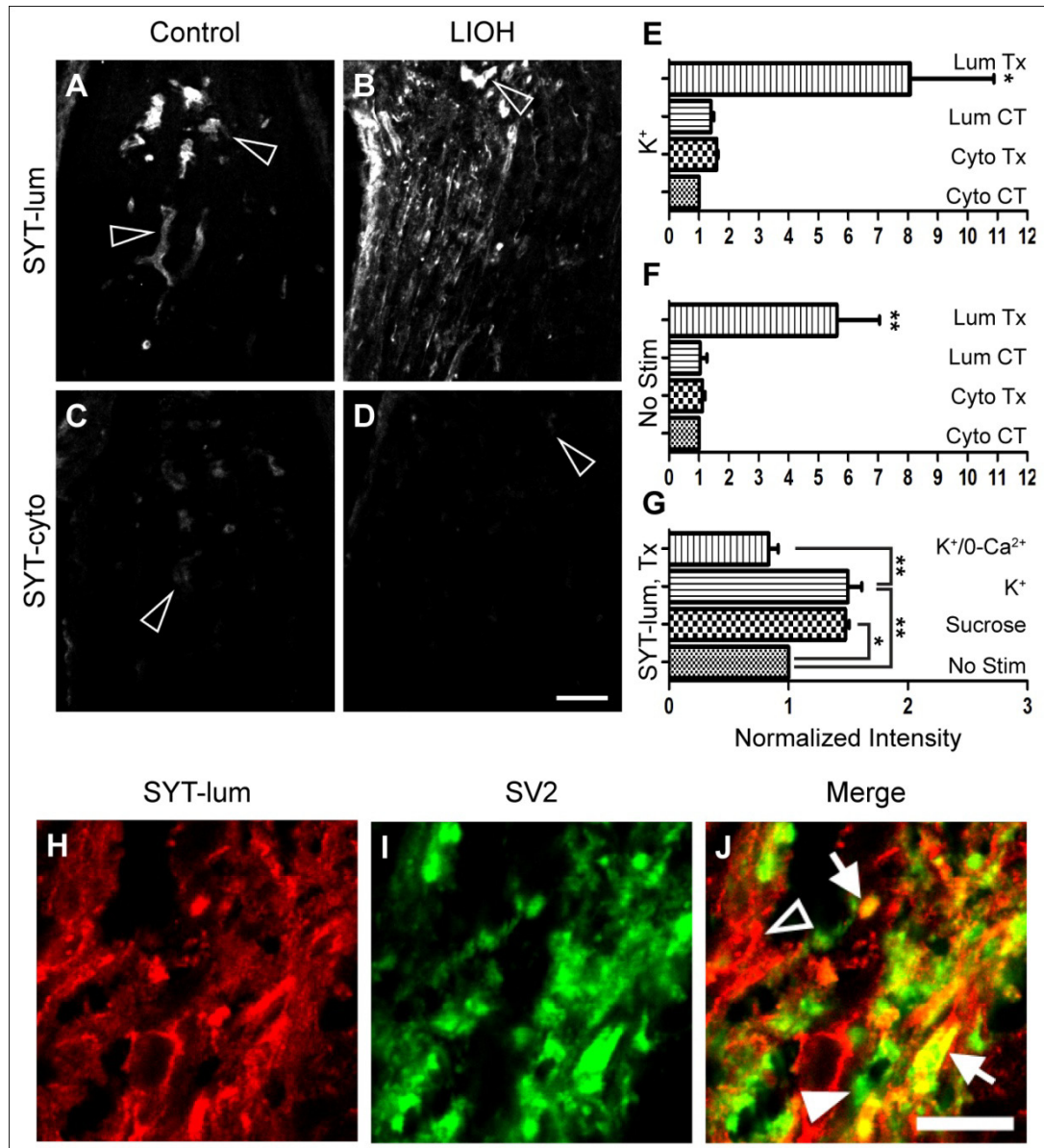


Figure 4-6. Living labeling with synaptotagmin luminal domain antibodies demonstrates exocytosis of ectopic vesicles

Freshly dissected eye cups were incubated with antibodies against either the luminal domain of synaptotagmin (SYT-lum), or the cytoplasmic domain (SYT-cyto) as a negative control. (A-D) A representative experiment in which tissues were stimulated with high K⁺ prior to labeling. SYT-cyto (C, D) produces no appreciable signal other than non-specific blood vessel staining (open arrowheads). SYT-lum labeling is very weak in the control condition (A), but increases markedly after LIOH (B), which appears clearly distinguishable from the non-specific staining (open arrowheads). Quantification of K⁺-stimulated (E) and unstimulated (F) experiments demonstrates significant upregulation of SYT-lum labeling at the LIOH ONHs compared to untreated controls. The analysis in (G) compares different SYT-lum labeling conditions for LIOH samples. Either high K⁺ or

hypertonic sucrose stimulation leads to more substantial SYT-lum staining than normal aCSF alone. Eliminating Ca^{2+} from the high K^{+} solution abolishes the difference between stimulated and unstimulated conditions. **(H-J)** Co-labeling of SYT-lum **(H)** and SV2 **(I)** within a region of the ONH. The LIOH sample from an unstimulated experiment is shown here. Arrows in **(J)** point to co-localized immunoreactivities of SYT-lum and SV2. Solid and open arrowheads denote SYT-lum⁻ SV2⁺ and SYT-lum⁺ SV2⁻ regions, respectively. Scale bar: 50 μm . n = 3 experiments for **(E)**, 4 experiments for **(F)**, and 3 experiments for **(G)**. * $p < 0.05$; ** $p < 0.01$. Prior to the experiments used for quantification, pilot studies with high K^{+} aCSF were conducted 6 times with similar results.

Glutamate Can Be Released from the Glaucomatous ONH

Having established that ectopic vesicles contain glutamate and can undergo exocytosis *in vivo* and *ex vivo*, I next investigated whether glutamate can be released from the LIOH ONH. As shown in Fig. 4-3, immunoreactive “hotspots” of glutamate often appear to extend into the surrounding areas of SV protein labeling. However, using indirect immuno-detection at the light microscopy level, it is difficult to ascertain whether glutamate has been released from the vesicles into the extracellular space. To detect and quantify glutamate release, I used an enzymatic assay in which endogenous glutamate released from living tissues is visualized with fluorescence imaging. L-glutamic dehydrogenase (GDH) supplied in the assay solution converts glutamate to α -ketoglutarate, concomitantly reducing β -nicotinamide adenine dinucleotide (NAD^{+}) to NADH, which fluoresces under UV excitation^{279,304-306}. This reaction is described by the following equation:



Freshly dissected control or LIOH ONH tissue was incubated with an enzymatic assay solution containing GDH and NAD^{+} . Stimulation was introduced by either high K^{+}

or hypertonic sucrose, and the release of glutamate was monitored by detecting NADH accumulation with time-lapse fluorescence imaging. Fig. 4-7A-B shows a pseudo-colored representative experiment with sucrose. In the control ONH (Fig. 4-7A), application of sucrose produced no detectable change in NADH fluorescence over time. In contrast, sucrose stimulation of the LIOH ONH led to marked enhancement of NADH fluorescence (Fig. 4-7B), which served as an indirect measurement of glutamate release. Quantitative studies were conducted for both K^+ (Fig. 4-7C) and sucrose (Fig. 4-7D) stimulation, and demonstrated significant rise of NADH fluorescence following stimulation in LIOH but not control ONH.

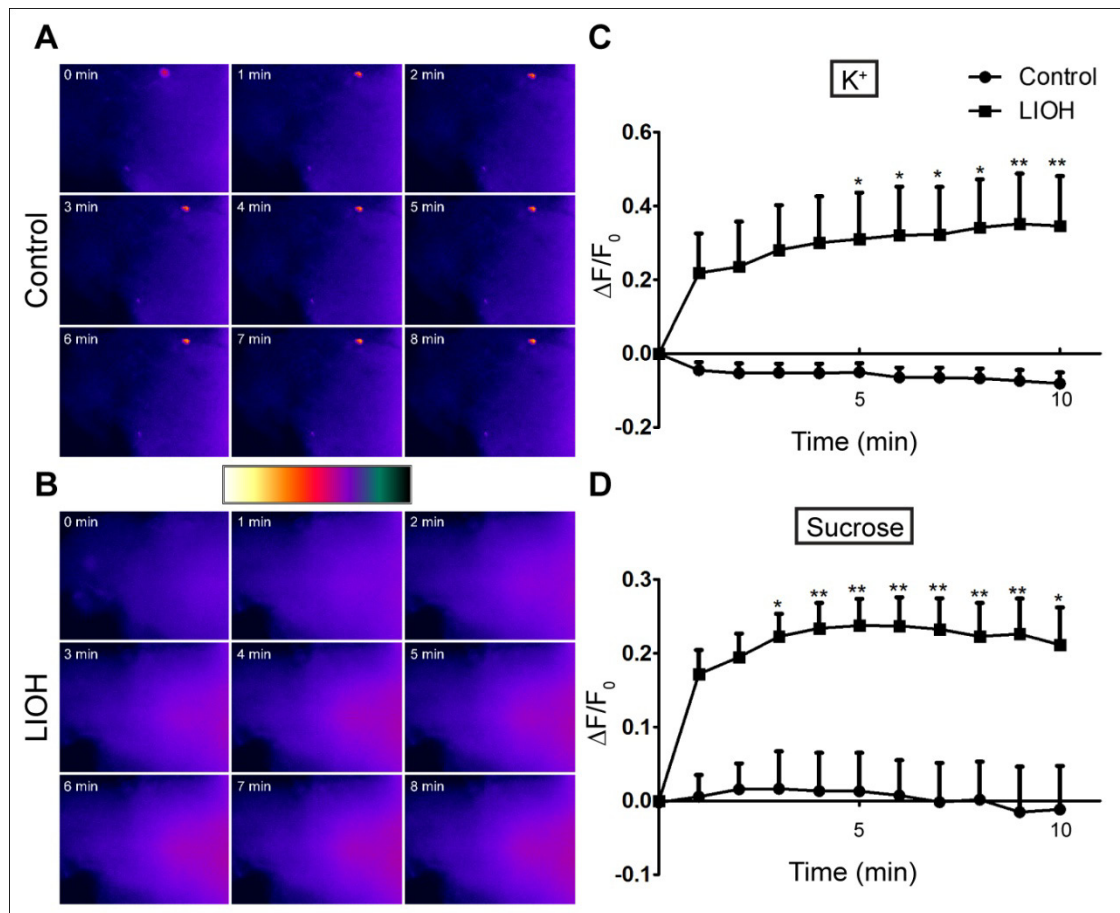


Figure 4-7. NADH assay detects release of glutamate from acutely prepared LIOH ONH tissues

In the presence of glutamate, NAD^+ is converted into NADH, which is fluorescent when excited by UV light. (A, B) A representative time-lapse experiment in which hypertonic sucrose was introduced to provide stimulation. No change in fluorescence level was detected in the control ONH (A). In the LIOH ONH (B), a robust rise in NADH fluorescence resulted from sucrose stimulation, as visualized by the pseudo-colored montage. Images captured at one minute intervals are shown. Quantification of fluorescence intensity shows that both high K^+ (C) and hypertonic sucrose (D) stimulation result in significant accumulation of NADH in the LIOH ONH, suggesting that glutamate has been released from the tissue. $n = 6$ for both control and LIOH in (C). In (D), $n = 9$ for control and 19 for LIOH. * $p < 0.05$; ** $p < 0.01$.

Glutamate Receptor Expression on RGC Axons and Glia at the ONH

So far in my dissertation, I have demonstrated that ectopic glutamate-containing vesicles accumulate at the glaucomatous ONH, and they can undergo exocytosis to release glutamate. However, these findings would lack functional consequences if glutamate receptors are not present at the ONH. I performed immuno-localization studies using glutamate receptor subunit-specific antibodies on cryosections. The results indicate that the alpha-amino-3-hydroxy-5-methyl-4-isoxazolepropionic acid (AMPA) receptor subunit GluR1 and GluR2, and the N-methyl-D-aspartate (NMDA) receptor subunit NR1 are expressed in both control (data not shown) and LIOH (Fig. 4-8). GluR1 was found to co-localize with tubulin (Fig. 4-8C), GFAP (Fig. 4-8F), and CD11b (Fig. 4-8I), suggesting its widespread expression on RGC axons, astrocytes and microglia. The GluR2 subunit exhibited an analogous expression pattern (data not shown). Similarly, punctate NR1 immunoreactivity was also localized to tubulin⁺ axons (Fig. 4-8L) and GFAP⁺ astrocytes (Fig. 4-8O).

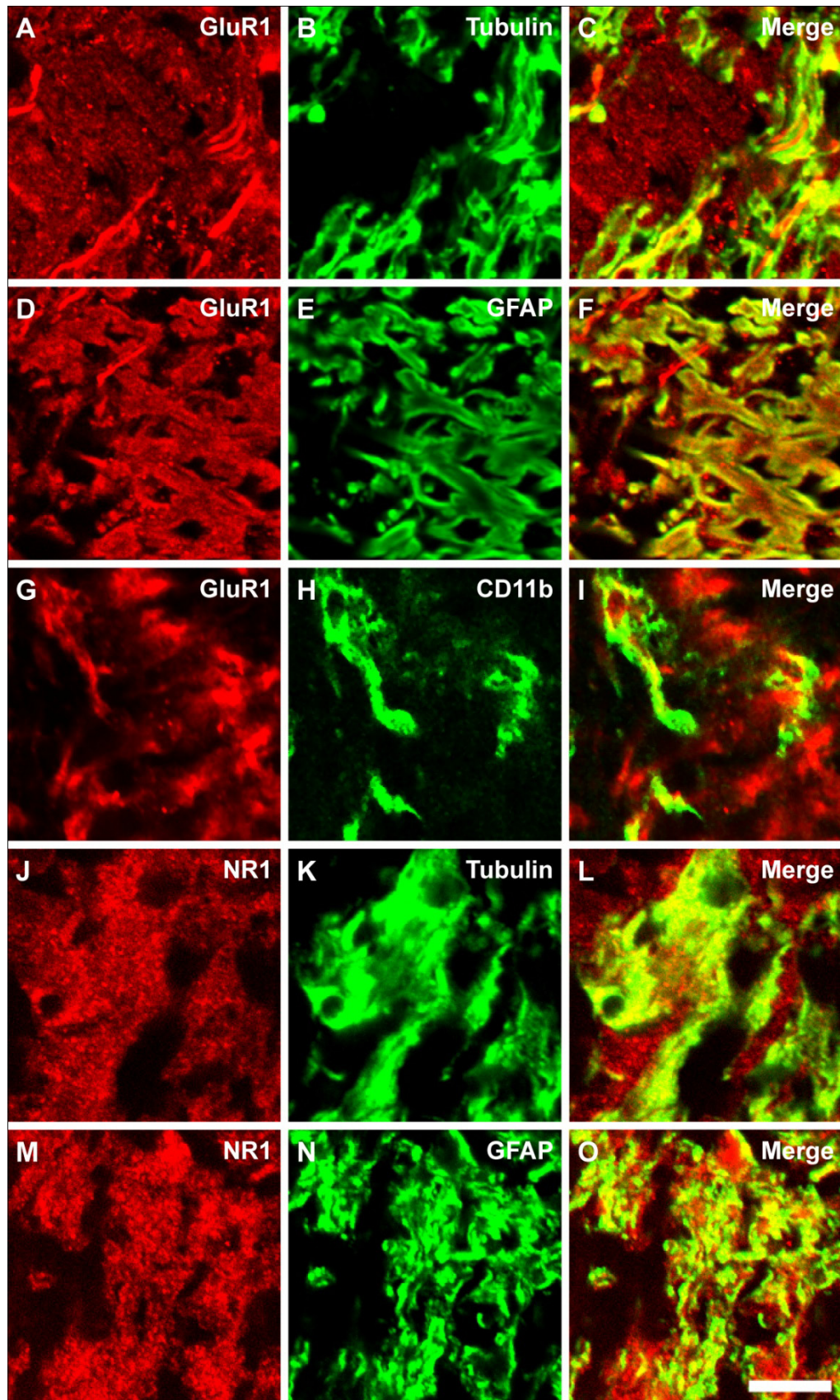


Figure 4-8. Localization of glutamate receptor subunits on RGC axons and glia at the ONH

Images acquired from LIOH day 4 samples are shown. (A-I) GluR1 immunohistochemistry. Co-labeling studies of GluR1 (A, D, G) with tubulin (B), GFAP (E), and CD11b (H) demonstrate that GluR1 is expressed on axons (C), astrocytes (F), and microglia (I). (J-O) NR1 immunohistochemistry. NR1 (J, M) was co-immunostained with tubulin (K) or GFAP (N). Punctate labeling is found on both axons (L) and astrocytes (O). Scale bar: 50 μ m.

Functional Demonstration of Glutamate Receptor Activity Upregulation at the Glaucomatous ONH

Although subunit localization studies suggest that ionotropic glutamate receptors are expressed on RGC axons and glia of the ONH, their functionality cannot be directly demonstrated by immunolabeling. I next used Agmatine (1-amino-4-guanidobutane; AGB) as a reporter for channel permeation to provide functional evidence of ionotropic glutamate receptor activation in LIOH. The guanidinium analogue AGB is a channel-permeant organic cation. It has been established as a useful tool to functionally map ionotropic glutamate receptors in developing and adult retinas of several mammalian species³⁰⁷⁻³²⁰. Pioneering studies by Robert Marc's group demonstrate that activating ionotropic glutamate receptors in the presence of AGB results in AGB permeation into retinal neurons, and the intracellular AGB can be trapped by glutaraldehyde fixation and detected with specific antibodies^{313,319}. Most of the retinal mapping studies employing AGB have been performed *in vitro* with exogenously supplied glutamate or agonists. I modified these protocols to develop a method of studying endogenous glutamate receptor activation at the ONH *in vivo*. AGB was injected into the subconjunctival space of anesthetized control or LIOH mice, in order for the reagent to gain access into the ONH.

The tissues were subsequently fixed and processed for immunohistochemistry with AGB-specific antibodies. Previous reports³¹⁸⁻³²⁰ and our pilot study (data not shown) confirmed that there was no endogenous AGB signal without exposure to the reagent. Control mice injected with AGB exhibited low levels of punctate labeling at the ONH (Fig. 4-9A, G). AGB signal was notably upregulated in LIOH samples (Fig. 4-9D, J). Quantification of immunoreactivity confirmed that accumulation of AGB at the LIOH ONH was significantly higher than control (Fig. 4-9M), indicating increased level of ionotropic glutamate receptor activity. AGB co-labeled with both tubulin (B, E) and GFAP (H, K), suggesting that the receptors were activated on both RGC axons and astrocytes. These findings are consistent with the expression of glutamate receptor subunits demonstrated previously. The potentiation of receptor activity in LIOH likely reflects the ectopic accumulation and vesicular release of glutamate at the ONH.

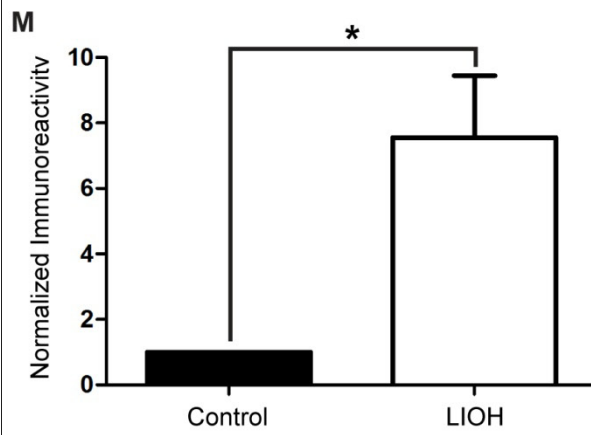
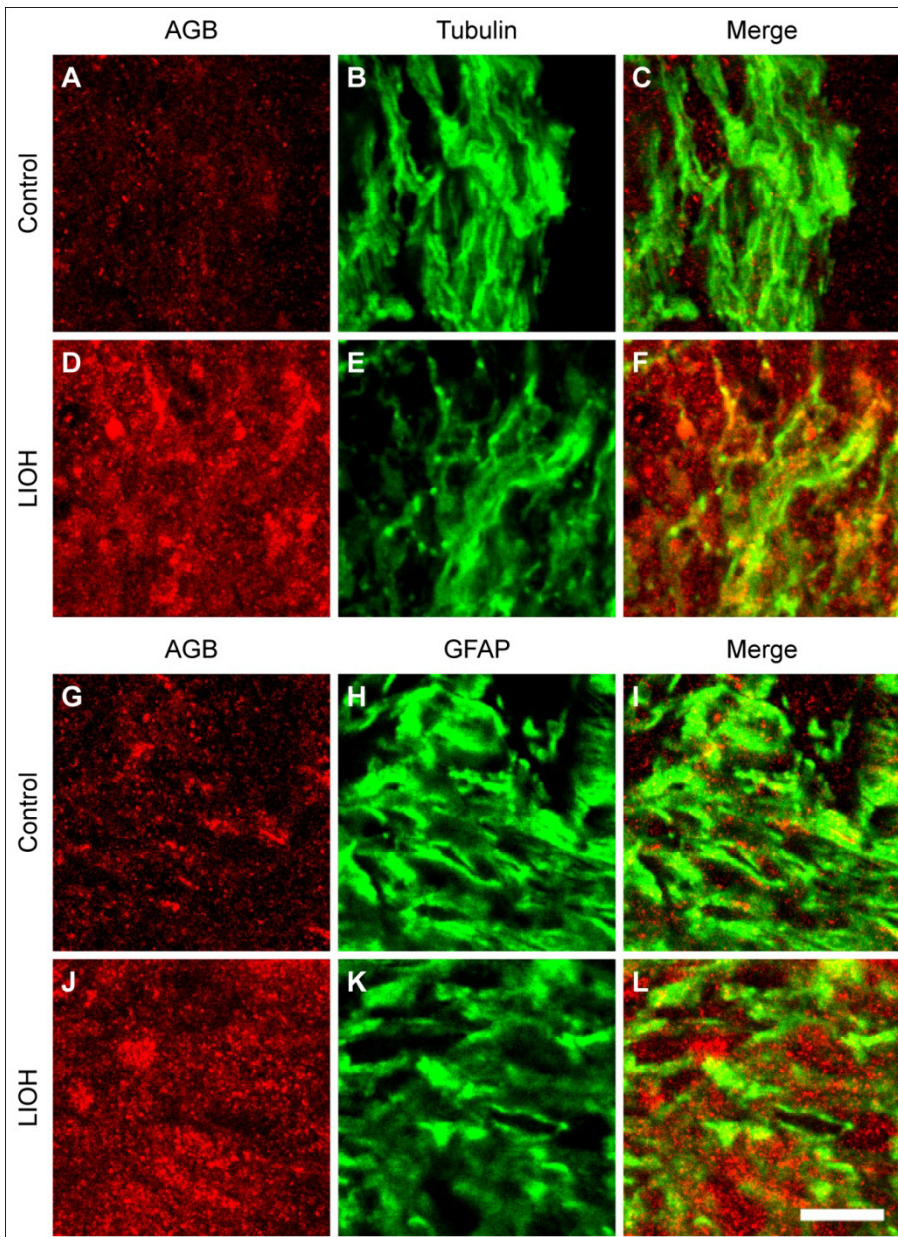


Figure 4-9. Probing ionotropic glutamate receptor activation with the channel-permeant organic cation AGB

After exposure to AGB *in vivo* through subconjunctival injection, control (A, G) and LIOH (D, J) tissues were labeled with antibodies directed against AGB. Co-labeling with tubulin (B, E) or GFAP (H, K) was also performed. AGB immunostaining can be found overlapping with both tubulin (C, F) and GFAP (I, L) at the ONH. (M) Quantitative studies show that AGB immunoreactivity is significantly higher in LIOH compared to control ONHs. Scale bar: 50 μm . n = 4 experiments. * $p < 0.05$.

Pharmacological Blockage of Glutamate Signaling Attenuates Glaucomatous Axon

Degeneration *in vitro* and *in vivo*

The finding of increased glutamate signaling at glaucomatous ONHs makes the effects it exerts on RGC axons of great interest. I developed an organotypic optic nerve explant system to investigate the action of glutamate and other pharmacological agents *in vitro*. Optic nerve explants with retinas attached were cultured at the interface of fluid and air on Millipore inserts. This approach preserves the organization of optic nerve axons and their interaction with surrounding glia, and offers the advantage of a more physiologically relevant environment than isolated neuronal culture. First, I examined the effect of exogenous glutamate application on control optic nerves *in vitro*. Glutamate accelerated axonal degeneration in optic nerve explants in a dose-dependent manner (Fig. 4-10A-D, K). I next explanted LIOH-treated optic nerves, and investigated whether glutamate signaling antagonists influence their degeneration *in vitro*. A cocktail of NBQX and MK-801 was used to block ionotropic AMPA/kainate and NMDA glutamate receptors, respectively. The voltage-gated sodium channel blocker tetrodotoxin (TTX) was also applied to dampen the excitability of axons, which would presumably result in lower glutamate release. Optic nerves cultured 2 days after LIOH (Fig. 4-10H) exhibited

more severe axonal degeneration than untreated control (Fig. 4-10A) *in vitro* (quantified in Fig. 4-10L). NBQX/MK-801 cocktail (Fig. 4-10F, I) and TTX treatment (Fig. 4-10G, J) both significantly attenuated axonal degeneration in LIOH optic nerve explants (Fig. 4-10L). These *in vitro* experiments were performed on multiple days, each with the complete set of treatment groups. Each data point was normalized against the control sample processed at the same time, so that experiments conducted on different days could be compared. To examine the effect of glutamate signaling antagonists *in vivo*, I surgically implanted gelfoam plugs soaked with a NBQX/MK-801/TTX cocktail next to the ONH 1 day after LIOH treatment. Optic nerves were harvested 6 days later, and the axon numbers quantified in cross section. While IOP elevation induced by LIOH was comparable in both treatment conditions (Fig. 4-10M), the surviving axon count was significantly higher in the antagonist cocktail-treated group compared to vehicle-treated animals (Fig. 4-10N). Taken together, these data suggest that glutamate plays a role in optic nerve axon degeneration, and pharmacologically blocking glutamate signaling is protective in experimental glaucoma.

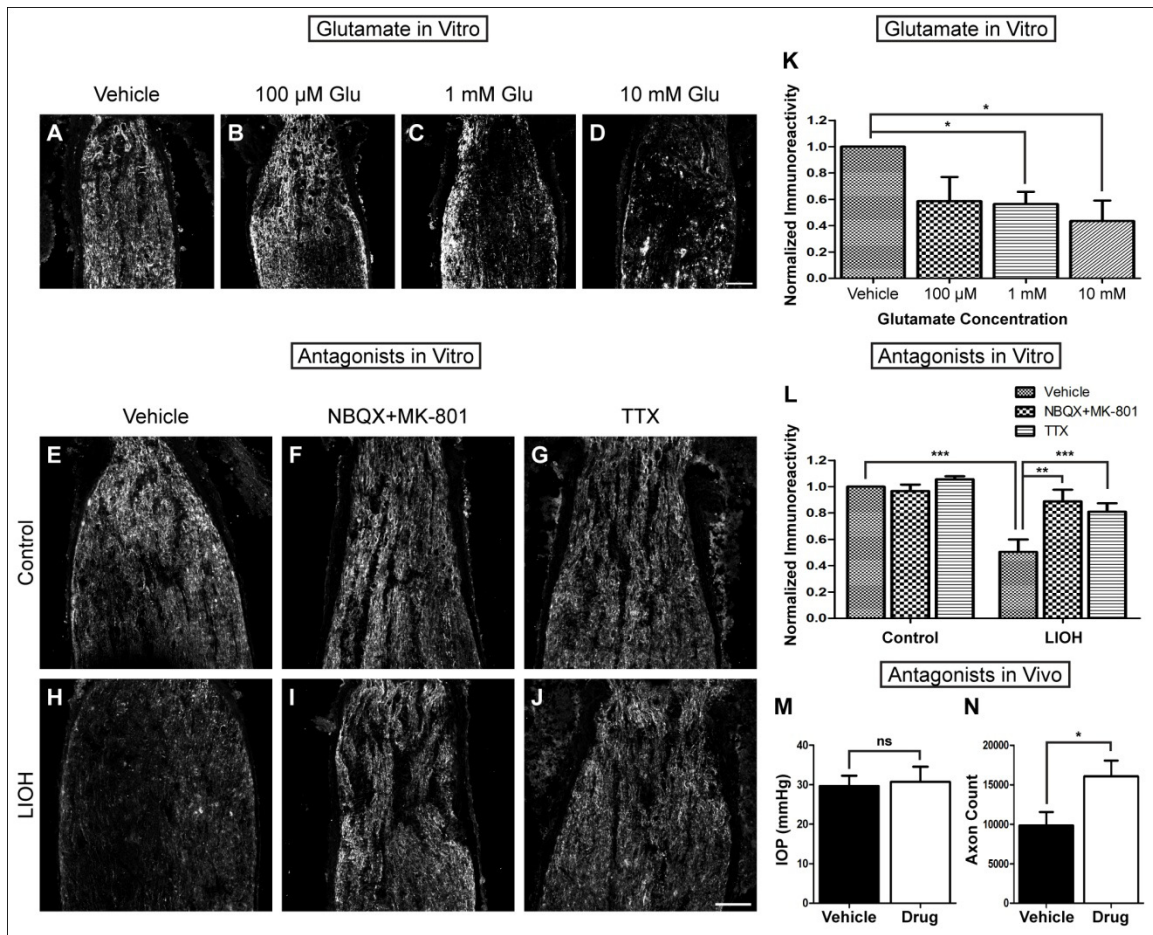


Figure 4-10. Effects of glutamate and glutamate signaling antagonists on optic nerve axonal degeneration *in vitro* and *in vivo*

(A-D) Organotypic optic nerve explant cultures treated with increasing concentrations of glutamate were cryosectioned and analyzed with neurofilament immunohistochemistry. (E-J) Control or LIOH optic nerve explants treated with vehicle, NBQX/MK-801, or TTX. (K) Quantification of the *in vitro* glutamate treatment experiment exemplified in (A-D). Significant axonal degeneration above the vehicle control level is observed for the 1 mM and 10 mM glutamate treatment groups. (L) Quantification of the *in vitro* glutamate antagonists experiment exemplified in (E-J). Exposure to LIOH for 2 days prior to culturing results in more prominent axonal degeneration compared to control explants. Treatment with NBQX/MK-801 or TTX significantly protects against degeneration in LIOH samples. (M, N) Glutamate signaling antagonist cocktail or vehicle was locally delivered to the ONH of animals treated with LIOH. (M) confirms that IOP elevation in both groups was comparable. (N) The antagonist-treated group has significantly higher number of survival axons in the optic nerve compared to vehicle control. Scale bar: 50 μ m. n = 5 experiments for (K), 6 experiments for (L), and 11 animals for the study analyzed in (M) and (N). * $p < 0.05$; ** $p < 0.01$; *** $p < 0.001$.

Generation of Albino Mice Carrying Floxed Alleles of VGLUT2 and NR1

The data so far support a model in which ectopic accumulation of SV protein-containing vesicles at the glaucomatous ONH leads to an excess of exocytotic glutamate release, contributing to the degeneration of RGC axons. Although the pharmacological antagonism experiments provide an important line of evidence demonstrating the involvement of glutamate, diffusible drug application is limited in spatial specificity, and the approach does not address which cell type is the primary target of glutamate action. Glutamate could directly bind to its receptors on RGC axons, or indirectly participate in axonal degeneration through glial activation. To provide further spatial and cell-type specificity, I studied the LIOH model with transgenic mice in which key components of the proposed pathophysiological pathway were selectively deleted in RGCs. In a *Cre/loxP* recombination system, the gene of interest is flanked by two *loxP* sites (floxed), and the introduction of Cre recombinase results in conditional excision of the floxed gene in a spatially and temporally controlled manner³²¹. Two transgenic lines were used in this particular experiment: one that carries floxed *Slc17a6* gene which encodes VGLUT2²⁷⁸ and one that carries floxed *NMDA receptor 1 (NR1)* gene²⁷⁷. Cre recombinase was delivered by intravitreal injection of recombinant adeno-associated virus (rAAV) that transduces RGC with high efficiency and specificity.

The floxed *Slc17a6* (henceforth referred to as VGLUT2-f) and floxed *NMDAR1* (referred to as NR1-f) mice were maintained in the C57BL/6 background. To date, we have not obtained consistent and reproducible results with conducting the LIOH model in

C57BL/6 mice. IOP elevation and optic nerve degeneration were observed in some experimental animals, but results were often confounded by considerable anterior segment abnormality and ocular inflammation (data not shown). One major advantage of using albino mice in LIOH is the ease of visualizing ocular vasculature, allowing better laser targeting and minimal secondary damage. To circumvent the problem of pigmentation in LIOH operation, I made the floxed mouse lines albino by crossing them to a coisogenic strain that differs from C57BL/6 at one single locus. The B6(Cg)-*Tyr*^{c-2J}/J (B6-albino) mice, available from the Jackson Laboratory, are albino C57BL/6J mice homozygous for a *Tyr*^{c-2J} mutation in the tyrosinase gene. Crossing the pigmented floxed mice to B6-albino mice for two generations produced albino VGLUT2-f (*Slc17a6*^{loxP/loxP}; *Tyr*^{c-2J/c-2J}) and NR-f (*NR1*^{loxP/loxP}; *Tyr*^{c-2J/c-2J}) mice, which were then used in subsequent LIOH studies.

Intravitreal Injection of Recombinant AAV Vectors

Recombinant AAV-2 vectors delivered via intravitreal injection have been shown to transduce RGCs with high efficiency and specificity^{82,280,322-326}. I used an AAV vector carrying the Cre recombinase (AAV-Cre) to conditionally delete floxed genes encoding VGLUT2 or NR1, and one that carries GFP (AAV-GFP) as control. The vectors were generously provided by Dr. Zhigang He, and have been described previously²⁸⁰. The reporter line Rosa26-EYFP Ai3³²⁷ that produces EYFP in cells which co-express Cre was used to confirm Cre recombination of *loxP*-flanked sequences. An example of flat-mounted Rosa26-EYFP retina three weeks after intravitreal injection of AAV-Cre is

shown in Supplemental Fig. 4-17A-C, using NeuN as a marker for RGCs⁶¹. The percentage of NeuN⁺ cells that co-localize with EYFP fluorescence was about ~90% of the total RGCs that were transduced with AAV-Cre. This finding agrees with Park et al. who reported more than 90% transduction efficiency two weeks following intravitreal injection²⁸⁰. In retinal cross sections, robust EYFP signal in the GCL, NFL, and IPL was observed (Fig. 4-17D). Although a few bipolar and amacrine cells appeared to be labeled, RGCs remained the primary cell type transduced in the retina (Fig. 4-17F). In the optic nerve, EYFP labeling was robust and highly specific (Fig. 4-17G). RGC axons were the only cell type transduced (Fig. 4-17I).

VGLUT2 Deletion in RGCs Diminishes Glutamate Accumulation at the Glaucomatous ONH

Albino VGLUT2-f mice were intravitreally injected with AAV-Cre in one eye and AAV-GFP in the fellow eye. LIOH was performed three weeks after injection. Similar to the CD-1 mice, AAV-GFP-injected B6-albino mice also exhibited dramatic accumulation of VGLUT2 immunoreactivity at the LIOH ONH (Fig. 4-11A), which co-localized with the axon marker tubulin (Fig. 4-11C). AAV-Cre injection resulted in dramatic knockdown of VGLUT2 accumulation. In some cases, VGLUT2 immunoreactivity at the ONH was nearly abrogated (Fig. 4-11D).

Accumulation of glutamate immunoreactivity was observed in AAV-GFP-injected VGLUT2-f mouse ONH after LIOH, consistent with the findings in CD-1 mice (Fig. 4-11G). The glutamate labeling overlapped that of SV2 extensively (Fig. 4-11I).

Higher magnification (Fig. 4-11I, inset) revealed that glutamate immunoreactivity was heterogeneous and appeared in intensely labeled patches, which were closely associated with corresponding SV2 “hotspots.” In AAV-Cre-injected ONH, glutamate labeling after LIOH was markedly diminished (Fig. 11J). While SV2 accumulation remained (Fig. 4-11K), glutamate staining was weak and diffuse, and did not correlate with SV2 “hotspots” (Fig. 4-11L, inset). These observations confirm that the conditional gene deletion was indeed specific for VGLUT2. Ectopic vesicles were still present at the ONH, although most of them became devoid of VGLUT2 after AAV-Cre transduction, and consequently lost the ability to accumulate glutamate.

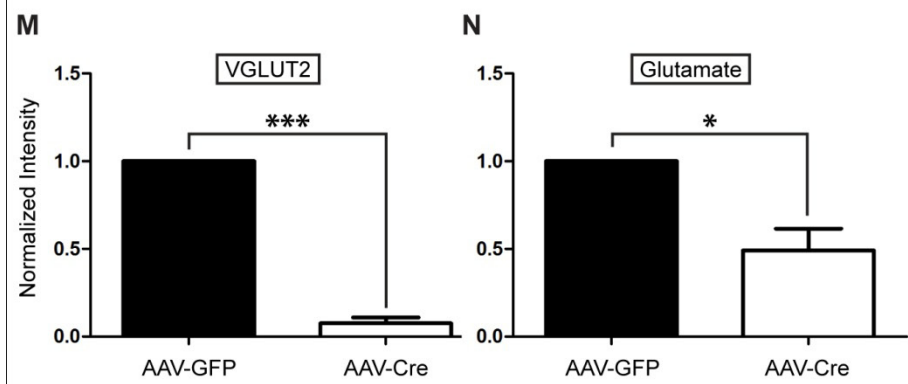
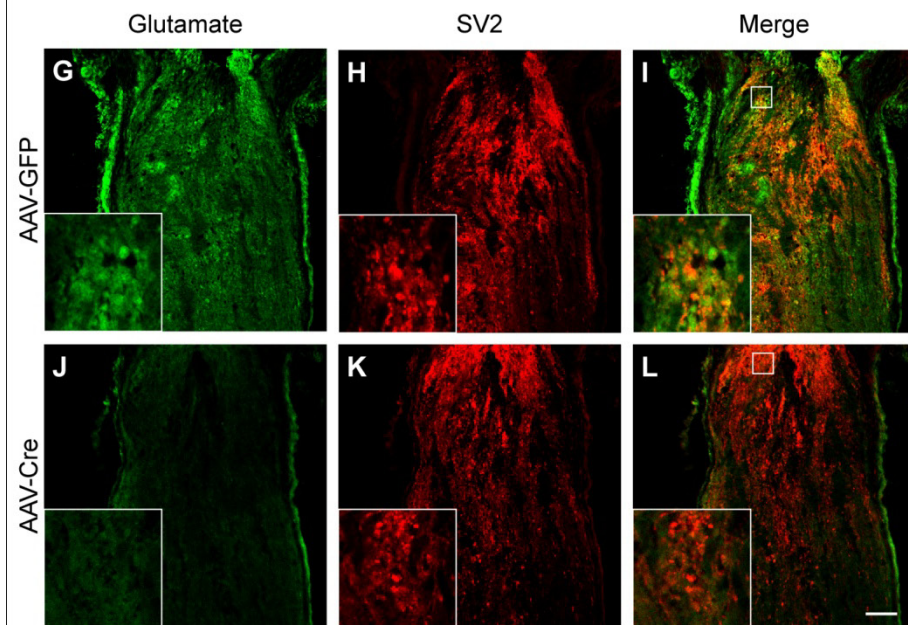
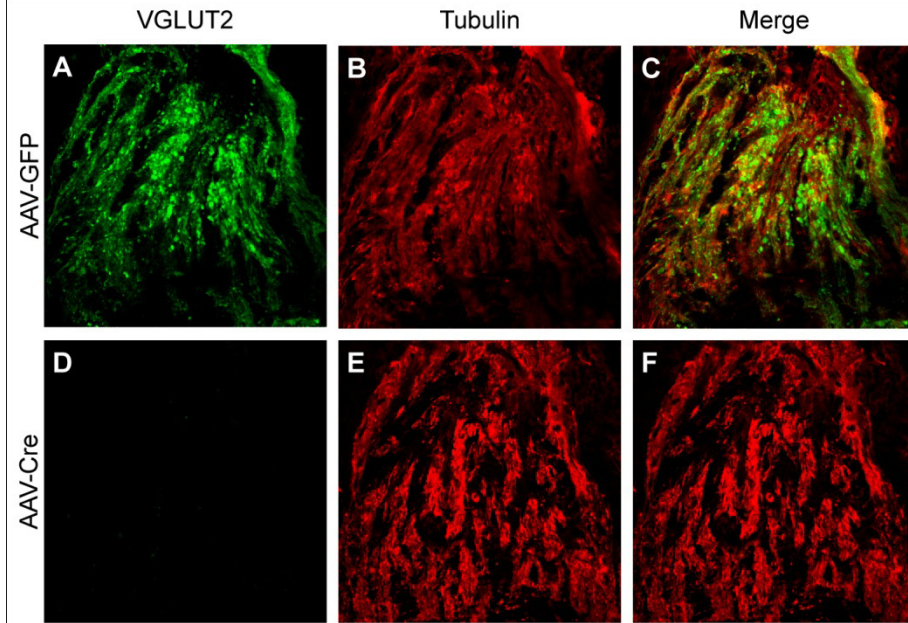


Figure 4-11. Effective VGLUT2 knockdown and reduction of ONH glutamate by AAV-Cre in VGLUT2-f mice

The accumulation of VGLUT2 after LIOH is observed in AAV-GFP-injected VGLUT2-f mouse ONH (A), but becomes nearly abolished in the AAV-Cre-injected eye (D). In this case, although some small puncta of VGLUT2 immunoreactivity could be discerned by visual inspection under epifluorescence, with image acquisition parameters matching those of the AAV-GFP condition, the remaining label is below the level of detection. Tubulin staining (B-C, E-F) confirms the presence of RGC axons. SV2 labeling after LIOH is not altered in AAV-Cre (K) compared to AAV-GFP (H), but glutamate immunoreactivity becomes much reduced in the AAV-Cre condition (compare J with G). Glutamate and SV2 "hotspot" often co-distribute in the AAV-GFP control (G-I, insets taken from the boxed region in I). In AAV-Cre, glutamate labeling is more diffuse and no longer mirrors SV2 "hotspots" (J-L, insets taken from the boxed region in L). Samples were analyzed 3 days after LIOH. The reduction in VGLUT2 (M) and glutamate (N) was quantified and found to be significant. VGLUT2 and tubulin were in fact labeled with cy3- and cy5- conjugated secondary antibodies, so GFP fluorescence in the AAV-GFP control condition did not contribute to the VGLUT2 signal. The images were colorized in green and red for consistency of presentation and ease of visualizing co-localization. Scale bar: 50 μm . $n = 4$ for VGLUT2 and 5 for glutamate. $*p < 0.05$; $***p < 0.001$.

VGLUT2 Deletion in RGCs Attenuates Glutamate Receptor Activity at the Glaucomatous ONH

Ionotropic glutamate receptor activation was probed using AGB as demonstrated in Fig. 4-9. In the AAV-GFP condition, LIOH-treated B6-albino VGLUT2-f mice displayed strong labeling at the ONH (Fig. 4-12A), which was present in both axons and glia (Fig. 4-12C). After AAV-Cre injection, the overall level of receptor activation was attenuated (Fig. 4-12D), likely a consequence of the diminution of glutamate accumulation due to VGLUT2 knockdown. AGB immunoreactivity over RGC axons was quantified and found to be significantly reduced by 70% in AAV-Cre (Fig. 4-12M).

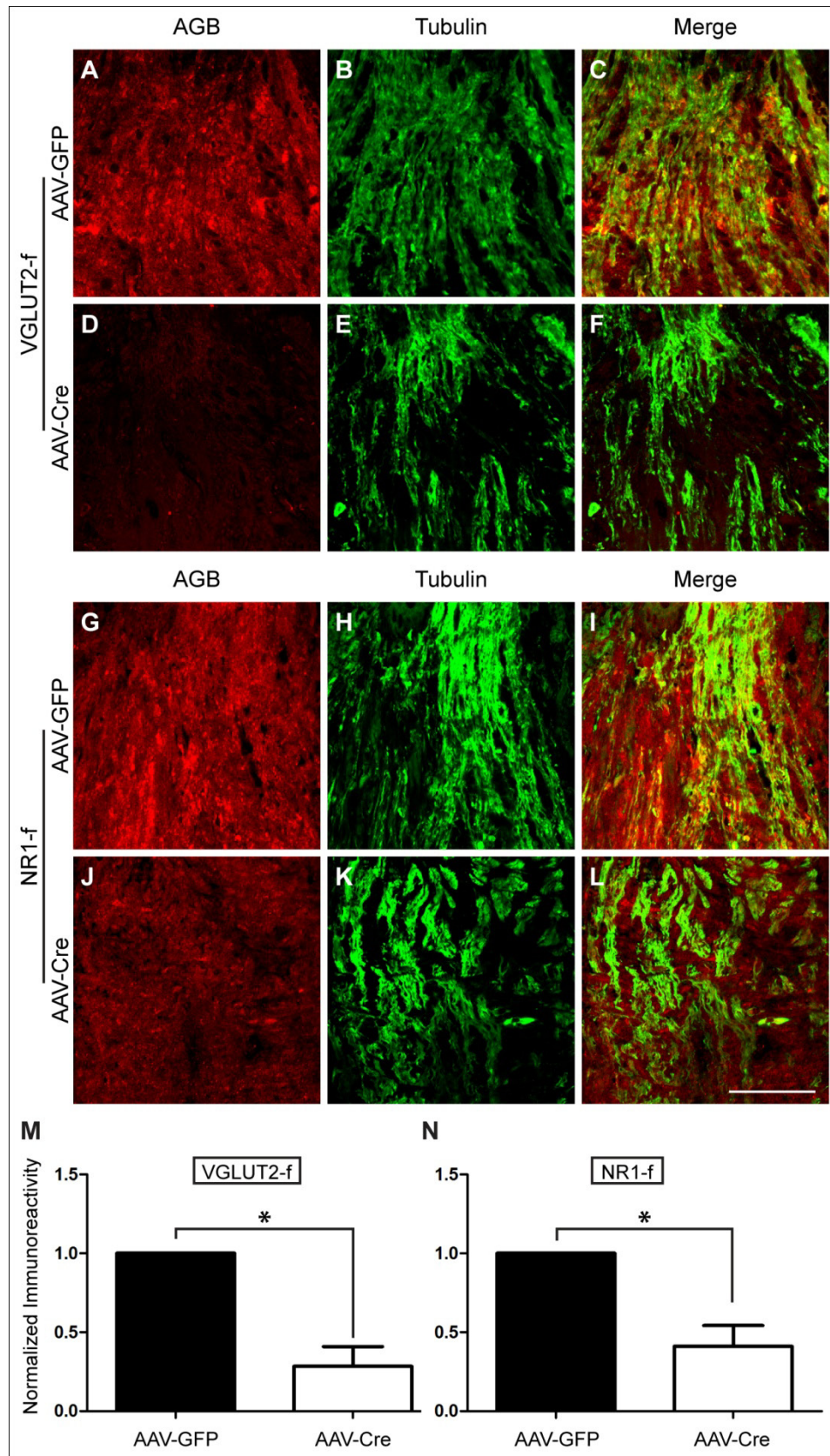


Figure 4-12. AGB assay demonstrates reduced glutamate receptor activity by AAV-Cre injection in both VGLUT-f and NR1-f mice

AGB was injected subconjunctivally 3 days after LIOH, as described earlier. In both floxed mouse lines, LIOH results in strong AGB labeling (**A, G**) at the ONH. Tubulin staining (**B, H**) shows that part of the AGB signal is localized to axons (**C, I**), while additional glial labeling is also present. In VGLUT2-f mice, AAV-Cre injection markedly reduces the overall level of AGB staining (**D-F**). In NR1-f mice, AGB staining (**J**) is diminished in tubulin⁺ axons, while the intensity of glial signal remains comparable to the AAV-GFP control (**L**). AGB immunoreactivity over RGC axons in VGLUT2-f (**M**) and NR1-f (**N**) mice was quantified. Significant reduction by AAV-Cre compared to AAV-GFP is found in both experiments. Scale bar: 50 μ m. n = 3 for VGLUT2-f and 4 for NR1-f. * $p < 0.05$.

NR1 Deletion in RGCs Reduces Glutamate Signaling in Axons at the Glaucomatous ONH

The conditional deletion of NR1 by AAV-Cre in floxed mice was not analyzed by immunohistochemistry for NR1, because at the time of this experiment, the NR1 antibodies used previously were discontinued from the manufacturer. By the time this dissertation was prepared, I had analyzed several alternative antibodies but did not identify one that was satisfactorily specific for NR1. Instead, I used the functional AGB activation assay as an indirect measure of NR1 knockdown. Since NR1 is an essential subunit of the NMDA receptor³²⁸⁻³²⁹, disruption of NR1 in RGC axons would reduce AGB permeation and accumulation in axons. This prediction was indeed confirmed. In B6-albino NR1-f eyes injected with AAV-GFP, AGB permeation after LIOH resulted in robust labeling of ONH axons and glia (Fig. 4-12G-I). AAV-Cre injection led to a reduction of AGB signal in tubulin⁺ axons by 60% (Fig. 4-12L, N). On the other hand, AGB staining in the neighboring glial cells remained strong. These findings are consistent with the restricted deletion of NR1 in only RGCs. Since the AMPA receptor

subunits GluR1 and GluR2 are also found to be expressed on RGC axons, the remaining AGB signal could be accounted for by AMPA receptors.

Deletion of VGLUT2 or NR1 in RGCs Promotes Axon Survival in Experimental Glaucoma

Axonal survival in AAV-injected VGLUT2-f or NR1-f mice after LIOH was investigated by analyzing PPD-stained optic nerve cross sections. A set of representative images from an experiment in NR1-f mice are shown in Fig. 13A-D. In both mouse lines, IOP elevation was not affected by AAV-GFP versus AAV-Cre treatment (Fig. 4-13E, G). Optic nerve axon counts were comparable in control animals injected with either AAV vector. LIOH in B6-albino mice reduced RGC axon count to ~55-60% of control level in the AAV-GFP injection group after two weeks. AAV-Cre-mediated deletion of either VGLUT2 or NR1 resulted in significant protection of RGC axons (Fig. 13F, H). The total axon count was restored to ~80% of control level. These data indicate that interfering with either vesicular glutamate release or NMDA glutamate receptor activation promotes axonal survival in experimental glaucoma.

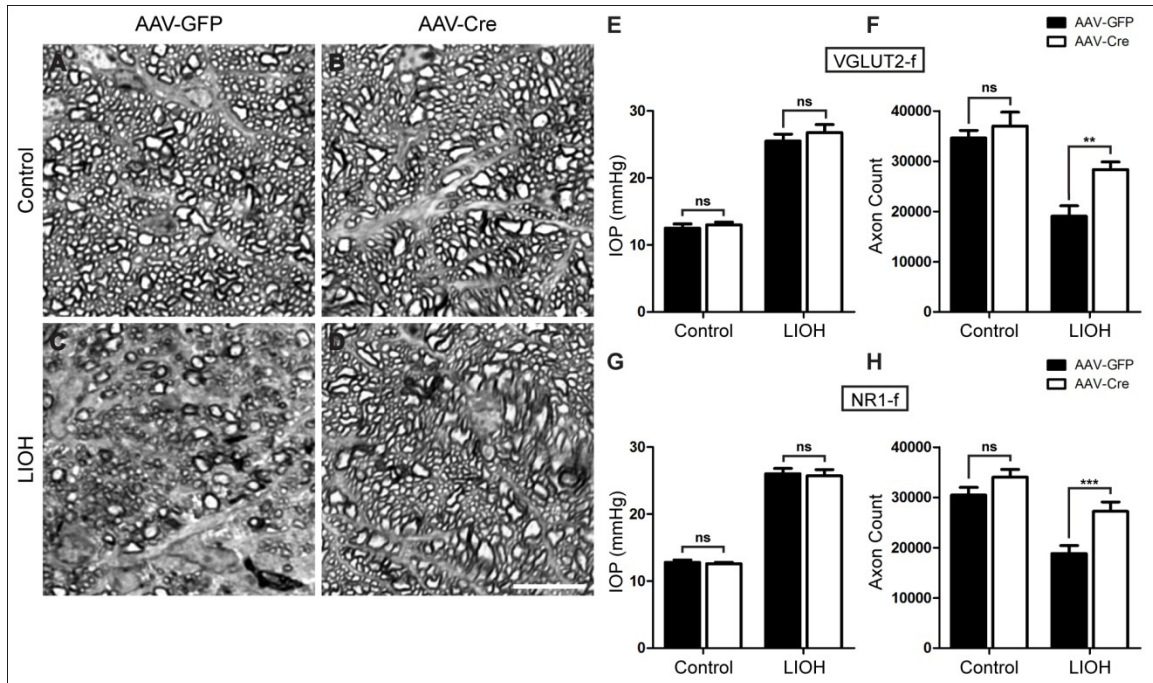


Figure 4-13. AAV-Cre-mediated deletion of VGLUT or NR1 is protective for RGC axons after LIOH

(A-D) Representative PPD-stained optic nerve cross sections from one NR1-f experiment. The control sections are indistinguishable from the AAV-GFP (A) and AAV-Cre (B) conditions. Significant axon drop-out can be observed in the AAV-GFP condition two weeks after LIOH (C). AAV-Cre injection remarkably protects RGC axons against degeneration (D). (E-F) Data from both the VGLUT2-f and NR1-f experiments were quantified. There is no difference of IOP elevation induced by LIOH in AAV-Cre and AAV-GFP (E, G). AAV-Cre injection significantly increases the number of surviving axons two weeks after LIOH in both VGLUT2-f (F) and NR1-f (H) mice. Scale bar: 10 μ m. n = 10 animals for VGLUT-2 and 20 animals for NR1-f. ** $p < 0.01$; *** $p < 0.001$.

Discussion

Ectopic vesicles accumulate in axons at the ONH after induction of experimental glaucoma. These vesicles can undergo exocytosis and lead to local accumulation of glutamate. Glaucomatous ONH exhibits higher activity of glutamate receptors, and disrupting components of this glutamate signaling pathway either pharmacologically or genetically confers significant protection to RGCs against glaucomatous degeneration. Figure 4-14 illustrates a model that I propose based on these findings.

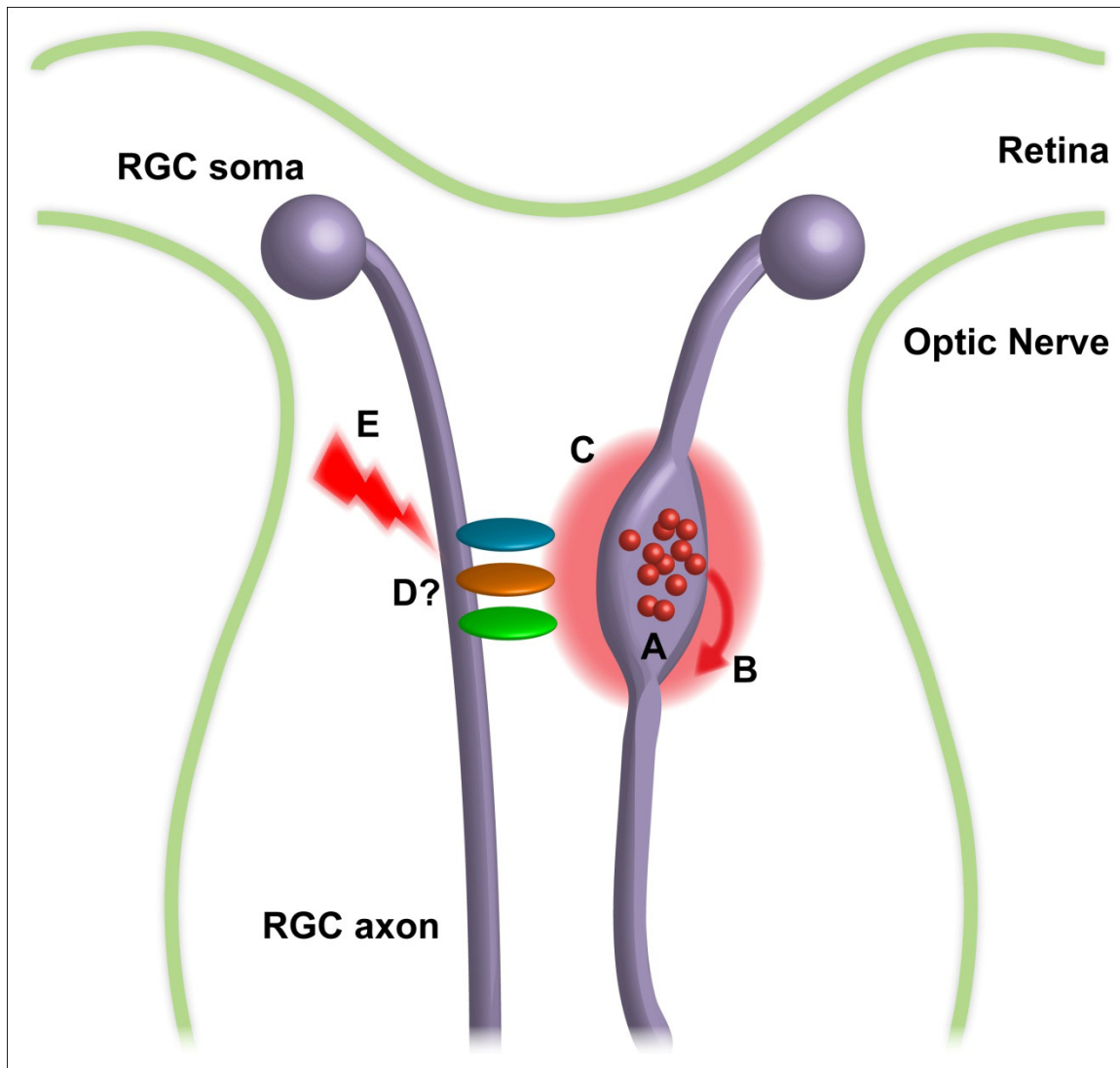


Figure 4-14. Proposed model of localized glutamate excitotoxicity at the glaucomatous ONH

IOP elevation results in ectopic accumulation of SV protein-expressing vesicles that contain glutamate at the ONH (A). These vesicles have the ability to undergo exocytosis (B), potentially leading to local glutamate “hotspots” (C). Glutamate receptors appear to be expressed on RGC axons (D), although the subtype specificity remains to be established. Over-stimulation of glutamate receptors may contribute to excitotoxic damage to neighboring axons (E).

Morphology and Organization of Ectopic Vesicles at the Glaucomatous ONH

Ultrastructural examination of the LIOH-treated ONH reveals dramatic axon swellings and massive accumulation of membrane-bound organelles. This observation agrees with previous findings in rat experimental glaucoma^{28,62}, and bears remarkable resemblance to those documented in plaque-associated dystrophic neurites in AD^{150-151,274}. Among the accumulated organelles are translucent vesicles immunoreactive for the synaptic vesicle marker Synaptophysin. The pleiomorphic nature of these vesicles is worth discussing, because they differ from classical synaptic vesicles which are typically uniform in size (~50 nm) and shape (spherical). Studies of presynaptic assembly in neuronal culture have established that components of the active zone are derived from the trans-Golgi network and transported along developing axons as discrete precursor vesicles to nascent synapses³³⁰⁻³³². These precursors include Piccolo-bassoon Transport Vesicles (PTVs), which carry active zone proteins Piccolo and Bassoon, and Synaptic Vesicle Precursors (SVPs) which contain synaptic vesicle proteins³³³. Pleiomorphic vesicles have indeed been demonstrated in axons at the EM level^{300,332}, which are interpreted to be intermediates in the formation of mature synaptic vesicles. Importantly, they are capable of undergoing exo-endocytosis without the presence of synaptic contacts^{300-301,334-336}. Furthermore, in our LIOH samples, some dense-core vesicles are observed to aggregate with translucent vesicles within axon swellings, which may correspond to PTVs known to be small dense-core vesicle ~80 nm in diameter³³⁰⁻³³¹. This is consistent with our immunohistochemical demonstration that Bassoon co-localizes with ectopic synaptic vesicle markers.

Although some of the putative synaptic vesicle precursors appear scattered among other organelles in our LIOH micrographs, many are densely aggregated and closely apposed to the axolemma. This finding is consistent with our data suggesting that hypertonic sucrose is able to stimulate ectopic vesicle exocytosis and glutamate release. The mechanism by which hypertonic sucrose triggers vesicle fusion remains obscure, but has been proposed to involve mechanical forces imposed by osmotic pressure gradient, causing deformation of the active zone^{302-303,337-338}. Given that the ectopic vesicles are densely packed in large numbers, it is conceivable that mechanical deformation might surmount the energy barrier to membrane fusion. Neurotransmitter release could also be due to reversal of the uptake transporters under depolarizing conditions³³⁹. Therefore, our high K⁺ experiment cannot unequivocally demonstrate that glutamate release from the LIOH ONH is via a vesicular mechanism. The hypertonic sucrose experiments, albeit non-physiological, provide additional evidence in support of this conclusion.

Ectopic Release in Normal Physiology

The release of neurotransmitter-containing vesicles from a non-synaptic region shown in this study may seem surprising at first glance, as it violates the dictum of synaptic vesicle release from highly specialized presynaptic active zones onto postsynaptic densities. However, accumulating evidence suggests that exocytosis can occur at ectopic locations distant from conventional synapses, and many of these release sites are poorly defined at the ultrastructural level³⁴⁰. Ectopic release has been demonstrated at the neuromuscular junction³⁴¹⁻³⁴², retinal bipolar cell terminals³⁴³⁻³⁴⁴,

saccular hair cells³⁴⁵, ciliary ganglion³⁴⁶, and in the cerebellum between climbing fibers and Bergmann glia³⁴⁷⁻³⁴⁹. In addition to nerve terminals, exocytosis of neurotransmitter can occur in white matter tracts. Axons in the corpus callosum and optic nerve release glutamate via vesicular fusion, which is detected by AMPA receptors on NG2⁺ oligodendrocyte precursor cells (OPCs)³⁵⁰⁻³⁵¹. In the olfactory bulb, activity-dependent release of glutamate by olfactory receptor axons evokes Ca²⁺ transients in olfactory ensheathing cells, which is thought to mediate neurovascular coupling³⁵². In many of these examples, clusters of vesicles have been described at the EM level. Although electron dense materials are reported at the axon-OPC junction³⁵⁰, in most cases no distinct presynaptic or postsynaptic specializations similar to the conventional synapses are found. These studies suggest that ectopic release plays a role in normal physiology by mediating synaptic transmission and axon-glia communication, and they pave the way for understanding similar mechanism in pathological situations. Our ultrastructural analysis of the LIOH ONH indicates that although some ectopic vesicles appear to associate with electron dense material along the membrane, the junctions between these accumulation sites and the neighboring cells are not consistently defined. The aforementioned studies strongly argue that morphologically distinct specialization is not a prerequisite for exocytosis, supporting our hypothesis of vesicular glutamate release. Additional evidence includes immunohistochemical demonstration that SNAP-25 is present throughout the RGCs axons, consistent with previous findings for both t-SNARE components, SNAP-25 and syntaxin-1³⁵³⁻³⁵⁴.

Axonal Glutamate Receptors

One major caveat of this study involves the potential lack of specificity of glutamate receptor antibodies. The excitotoxic injury of RGC axons that I propose here depends on the expression of axonal glutamate receptors. Immunohistochemistry suggests that the AMPA receptor subunits GluR1 and GluR2 as well as the essential NMDA receptor subunit NR1 are expressed on RGC axons at the unmyelinated ONH. However, the specificity of these antibodies has not been rigorously demonstrated. The two NR1 antibodies used in this study had subsequently become unavailable. Although one of these antibodies has been widely cited in the literature^{316,355-358}, I did not have an opportunity to directly demonstrate their specificity. Alternative antibodies from other vendors all produced staining on brain sections of *NR1*^{-/-} mouse embryos, raising the concern that antibodies used to generate data in this study may have similar problems with specificity.

Despite the potential concern with specificity in immuno-localization, additional experiments in this study support the presence of axonal glutamate receptors. In my AGB activation experiments, robust glutamate receptor activity is observed in ONH axons, while the subconjunctival delivery method does not produce detectable labeling in the retina. This argues that axonal glutamate receptors can be activated independent of the cell body. However, the data presented here do not differentiate between different routes of AGB entry into the axons. AGB influx could potentially occur via AMPA, kainate or NMDA receptors. Furthermore, *in vitro* pharmacological experiments demonstrate that a cocktail of NBQX and MK-801 attenuates axonal degeneration in optic nerves injured by laser glaucoma. NBQX is a competitive antagonist of both AMPA and kainate receptors³⁵⁹, and MK-801 blocks NMDA receptors³⁶⁰. These results suggest that

glutamate receptors are present on RGC axons and contribute to glaucomatous degeneration; however, the relative contribution of AMPA, kainate and NMDA receptors remains inconclusive.

Previous findings have demonstrated that white matter axons can respond to AMPA or kainate receptor agonists, and excessive stimulation of these receptors can lead to axonal damage^{87,361}. Calcium imaging in spinal cord dorsal column reveals that axons respond to the application of AMPA or kainate receptor agonists with a rise in intra-axonal Ca^{2+} concentration³⁶²⁻³⁶⁴. Injection of AMPA intracerebrally³⁶⁵ or infusion of kainate into the optic nerve³⁶⁶ causes degeneration of axons within white matter tracks. Antagonizing these receptors confers axonal protection in several white matter injury models both *in vitro*^{364,367-370} and *in vivo*³⁷¹⁻³⁷⁵. Using calcium imaging, pharmacological manipulation, and immunohistochemistry, recent studies suggest that spinal cord dorsal column axons express functional GluR4-containing AMPA receptors and GluR5/GluR6-containing kainate receptors. Activation of these receptors using subunit-specific agonists causes increased intra-axonal Ca^{2+} concentration, which is partially dependent on activation of L-type voltage-gated calcium channels and release from intracellular Ca^{2+} stores. In my dissertation, blocking glutamate receptor activation or preventing glutamate uptake/accumulation at the ONH protects against glaucomatous axonal degeneration. It is possible that the excitotoxic action of glutamate demonstrated in this study is mediated, at least in part, by AMPA/kainate receptors.

The expression of NMDA receptor subunits in rodent RGC somas has been well established by mRNA detection³⁷⁶⁻³⁷⁸, immunohistochemistry^{316,355,358}, and electrophysiology³⁷⁹. On the other hand, axonal localization of NMDA receptors has not

been clearly demonstrated. One study reports immuno-detection of NR1 in rat optic nerve³⁸⁰. However, the authors did not confirm the cellular origin of the immunoreactivity in their myelinated optic nerve sample, which is known to contain NR1-positive oligodendrocytes³⁵⁶. Although NMDA receptors are commonly segregated into the somatodendritic compartment instead of axonal compartment in polarized neurons³⁸¹, NR1 expression³⁸²⁻³⁸³ and function³⁸⁴⁻³⁸⁵ on axons has been documented. The presence of NR1 specifically in unmyelinated RGC axons needs to be further corroborated by future studies. In my dissertation, AAV-Cre-mediated deletion of NR1 from RGCs reduces AGB signal in ONH axons, indicating that NMDA receptors account for at least part of the ionotropic glutamate receptor activity. The significant axonal protection conferred by NR1 deletion from RGCs supports a role of NMDA receptors in glaucomatous axon degeneration. However, this particular experiment does not rule out the involvement of RGC somas. An alternative interpretation of the data is that NMDA receptors on RGC somas may be over-stimulated by glutamate released from dying RGCs in the retina, leading to excitotoxic soma injury and subsequent axon damage. It was the objective of my dissertation research to focus on the compartmentalized axonal degeneration mechanisms, while soma injury is not investigated in detail. An important future direction would be thorough time course studies to compare the survival of axons, somas, and dendrites after disrupting glutamate signaling in experimental glaucoma.

Excitotoxic Hotspots

The concept of compartmentalized degeneration of RGC axons versus somas, dendrites and synapses is discussed in Chapter 1. This study presents a mechanism by which localized insult could specifically cause injury to RGC axons. The accumulation of ectopic vesicles induced by LIOH is most prominent at the ONH, and to a much lesser extent in the adjoining retina and myelinated optic nerve regions. The protective effect of VGLUT2 deletion selectively from RGCs provides strong evidence that localized vesicular glutamate release participates in axonal degeneration. Furthermore, a key take-home message emerged from this study is the heterogeneity of pathological responses in glaucoma. Not only is the ectopic vesicle accumulation localized at the ONH with respect to the rest of the eye, it appears heterogeneous within the axon population, and within different segments of the same axon. Consequently, glutamate accumulation and receptor activity also exhibit a distribution in discrete “hotspots.” Since glutamate is traditionally considered a diffusible factor, one criticism of the excitotoxicity theory of glaucoma is that increased vitreal glutamate concentration cannot explain the patchiness of RGC loss in the retina. The pattern of excitotoxic hotspots observed here could lead to focal damage of selective axon bundles at the ONH, thus addressing the sectorial pattern of RGC degeneration^{48,58,138,386}.

The excitotoxic mechanism proposed here differs considerably from the traditional idea discussed in Chapter 1. Previous efforts were focused on investigating vitreal glutamate, which is thought to be released by dying RGCs and cause secondary degeneration of neighboring cells. Although the initial finding of raised vitreal glutamate concentration was not replicated, it does not rule out glutamate involvement in a more localized fashion. The neuroprotective effect of NMDA receptor blockers in animal

models support the relevance this idea^{21,23-24,387}. We demonstrate in the present study that glutamate is released via a vesicular mechanism from ONH axons as opposed to the retina, and the accumulation of glutamate is heterogeneous instead of uniform. This phenomenon occurs relatively early in the disease process (~2 days after LIOH), before significant soma loss sets in (between week 1 and 2 as shown in Chapter 2). Therefore, blocking glutamate release and/or signaling at this point could still rescue a considerable proportion of RGCs, as demonstrated by our AAV experiments.

It is also possible that glutamate plays a role within the retina in parallel to the axonal degeneration program, even if its vitreal concentration doesn't reach detectable level. Some recent studies provide evidence that intra-retinal glutamate is elevated²⁵⁻²⁷ in rodent glaucoma. In addition, glutamate clearance mechanism may be compromised in glaucomatous retina, contributing to extracellular accumulation of the excitotoxin³⁸⁸. How intra-retinal glutamate affects the survival and function of different RGC compartments awaits further elucidation.

Cause of Ectopic Vesicle Accumulation

The nature of the factors that cause ectopic vesicle accumulation remains unclear. One scenario is that mechanical forces secondary to IOP elevation directly obstruct axonal transport. The second scenario may involve glial activation, which then signals the stalling of transport vesicles in the axon via molecular messengers. Anterograde transport of vesicular cargos on the axonal microtubule is mediated by the kinesin family of motor proteins³³³. Nitric oxide derived from microglia, inflammatory cytokine tumor necrosis

factor- α , and pathogenic polyglutamine-expanded androgen receptor have all been shown to stimulate phosphorylation of c-Jun N-terminal kinase (JNK), causing dissociation of kinesin from microtubules, and unloading of synaptic vesicle precursors³⁸⁹⁻³⁹¹. Kinesin-1 defect in transgenic mice is sufficient to induce axonal pathologies similar to many neurodegenerative diseases³⁹². Interestingly, my preliminary data indicate that phosphorylated JNK is upregulated at the ONH after LIOH, and co-localizes with ectopic vesicles. Whether this observation has a causal relationship to the vesicular accumulation deserves to be followed up in future studies.

Supplemental Figures

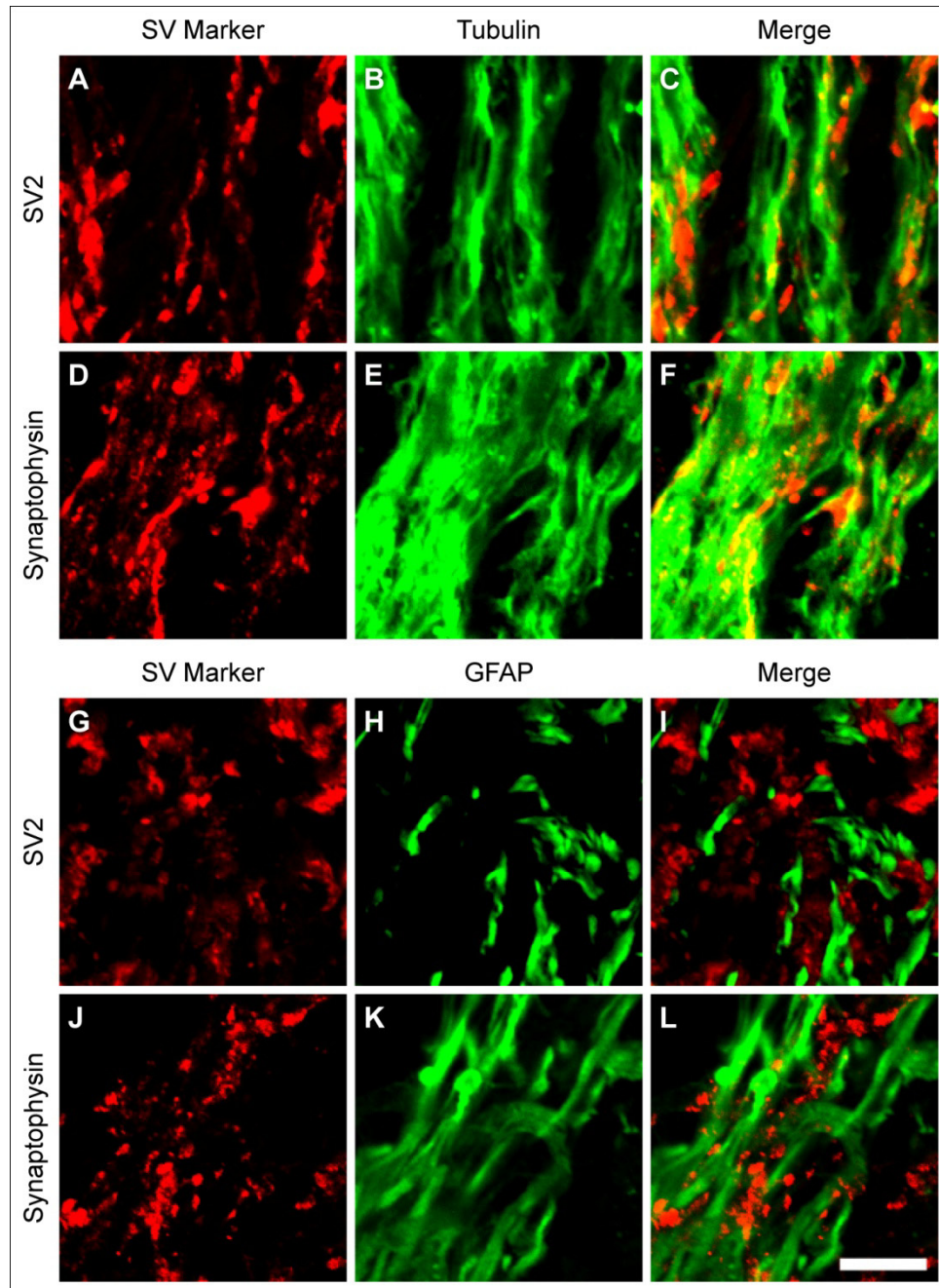


Figure 4-15. Ectopic synaptic vesicle proteins SV2 and Synaptophysin are present in axons but not astrocytes

Samples collected 4 days after LIOH were immunostained for SV2 (**A, G**) and Synaptophysin (**D, J**), with co-labeling of tubulin β -III (**B, E**) or GFAP (**H, K**). Both SV2 (**C, I**) and Synaptophysin (**F, L**) co-localize with the axonal marker tubulin but not the astrocytic marker GFAP. Scale bar: 50 μ m.

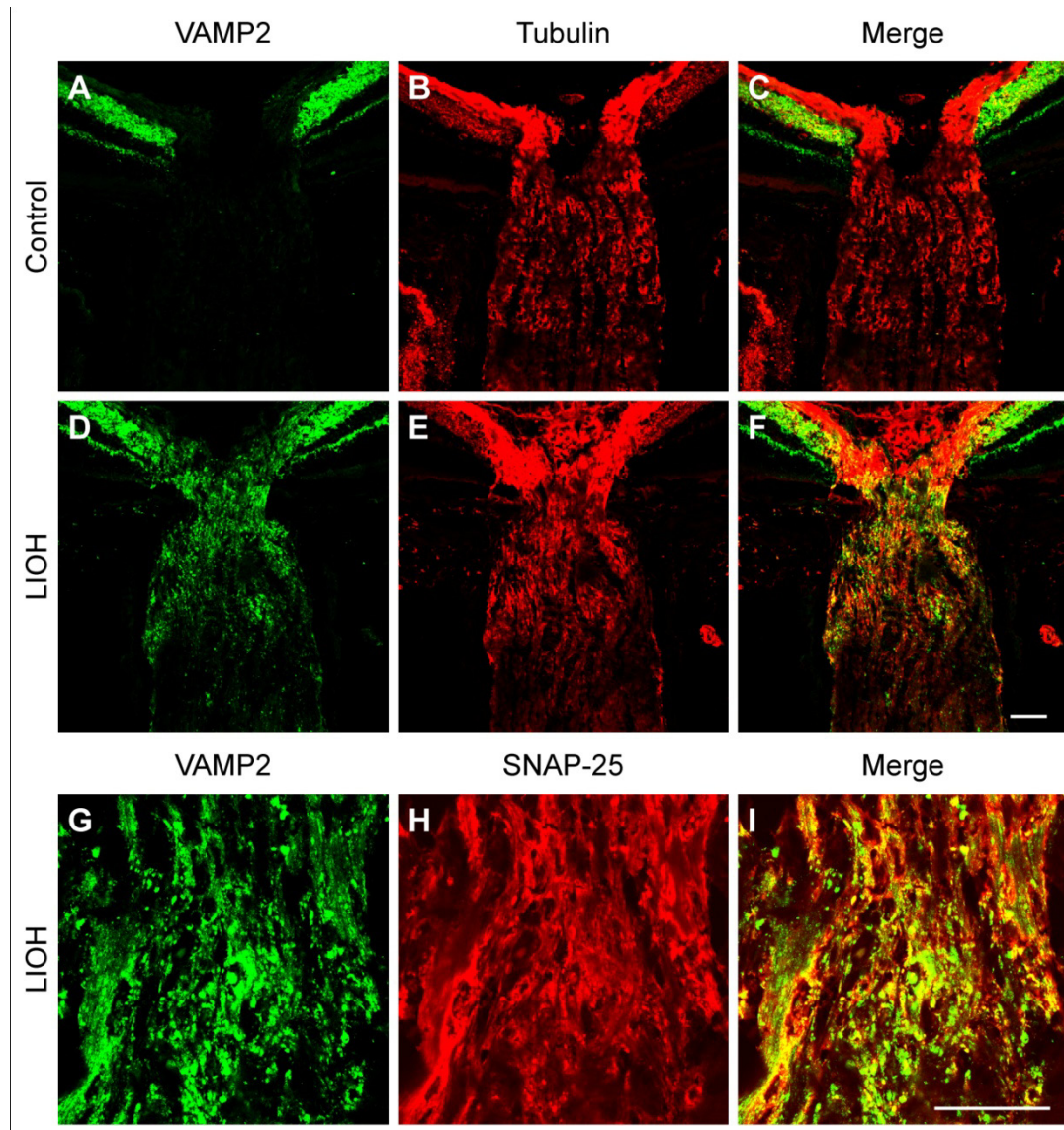


Figure 4-16. VAMP2 accumulation at the LIOH ONH and co-localization with SNAP-25

VAMP2 is absent in the control optic nerve (A), but becomes dramatically accumulated at the ONH 4 days after LIOH (D), similar to other synaptic vesicle proteins. Tubulin (B, E) staining demonstrates that ectopic VAMP2 accumulation is within RGC axons (F). Co-labeling of VAMP2 (G) and SNAP-25 (H) in LIOH samples reveals extensive overlap of immunoreactivity (I). Scale bar: 50 μ m.

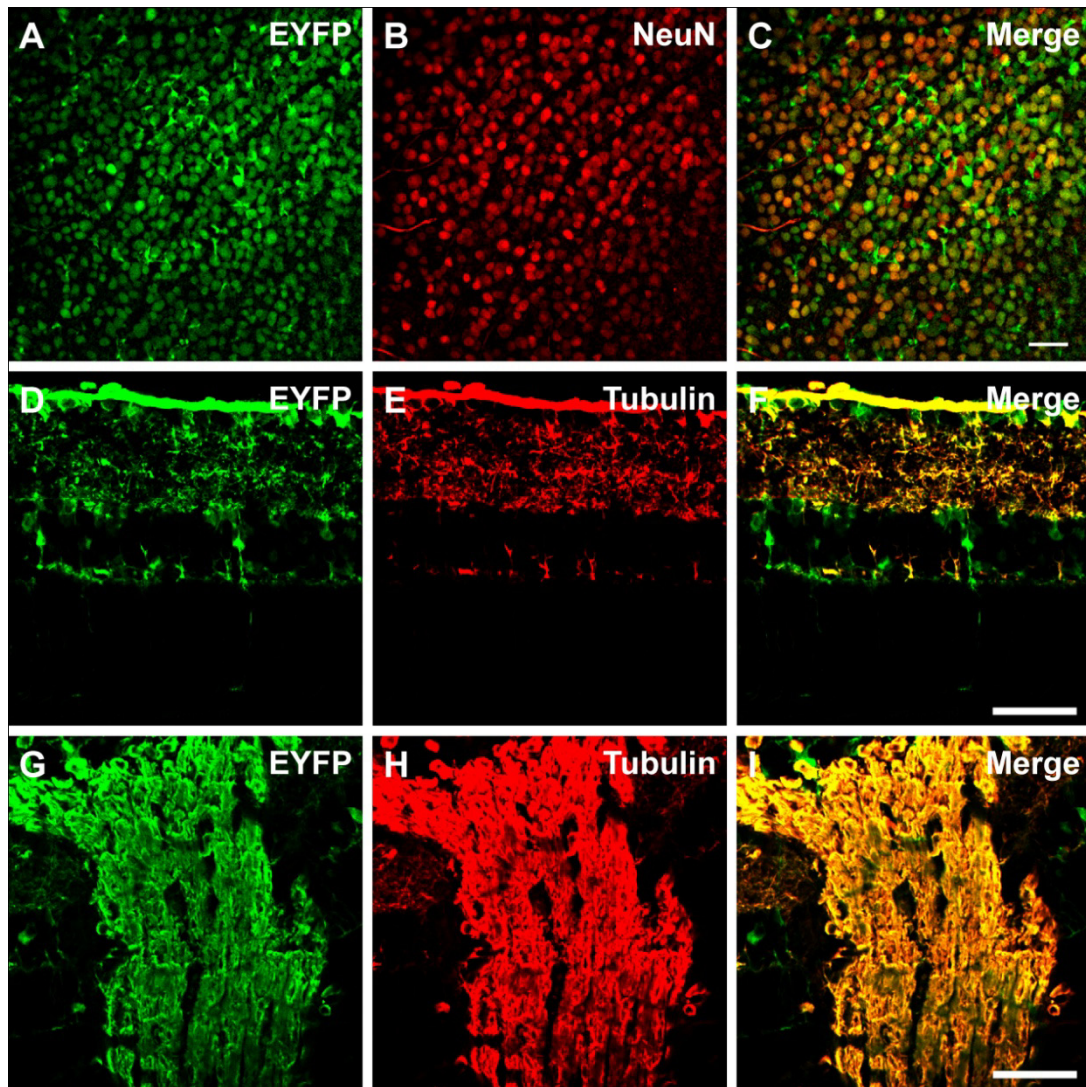


Figure 4-17. Efficiency and specificity of AAV-Cre transduction of RGCs

AAV-Cre vector was injected intravitreally into Rosa26-EYFP mice. Retinal whole-mounts (A-C), retinal cross sections (D-F) and optic nerve cross sections were examined after 3 weeks. The EYFP signal (A, D, G) was amplified with Alexa Fluor 488-conjugated antibodies directed against GFP, which also recognize EYFP. NeuN (B) was used as a marker for RGC somas, while RGC dendrites and axons were labeled with tubulin (E, H). Efficient transduction of RGCs is shown by robust immunoreactivity of the EYFP reporter, co-localizing with NeuN signals (C). In retinal cross section, tubulin⁺ RGC somas, axons and dendrites display AAV-Cre-mediated expression of EYFP in the GCL, NFL, and IPL (F). Some cells in the INL are also labeled, likely bipolar and amacrine cells. In the optic nerve, strong EYFP signaling is only observed on RGC axons (I). No other optic nerve cell types are labeled. Scale bar: 50 μ m.

Chapter 5

Conclusions

Summary of Findings

Glaucoma is a complex disease in which many cellular and molecular players have been implicated. While pharmacological modulation has yielded valuable information on pathophysiological mechanisms, genetic approaches offer additional specificity in targeting the molecules of interest, both spatially and temporally. In order to harness the power of mouse genetics, I began my dissertation research by trying to induce glaucoma experimentally via translimbal laser photocoagulation. My results, along with several other laboratories' (personal communications), indicate that the laser glaucoma model in C57BL/6 mice is less than satisfactory. Therefore, the first part of my dissertation is devoted to developing an alternative experimental model that would allow me and other investigators to study glaucoma in mice both pharmacologically and genetically. I demonstrate that using albino mice in this experimental protocol is advantageous in the ease of visualizing ocular vasculature. IOP elevation can be successfully induced and results in RGC soma and axon loss characteristic of glaucoma. My data also demonstrate that axon pathology precedes soma death, and is associated with remarkable disorganization and reactive plasticity.

Secondly, I used this new experimental model to investigate the role of Eph/ephrin signaling implicated in adult CNS injuries including glaucoma. Upregulation of several members of the EphB and ephrin-B families occur relatively early after IOP elevation. Concomitant increase of phosphorylated ephrin-B suggests activation of reverse signaling. Notably, genetic deletion of either EphB2 or EphB3 increases susceptibility to axonal degeneration induced by experimental mouse glaucoma. The involvement of Ephs and ephrins in glaucoma has been surmised for a while, based on

expression studies^{128,246} and microarray data (Gareth Howell, personal communications, 2008) in other animal models. This is the first demonstration that EphB receptors play a neuroprotective role in glaucoma at the functional level. In addition, C-terminally truncated EphB2 is only partially effective in mediating the function of axonal protection, indicating that signaling in both the forward and reverse directions is required. Although endogenous Eph/ephrin activation is transient and not sufficient to overcome the mechanisms that ultimately lead to axonal degeneration, understanding this pathway may lead to interventions that prolong or enhance its action and tip the balance toward neuroprotection.

Thirdly, I propose a mechanism of localized excitotoxicity that may offer new insight into glutamate's role in glaucoma. Corroborating immunohistochemical and ultrastructural analyses of the glaucomatous ONH reveal a localized accumulation of SV protein-expressing vesicles. These heterogeneously distributed ectopic vesicles can release glutamate via exocytosis, potentially leading to glutamate accumulation in focal hotspots. Immuno-localization studies suggest glutamate receptors are expressed on ONH axons, although the specificity of these antibodies need to be further established by additional control experiments. Functional assays demonstrate that ionotropic glutamate receptors are more active in experimental glaucoma, and pharmacological blockage of glutamate signaling preserves RGC axons *in vitro* and *in vivo*. Restricted deletion of VGLUT2 or NR1 in RGCs disrupts glutamate release or NMDA receptor activation, and significantly promotes axon survival *in vivo*. These data are consistent with a model in which vesicular glutamate release from ONH axons causes local excitotoxic damage to neighboring axons. This mechanism differs from the traditionally held theory of

excitotoxicity in that it occurs relatively early, and involves actively regulated components. The reliance of this pathway on vesicular fusion may present novel entry points that could be targeted to interfere with excitotoxic degeneration. A number of important questions remain to be answered. The present study does not adequately address the expression of NMDA, AMPA and kainate glutamate receptors on ONH axons, and their relative contribution to excitotoxicity. In addition, the relative importance of axonal versus somatic excitotoxic pathways and their spatial/temporal interactions need to be further elucidated.

Connecting Eph/ephrin Signaling and Glutamate Excitotoxicity

Is there a direct connection between the latter two parts of my dissertation? Do the EphB/ephrin-B signaling mechanisms interact with the glutamate excitotoxicity pathway? There is now an impressive body of literature on the role of Eph/ephrin signaling in modulating synaptic functions. For example, EphB2 promotes NMDA receptor clustering and calcium influx in a kinase-independent fashion¹⁸⁵⁻¹⁸⁶. At the mossy fiber-CA3 synapse, EphB2 activates AMPA receptor function, as well as enhancing the probability of presynaptic glutamate release via reverse signaling³⁹³. In the *Xenopus* retinotectal system, ephrin-B1 facilitates presynaptic transmitter release, and increase postsynaptic responsiveness³⁹⁴. The ability of Eph/ephrin to enhance excitatory transmission in some systems appears at odds with the results presented here. How can Eph/ephrin signaling be neuroprotective if it could potentiate the effect of excitotoxic stimuli? Firstly, it is important to point out that although this study demonstrates ectopic accumulation of SV

protein-containing vesicles, the ONH is still distinct from specialized synaptic regions. The mechanisms in normal synaptic plasticity and glaucomatous pathology may involve similar molecules but different outcome. The Eph/ephrin system is well-known for having paradoxical effects. Whether it mediates attractive or repulsive interactions could be highly context- and concentration-dependent^{156,395-396}. The downstream molecules that transduce Eph/ephrin signals likely exhibit different concentrations in a normally non-synaptic region (RGC axons) compared to synapses. Secondly, the glutamate receptor subtype most important for excitotoxicity at the ONH has not been conclusively demonstrated. This study did not investigate the involvement of kainate receptors, which may in part mediate the effect of glutamate. Whether kainate receptors interact with the Eph/ephrin system in normal physiology is unclear. Alternatively, Eph/ephrin and glutamate signaling could act independently in parallel pathways, but both affect the ultimate outcome of axonal degeneration via opposing downstream effectors.

Concluding Remarks

A number of themes have emerged from my research and readings on glaucoma. The concept of compartmentalization has been extensively discussed throughout this dissertation. My work led me to realize that compartmentalization may need to be appreciated at even finer levels than reviewed in the literature. The potential occurrence of “excitotoxic hotspots” at the ONH would suggest that not only do different compartments of the neuron launch distinct molecular programs in response to glaucoma, heterogeneity could occur within the same compartment. This idea could have profound

implications in drug design and delivery. Systemic delivery of neuroprotective agents may not achieve desirable concentration at the most relevant site of action. More localized and targeted delivery routes need to be developed to address this limitation. Furthermore, most neuroprotective strategies proposed to date focus on antagonizing pathogenic pathways. It is important to keep in mind that the outcome of glaucoma depends on a tug-of-war between endogenous protective and detrimental signals. The balance between these mechanisms may determine the differential susceptibility of individuals to glaucoma, even in the absence of IOP elevation. Novel strategies that aim at potentiating pro-survival pathways such as Eph/ephrin signaling in glaucoma could considerably expand the arsenal to fight this debilitating disease.

Chapter 6

References

1. Kaiser, H.J., Schoetzau, A., Stumpfig, D. & Flammer, J. Blood-flow velocities of the extraocular vessels in patients with high-tension and normal-tension primary open-angle glaucoma. *Am J Ophthalmol* **123**, 320-327 (1997).
2. Kerr, J., Nelson, P. & O'Brien, C. A comparison of ocular blood flow in untreated primary open-angle glaucoma and ocular hypertension. *Am J Ophthalmol* **126**, 42-51 (1998).
3. Michelson, G., Langhans, M.J. & Groh, M.J. Perfusion of the juxtapapillary retina and the neuroretinal rim area in primary open angle glaucoma. *J Glaucoma* **5**, 91-98 (1996).
4. Wolf, S., *et al.* Retinal hemodynamics using scanning laser ophthalmoscopy and hemorheology in chronic open-angle glaucoma. *Ophthalmology* **100**, 1561-1566 (1993).
5. Yamazaki, Y. & Drance, S.M. The relationship between progression of visual field defects and retrobulbar circulation in patients with glaucoma. *Am J Ophthalmol* **124**, 287-295 (1997).
6. Bosco, A., *et al.* Reduced retina microglial activation and improved optic nerve integrity with minocycline treatment in the DBA/2J mouse model of glaucoma. *Invest Ophthalmol Vis Sci* **49**, 1437-1446 (2008).
7. Neufeld, A.H., Sawada, A. & Becker, B. Inhibition of nitric-oxide synthase 2 by aminoguanidine provides neuroprotection of retinal ganglion cells in a rat model of chronic glaucoma. *Proc Natl Acad Sci U S A* **96**, 9944-9948 (1999).

8. Sappington, R.M. & Calkins, D.J. Contribution of TRPV1 to microglia-derived IL-6 and NFkappaB translocation with elevated hydrostatic pressure. *Invest Ophthalmol Vis Sci* **49**, 3004-3017 (2008).
9. Tezel, G. & Wax, M.B. Increased production of tumor necrosis factor-alpha by glial cells exposed to simulated ischemia or elevated hydrostatic pressure induces apoptosis in cocultured retinal ganglion cells. *J Neurosci* **20**, 8693-8700 (2000).
10. Ferreira, S.M., Lerner, S.F., Branzini, R., Evelson, P.A. & Llesuy, S.F. Oxidative stress markers in aqueous humor of glaucoma patients. *Am J Ophthalmol* **137**, 62-69 (2004).
11. Izzotti, A., Sacca, S.C., Cartiglia, C. & De Flora, S. Oxidative deoxyribonucleic acid damage in the eyes of glaucoma patients. *Am J Med* **114**, 638-646 (2003).
12. Levin, L.A., Clark, J.A. & Johns, L.K. Effect of lipid peroxidation inhibition on retinal ganglion cell death. *Invest Ophthalmol Vis Sci* **37**, 2744-2749 (1996).
13. Tezel, G. & Yang, X. Caspase-independent component of retinal ganglion cell death, in vitro. *Invest Ophthalmol Vis Sci* **45**, 4049-4059 (2004).
14. Tezel, G. & Yang, X. Comparative gene array analysis of TNF-alpha-induced MAPK and NF-kappaB signaling pathways between retinal ganglion cells and glial cells. *Exp Eye Res* **81**, 207-217 (2005).
15. Burgoyne, C.F., Downs, J.C., Bellezza, A.J. & Hart, R.T. Three-dimensional reconstruction of normal and early glaucoma monkey optic nerve head connective tissues. *Invest Ophthalmol Vis Sci* **45**, 4388-4399 (2004).

16. Downs, J.C., *et al.* Three-dimensional histomorphometry of the normal and early glaucomatous monkey optic nerve head: neural canal and subarachnoid space architecture. *Invest Ophthalmol Vis Sci* **48**, 3195-3208 (2007).
17. Quigley, H.A. & Addicks, E.M. Regional differences in the structure of the lamina cribrosa and their relation to glaucomatous optic nerve damage. *Arch Ophthalmol* **99**, 137-143 (1981).
18. Yang, H., Downs, J.C., Bellezza, A., Thompson, H. & Burgoyne, C.F. 3-D histomorphometry of the normal and early glaucomatous monkey optic nerve head: prelaminar neural tissues and cupping. *Invest Ophthalmol Vis Sci* **48**, 5068-5084 (2007).
19. Yang, H., *et al.* 3-D histomorphometry of the normal and early glaucomatous monkey optic nerve head: lamina cribrosa and peripapillary scleral position and thickness. *Invest Ophthalmol Vis Sci* **48**, 4597-4607 (2007).
20. Brooks, D.E., Garcia, G.A., Dreyer, E.B., Zurakowski, D. & Franco-Bourland, R.E. Vitreous body glutamate concentration in dogs with glaucoma. *Am J Vet Res* **58**, 864-867 (1997).
21. Chaudhary, P., Ahmed, F. & Sharma, S.C. MK801-a neuroprotectant in rat hypertensive eyes. *Brain Res* **792**, 154-158 (1998).
22. Dreyer, E.B., Zurakowski, D., Schumer, R.A., Podos, S.M. & Lipton, S.A. Elevated glutamate levels in the vitreous body of humans and monkeys with glaucoma. *Arch Ophthalmol* **114**, 299-305 (1996).

23. Guo, L., *et al.* Assessment of neuroprotective effects of glutamate modulation on glaucoma-related retinal ganglion cell apoptosis in vivo. *Invest Ophthalmol Vis Sci* **47**, 626-633 (2006).
24. Hare, W., *et al.* Efficacy and safety of memantine, an NMDA-type open-channel blocker, for reduction of retinal injury associated with experimental glaucoma in rat and monkey. *Surv Ophthalmol* **45 Suppl 3**, S284-289; discussion S295-286 (2001).
25. Low, H.C., Gionfriddo, J.R. & Madl, J.E. Assessment of glutamate loss from the ganglion cell layer of young DBA/2J mice with glaucoma. *Am J Vet Res* **67**, 302-309 (2006).
26. Nucci, C., *et al.* Neurochemical evidence to implicate elevated glutamate in the mechanisms of high intraocular pressure (IOP)-induced retinal ganglion cell death in rat. *Neurotoxicology* **26**, 935-941 (2005).
27. Schuettauf, F., *et al.* Alterations of amino acids and glutamate transport in the DBA/2J mouse retina; possible clues to degeneration. *Graefes Arch Clin Exp Ophthalmol* **245**, 1157-1168 (2007).
28. Pease, M.E., McKinnon, S.J., Quigley, H.A., Kerrigan-Baumrind, L.A. & Zack, D.J. Obstructed axonal transport of BDNF and its receptor TrkB in experimental glaucoma. *Invest Ophthalmol Vis Sci* **41**, 764-774 (2000).
29. Quigley, H.A., *et al.* Retrograde axonal transport of BDNF in retinal ganglion cells is blocked by acute IOP elevation in rats. *Invest Ophthalmol Vis Sci* **41**, 3460-3466 (2000).

30. Quigley, H.A. & Broman, A.T. The number of people with glaucoma worldwide in 2010 and 2020. *Br J Ophthalmol* **90**, 262-267 (2006).
31. Quigley, H.A. Glaucoma: macrocosm to microcosm the Friedenwald lecture. *Invest Ophthalmol Vis Sci* **46**, 2662-2670 (2005).
32. Boland, M.V. & Quigley, H.A. Risk factors and open-angle glaucoma: classification and application. *J Glaucoma* **16**, 406-418 (2007).
33. Chrysostomou, V., Trounce, I.A. & Crowston, J.G. Mechanisms of retinal ganglion cell injury in aging and glaucoma. *Ophthalmic Res* **44**, 173-178 (2010).
34. Kerrigan, L.A., Zack, D.J., Quigley, H.A., Smith, S.D. & Pease, M.E. TUNEL-positive ganglion cells in human primary open-angle glaucoma. *Arch Ophthalmol* **115**, 1031-1035 (1997).
35. Quigley, H.A., *et al.* Retinal ganglion cell death in experimental glaucoma and after axotomy occurs by apoptosis. *Invest Ophthalmol Vis Sci* **36**, 774-786 (1995).
36. Garcia-Valenzuela, E., Shareef, S., Walsh, J. & Sharma, S.C. Programmed cell death of retinal ganglion cells during experimental glaucoma. *Exp Eye Res* **61**, 33-44 (1995).
37. Quigley, H.A. Neuronal death in glaucoma. *Prog Retin Eye Res* **18**, 39-57 (1999).
38. Reichstein, D., Ren, L., Filippopoulos, T., Mittag, T. & Danias, J. Apoptotic retinal ganglion cell death in the DBA/2 mouse model of glaucoma. *Exp Eye Res* (2006).
39. Qu, J., Wang, D. & Grosskreutz, C.L. Mechanisms of retinal ganglion cell injury and defense in glaucoma. *Exp Eye Res* **91**, 48-53 (2010).

40. Green, D.R. & Reed, J.C. Mitochondria and apoptosis. *Science* **281**, 1309-1312 (1998).
41. Hanninen, V.A., Pantcheva, M.B., Freeman, E.E., Poulin, N.R. & Grosskreutz, C.L. Activation of caspase 9 in a rat model of experimental glaucoma. *Curr Eye Res* **25**, 389-395 (2002).
42. Huang, W., *et al.* Transcriptional up-regulation and activation of initiating caspases in experimental glaucoma. *Am J Pathol* **167**, 673-681 (2005).
43. Libby, R.T., *et al.* Susceptibility to neurodegeneration in a glaucoma is modified by Bax gene dosage. *PLoS Genet* **1**, 17-26 (2005).
44. Ashkenazi, A. & Dixit, V.M. Death receptors: signaling and modulation. *Science* **281**, 1305-1308 (1998).
45. Kim, H.S. & Park, C.K. Retinal ganglion cell death is delayed by activation of retinal intrinsic cell survival program. *Brain Res* **1057**, 17-28 (2005).
46. McKinnon, S.J., *et al.* Caspase activation and amyloid precursor protein cleavage in rat ocular hypertension. *Invest Ophthalmol Vis Sci* **43**, 1077-1087 (2002).
47. Whitmore, A.V., Libby, R.T. & John, S.W. Glaucoma: Thinking in new ways-a role for autonomous axonal self-destruction and other compartmentalised processes? *Prog Retin Eye Res* (2005).
48. Howell, G.R., *et al.* Axons of retinal ganglion cells are insulted in the optic nerve early in DBA/2J glaucoma. *J Cell Biol* **179**, 1523-1537 (2007).
49. Beirowski, B., Babetto, E., Coleman, M.P. & Martin, K.R. The WldS gene delays axonal but not somatic degeneration in a rat glaucoma model. *Eur J Neurosci* **28**, 1166-1179 (2008).

50. Weber, A.J., Kaufman, P.L. & Hubbard, W.C. Morphology of single ganglion cells in the glaucomatous primate retina. *Invest Ophthalmol Vis Sci* **39**, 2304-2320 (1998).
51. Shou, T., Liu, J., Wang, W., Zhou, Y. & Zhao, K. Differential dendritic shrinkage of alpha and beta retinal ganglion cells in cats with chronic glaucoma. *Invest Ophthalmol Vis Sci* **44**, 3005-3010 (2003).
52. Morgan, J.E., Datta, A.V., Erichsen, J.T., Albon, J. & Boulton, M.E. Retinal ganglion cell remodelling in experimental glaucoma. *Adv Exp Med Biol* **572**, 397-402 (2006).
53. Weber, A.J. & Harman, C.D. Structure-function relations of parasol cells in the normal and glaucomatous primate retina. *Invest Ophthalmol Vis Sci* **46**, 3197-3207 (2005).
54. Stevens, B., *et al.* The classical complement cascade mediates CNS synapse elimination. *Cell* **131**, 1164-1178 (2007).
55. Wygnanski, T., Desatnik, H., Quigley, H.A. & Glovinsky, Y. Comparison of ganglion cell loss and cone loss in experimental glaucoma. *Am J Ophthalmol* **120**, 184-189 (1995).
56. Vickers, J.C., *et al.* Differential vulnerability of neurochemically identified subpopulations of retinal neurons in a monkey model of glaucoma. *Brain Res* **680**, 23-35 (1995).
57. Kendell, K.R., Quigley, H.A., Kerrigan, L.A., Pease, M.E. & Quigley, E.N. Primary open-angle glaucoma is not associated with photoreceptor loss. *Invest Ophthalmol Vis Sci* **36**, 200-205 (1995).

58. Jakobs, T.C., Libby, R.T., Ben, Y., John, S.W. & Masland, R.H. Retinal ganglion cell degeneration is topological but not cell type specific in DBA/2J mice. *J Cell Biol* **171**, 313-325 (2005).
59. Quigley, H.A., Addicks, E.M., Green, W.R. & Maumenee, A.E. Optic nerve damage in human glaucoma. II. The site of injury and susceptibility to damage. *Arch Ophthalmol* **99**, 635-649 (1981).
60. Soto, I., *et al.* Retinal ganglion cells downregulate gene expression and lose their axons within the optic nerve head in a mouse glaucoma model. *J Neurosci* **28**, 548-561 (2008).
61. Buckingham, B.P., *et al.* Progressive ganglion cell degeneration precedes neuronal loss in a mouse model of glaucoma. *J Neurosci* **28**, 2735-2744 (2008).
62. Morrison, J.C., *et al.* A rat model of chronic pressure-induced optic nerve damage. *Exp Eye Res* **64**, 85-96 (1997).
63. Quigley, H.A. & Addicks, E.M. Chronic experimental glaucoma in primates. II. Effect of extended intraocular pressure elevation on optic nerve head and axonal transport. *Invest Ophthalmol Vis Sci* **19**, 137-152 (1980).
64. Anderson, D.R. & Hendrickson, A. Effect of intraocular pressure on rapid axoplasmic transport in monkey optic nerve. *Invest Ophthalmol* **13**, 771-783 (1974).
65. Minckler, D.S., Tso, M.O. & Zimmerman, L.E. A light microscopic, autoradiographic study of axoplasmic transport in the optic nerve head during ocular hypotony, increased intraocular pressure, and papilledema. *Am J Ophthalmol* **82**, 741-757 (1976).

66. Burgoyne, C.F., Downs, J.C., Bellezza, A.J., Suh, J.K. & Hart, R.T. The optic nerve head as a biomechanical structure: a new paradigm for understanding the role of IOP-related stress and strain in the pathophysiology of glaucomatous optic nerve head damage. *Prog Retin Eye Res* **24**, 39-73 (2005).
67. Fechtner, R.D. & Weinreb, R.N. Mechanisms of optic nerve damage in primary open angle glaucoma. *Surv Ophthalmol* **39**, 23-42 (1994).
68. Grieshaber, M.C. & Flammer, J. Blood flow in glaucoma. *Curr Opin Ophthalmol* **16**, 79-83 (2005).
69. Agapova, O.A., Kaufman, P.L., Lucarelli, M.J., Gabelt, B.T. & Hernandez, M.R. Differential expression of matrix metalloproteinases in monkey eyes with experimental glaucoma or optic nerve transection. *Brain Res* **967**, 132-143 (2003).
70. Hernandez, M.R. Ultrastructural immunocytochemical analysis of elastin in the human lamina cribrosa. Changes in elastic fibers in primary open-angle glaucoma. *Invest Ophthalmol Vis Sci* **33**, 2891-2903 (1992).
71. Hernandez, M.R., Andrzejewska, W.M. & Neufeld, A.H. Changes in the extracellular matrix of the human optic nerve head in primary open-angle glaucoma. *Am J Ophthalmol* **109**, 180-188 (1990).
72. Morrison, J.C., Dorman-Pease, M.E., Dunkelberger, G.R. & Quigley, H.A. Optic nerve head extracellular matrix in primary optic atrophy and experimental glaucoma. *Arch Ophthalmol* **108**, 1020-1024 (1990).
73. Quigley, H.A., Brown, A. & Dorman-Pease, M.E. Alterations in elastin of the optic nerve head in human and experimental glaucoma. *Br J Ophthalmol* **75**, 552-557 (1991).

74. Quigley, H.A., Dorman-Pease, M.E. & Brown, A.E. Quantitative study of collagen and elastin of the optic nerve head and sclera in human and experimental monkey glaucoma. *Curr Eye Res* **10**, 877-888 (1991).
75. Neufeld, A.H. & Liu, B. Glaucomatous optic neuropathy: when glia misbehave. *Neuroscientist* **9**, 485-495 (2003).
76. Hernandez, M.R. The optic nerve head in glaucoma: role of astrocytes in tissue remodeling. *Prog Retin Eye Res* **19**, 297-321 (2000).
77. Johnson, E.C. & Morrison, J.C. Friend or foe? Resolving the impact of glial responses in glaucoma. *J Glaucoma* **18**, 341-353 (2009).
78. Lambiase, A., *et al.* Experimental and clinical evidence of neuroprotection by nerve growth factor eye drops: Implications for glaucoma. *Proc Natl Acad Sci U S A* (2009).
79. Mansour-Robaey, S., Clarke, D.B., Wang, Y.C., Bray, G.M. & Aguayo, A.J. Effects of ocular injury and administration of brain-derived neurotrophic factor on survival and regrowth of axotomized retinal ganglion cells. *Proc Natl Acad Sci U S A* **91**, 1632-1636 (1994).
80. Ko, M.L., Hu, D.N., Ritch, R., Sharma, S.C. & Chen, C.F. Patterns of retinal ganglion cell survival after brain-derived neurotrophic factor administration in hypertensive eyes of rats. *Neurosci Lett* **305**, 139-142 (2001).
81. Di Polo, A., Aigner, L.J., Dunn, R.J., Bray, G.M. & Aguayo, A.J. Prolonged delivery of brain-derived neurotrophic factor by adenovirus-infected Muller cells temporarily rescues injured retinal ganglion cells. *Proc Natl Acad Sci U S A* **95**, 3978-3983 (1998).

82. Pease, M.E., *et al.* Effect of CNTF on retinal ganglion cell survival in experimental glaucoma. *Invest Ophthalmol Vis Sci* **50**, 2194-2200 (2009).
83. Liu, B. & Neufeld, A.H. Expression of nitric oxide synthase-2 (NOS-2) in reactive astrocytes of the human glaucomatous optic nerve head. *Glia* **30**, 178-186 (2000).
84. Tezel, G. & Wax, M.B. Glial modulation of retinal ganglion cell death in glaucoma. *J Glaucoma* **12**, 63-68 (2003).
85. Sattler, R. & Tymianski, M. Molecular mechanisms of glutamate receptor-mediated excitotoxic neuronal cell death. *Mol Neurobiol* **24**, 107-129 (2001).
86. Lau, A. & Tymianski, M. Glutamate receptors, neurotoxicity and neurodegeneration. *Pflugers Arch* (2010).
87. Matute, C. Calcium dyshomeostasis in white matter pathology. *Cell Calcium* **47**, 150-157 (2010).
88. Wang, Q., Yu, S., Simonyi, A., Sun, G.Y. & Sun, A.Y. Kainic acid-mediated excitotoxicity as a model for neurodegeneration. *Mol Neurobiol* **31**, 3-16 (2005).
89. Caprioli, J., Kitano, S. & Morgan, J.E. Hyperthermia and hypoxia increase tolerance of retinal ganglion cells to anoxia and excitotoxicity. *Invest Ophthalmol Vis Sci* **37**, 2376-2381 (1996).
90. Izumi, Y., *et al.* An ex vivo rat retinal preparation for excitotoxicity studies. *J Neurosci Methods* **60**, 219-225 (1995).
91. Li, Y., Schlamp, C.L. & Nickells, R.W. Experimental induction of retinal ganglion cell death in adult mice. *Invest Ophthalmol Vis Sci* **40**, 1004-1008 (1999).

92. Lucas, D.R. & Newhouse, J.P. The toxic effect of sodium L-glutamate on the inner layers of the retina. *AMA Arch Ophthalmol* **58**, 193-201 (1957).
93. Mosinger, J.L., *et al.* Blockade of both NMDA and non-NMDA receptors is required for optimal protection against ischemic neuronal degeneration in the in vivo adult mammalian retina. *Exp Neurol* **113**, 10-17 (1991).
94. Sabel, B.A., Sautter, J., Stoehr, T. & Siliprandi, R. A behavioral model of excitotoxicity: retinal degeneration, loss of vision, and subsequent recovery after intraocular NMDA administration in adult rats. *Exp Brain Res* **106**, 93-105 (1995).
95. Sisk, D.R. & Kuwabara, T. Histologic changes in the inner retina of albino rats following intravitreal injection of monosodium L-glutamate. *Graefes Arch Clin Exp Ophthalmol* **223**, 250-258 (1985).
96. Ullian, E.M., Barkis, W.B., Chen, S., Diamond, J.S. & Barres, B.A. Invulnerability of retinal ganglion cells to NMDA excitotoxicity. *Mol Cell Neurosci* **26**, 544-557 (2004).
97. Carter-Dawson, L., *et al.* Vitreal glutamate concentration in monkeys with experimental glaucoma. *Invest Ophthalmol Vis Sci* **43**, 2633-2637 (2002).
98. Honkanen, R.A., *et al.* Vitreous amino acid concentrations in patients with glaucoma undergoing vitrectomy. *Arch Ophthalmol* **121**, 183-188 (2003).
99. Levkovitch-Verbin, H., *et al.* Measurement of amino acid levels in the vitreous humor of rats after chronic intraocular pressure elevation or optic nerve transection. *J Glaucoma* **11**, 396-405 (2002).
100. Wamsley, S., *et al.* Vitreous glutamate concentration and axon loss in monkeys with experimental glaucoma. *Arch Ophthalmol* **123**, 64-70 (2005).

101. Tezel, G. Oxidative stress in glaucomatous neurodegeneration: mechanisms and consequences. *Prog Retin Eye Res* **25**, 490-513 (2006).
102. Kumar, D.M. & Agarwal, N. Oxidative stress in glaucoma: a burden of evidence. *J Glaucoma* **16**, 334-343 (2007).
103. Neufeld, A.H. Nitric oxide: a potential mediator of retinal ganglion cell damage in glaucoma. *Surv Ophthalmol* **43 Suppl 1**, S129-135 (1999).
104. Levkovitch-Verbin, H. Animal models of optic nerve diseases. *Eye* **18**, 1066-1074 (2004).
105. McKinnon, S.J., Schlamp, C.L. & Nickells, R.W. Mouse models of retinal ganglion cell death and glaucoma. *Exp Eye Res* **88**, 816-824 (2009).
106. Pang, I.H. & Clark, A.F. Rodent models for glaucoma retinopathy and optic neuropathy. *J Glaucoma* **16**, 483-505 (2007).
107. Rasmussen, C.A. & Kaufman, P.L. Primate glaucoma models. *J Glaucoma* **14**, 311-314 (2005).
108. Weinreb, R.N. & Lindsey, J.D. The importance of models in glaucoma research. *J Glaucoma* **14**, 302-304 (2005).
109. Libby, R.T., *et al.* Inherited glaucoma in DBA/2J mice: Pertinent disease features for studying the neurodegeneration. *Vis Neurosci* **22**, 637-648 (2005).
110. Austad, S.N. Issues in the choice of genetic configuration for animal aging models. *Exp Gerontol* **32**, 55-63 (1997).
111. Nakazawa, T., *et al.* Tumor necrosis factor-alpha mediates oligodendrocyte death and delayed retinal ganglion cell loss in a mouse model of glaucoma. *J Neurosci* **26**, 12633-12641 (2006).

112. Aihara, M., Lindsey, J.D. & Weinreb, R.N. Experimental mouse ocular hypertension: establishment of the model. *Invest Ophthalmol Vis Sci* **44**, 4314-4320 (2003).
113. Gross, R.L., *et al.* A mouse model of elevated intraocular pressure: retina and optic nerve findings. *Trans Am Ophthalmol Soc* **101**, 163-169; discussion 169-171 (2003).
114. Grozdanic, S.D., *et al.* Laser-induced mouse model of chronic ocular hypertension. *Invest Ophthalmol Vis Sci* **44**, 4337-4346 (2003).
115. Gaasterland, D. & Kupfer, C. Experimental glaucoma in the rhesus monkey. *Invest Ophthalmol* **13**, 455-457 (1974).
116. Quigley, H.A. & Hohman, R.M. Laser energy levels for trabecular meshwork damage in the primate eye. *Invest Ophthalmol Vis Sci* **24**, 1305-1307 (1983).
117. Levkovitch-Verbin, H., *et al.* Translimbal laser photocoagulation to the trabecular meshwork as a model of glaucoma in rats. *Invest Ophthalmol Vis Sci* **43**, 402-410 (2002).
118. Ueda, J., *et al.* Experimental glaucoma model in the rat induced by laser trabecular photocoagulation after an intracameral injection of India ink. *Jpn J Ophthalmol* **42**, 337-344 (1998).
119. WoldeMussie, E., Ruiz, G., Wijono, M. & Wheeler, L.A. Neuroprotection of retinal ganglion cells by brimonidine in rats with laser-induced chronic ocular hypertension. *Invest Ophthalmol Vis Sci* **42**, 2849-2855 (2001).

120. Shareef, S.R., Garcia-Valenzuela, E., Salierno, A., Walsh, J. & Sharma, S.C. Chronic ocular hypertension following episcleral venous occlusion in rats. *Exp Eye Res* **61**, 379-382 (1995).
121. Ruiz-Ederra, J. & Verkman, A.S. Mouse model of sustained elevation in intraocular pressure produced by episcleral vein occlusion. *Exp Eye Res* **82**, 879-884 (2006).
122. Yu, S., Tanabe, T. & Yoshimura, N. A rat model of glaucoma induced by episcleral vein ligation. *Exp Eye Res* **83**, 758-770 (2006).
123. Moreno, M.C., *et al.* A new experimental model of glaucoma in rats through intracameral injections of hyaluronic acid. *Exp Eye Res* **81**, 71-80 (2005).
124. Weber, A.J. & Zelenak, D. Experimental glaucoma in the primate induced by latex microspheres. *J Neurosci Methods* **111**, 39-48 (2001).
125. Sappington, R.M., Carlson, B.J., Crish, S.D. & Calkins, D. The Microbead Occlusion Model: A Paradigm for Induced Ocular Hypertension in Rats and Mice. *Invest Ophthalmol Vis Sci* (2009).
126. Urcola, J.H., Hernandez, M. & Vecino, E. Three experimental glaucoma models in rats: comparison of the effects of intraocular pressure elevation on retinal ganglion cell size and death. *Exp Eye Res* **83**, 429-437 (2006).
127. Savinova, O.V., *et al.* Intraocular pressure in genetically distinct mice: an update and strain survey. *BMC Genet* **2**, 12 (2001).
128. Du, J., Tran, T., Fu, C. & Sretavan, D.W. Upregulation of EphB2 and ephrin-B2 at the Optic Nerve Head of DBA/2J Glaucomatous Mice Coincides with Axon Loss. *Invest Ophthalmol Vis Sci* **48**, 5567-5581 (2007).

129. Bartsch, S., Montag, D., Schachner, M. & Bartsch, U. Increased number of unmyelinated axons in optic nerves of adult mice deficient in the myelin-associated glycoprotein (MAG). *Brain Res* **762**, 231-234 (1997).
130. Leahy, K.M., *et al.* Quantitative ex vivo detection of rodent retinal ganglion cells by immunolabeling Brn-3b. *Exp Eye Res* **79**, 131-140 (2004).
131. Desai, K.H., *et al.* Cardiovascular indexes in the mouse at rest and with exercise: new tools to study models of cardiac disease. *Am J Physiol* **272**, H1053-1061 (1997).
132. Hayreh, S.S. The 1994 Von Sallman Lecture. The optic nerve head circulation in health and disease. *Exp Eye Res* **61**, 259-272 (1995).
133. Drager, U.C. & Olsen, J.F. Ganglion cell distribution in the retina of the mouse. *Invest Ophthalmol Vis Sci* **20**, 285-293 (1981).
134. Jeon, C.J., Strettoi, E. & Masland, R.H. The major cell populations of the mouse retina. *J Neurosci* **18**, 8936-8946 (1998).
135. Li, Y., Semaan, S.J., Schlamp, C.L. & Nickells, R.W. Dominant inheritance of retinal ganglion cell resistance to optic nerve crush in mice. *BMC Neurosci* **8**, 19 (2007).
136. Kielczewski, J.L., Pease, M.E. & Quigley, H.A. The effect of experimental glaucoma and optic nerve transection on amacrine cells in the rat retina. *Invest Ophthalmol Vis Sci* **46**, 3188-3196 (2005).
137. Xiang, M., *et al.* Brn-3b: a POU domain gene expressed in a subset of retinal ganglion cells. *Neuron* **11**, 689-701 (1993).

138. Schlamp, C.L., Li, Y., Dietz, J.A., Janssen, K.T. & Nickells, R.W. Progressive ganglion cell loss and optic nerve degeneration in DBA/2J mice is variable and asymmetric. *BMC Neurosci* **7**, 66 (2006).
139. Liu, X., Hawkes, E., Ishimaru, T., Tran, T. & Sretavan, D.W. EphB3: an endogenous mediator of adult axonal plasticity and regrowth after CNS injury. *J Neurosci* **26**, 3087-3101 (2006).
140. Buckmaster, P.S., Zhang, G.F. & Yamawaki, R. Axon sprouting in a model of temporal lobe epilepsy creates a predominantly excitatory feedback circuit. *J Neurosci* **22**, 6650-6658 (2002).
141. Cajal, R. *Degeneration and regeneration of the nervous system*, (Oxford University Press, London, 1928).
142. Chuckowree, J.A., Dickson, T.C. & Vickers, J.C. Intrinsic regenerative ability of mature CNS neurons. *Neuroscientist* **10**, 280-285 (2004).
143. Dancause, N., *et al.* Extensive cortical rewiring after brain injury. *J Neurosci* **25**, 10167-10179 (2005).
144. Fitch, M.T. & Silver, J. CNS injury, glial scars, and inflammation: Inhibitory extracellular matrices and regeneration failure. *Exp Neurol* **209**, 294-301 (2008).
145. Waxman, S.G. Axonal conduction and injury in multiple sclerosis: the role of sodium channels. *Nat Rev Neurosci* **7**, 932-941 (2006).
146. Li, S. & Stys, P.K. Mechanisms of ionotropic glutamate receptor-mediated excitotoxicity in isolated spinal cord white matter. *J Neurosci* **20**, 1190-1198 (2000).

147. Matsuo, A., *et al.* Unmasking of an unusual myelin basic protein epitope during the process of myelin degeneration in humans: a potential mechanism for the generation of autoantigens. *Am J Pathol* **150**, 1253-1266 (1997).
148. Mabuchi, F., Aihara, M., Mackey, M.R., Lindsey, J.D. & Weinreb, R.N. Optic nerve damage in experimental mouse ocular hypertension. *Invest Ophthalmol Vis Sci* **44**, 4321-4330 (2003).
149. Levin, L.A. Retinal ganglion cells and neuroprotection for glaucoma. *Surv Ophthalmol* **48 Suppl 1**, S21-24 (2003).
150. Masliah, E., *et al.* Patterns of aberrant sprouting in Alzheimer's disease. *Neuron* **6**, 729-739 (1991).
151. Phinney, A.L., *et al.* Cerebral amyloid induces aberrant axonal sprouting and ectopic terminal formation in amyloid precursor protein transgenic mice. *J Neurosci* **19**, 8552-8559 (1999).
152. Johnson, E.C., Deppmeier, L.M., Wentzien, S.K., Hsu, I. & Morrison, J.C. Chronology of optic nerve head and retinal responses to elevated intraocular pressure. *Invest Ophthalmol Vis Sci* **41**, 431-442 (2000).
153. Pena, J.D., Taylor, A.W., Ricard, C.S., Vidal, I. & Hernandez, M.R. Transforming growth factor beta isoforms in human optic nerve heads. *Br J Ophthalmol* **83**, 209-218 (1999).
154. Lemke, G. A coherent nomenclature for Eph receptors and their ligands. *Mol Cell Neurosci* **9**, 331-332 (1997).
155. Klein, R. Eph/ephrin signaling in morphogenesis, neural development and plasticity. *Curr Opin Cell Biol* **16**, 580-589 (2004).

156. Pasquale, E.B. Eph receptor signalling casts a wide net on cell behaviour. *Nat Rev Mol Cell Biol* **6**, 462-475 (2005).
157. Martinez, A. & Soriano, E. Functions of ephrin/Eph interactions in the development of the nervous system: emphasis on the hippocampal system. *Brain Res Brain Res Rev* **49**, 211-226 (2005).
158. Song, J., *et al.* Solution structure and backbone dynamics of the functional cytoplasmic subdomain of human ephrin B2, a cell-surface ligand with bidirectional signaling properties. *Biochemistry* **41**, 10942-10949 (2002).
159. Torres, R., *et al.* PDZ proteins bind, cluster, and synaptically colocalize with Eph receptors and their ephrin ligands. *Neuron* **21**, 1453-1463 (1998).
160. Flanagan, J.G. & Vanderhaeghen, P. The ephrins and Eph receptors in neural development. *Annu Rev Neurosci* **21**, 309-345 (1998).
161. Palmer, A. & Klein, R. Multiple roles of ephrins in morphogenesis, neuronal networking, and brain function. *Genes Dev* **17**, 1429-1450 (2003).
162. Wilkinson, D.G. Multiple roles of EPH receptors and ephrins in neural development. *Nat Rev Neurosci* **2**, 155-164 (2001).
163. Cheng, H.J., Nakamoto, M., Bergemann, A.D. & Flanagan, J.G. Complementary gradients in expression and binding of ELF-1 and Mek4 in development of the topographic retinotectal projection map. *Cell* **82**, 371-381 (1995).
164. Feldheim, D.A., *et al.* Genetic analysis of ephrin-A2 and ephrin-A5 shows their requirement in multiple aspects of retinocollicular mapping. *Neuron* **25**, 563-574 (2000).

165. Brown, A., *et al.* Topographic mapping from the retina to the midbrain is controlled by relative but not absolute levels of EphA receptor signaling. *Cell* **102**, 77-88 (2000).
166. Hindges, R., McLaughlin, T., Genoud, N., Henkemeyer, M. & O'Leary, D.D. EphB forward signaling controls directional branch extension and arborization required for dorsal-ventral retinotopic mapping. *Neuron* **35**, 475-487 (2002).
167. Mann, F., Ray, S., Harris, W. & Holt, C. Topographic mapping in dorsoventral axis of the *Xenopus* retinotectal system depends on signaling through ephrin-B ligands. *Neuron* **35**, 461-473 (2002).
168. McLaughlin, T., Hindges, R., Yates, P.A. & O'Leary, D.D. Bifunctional action of ephrin-B1 as a repellent and attractant to control bidirectional branch extension in dorsal-ventral retinotopic mapping. *Development* **130**, 2407-2418 (2003).
169. Huberman, A.D., Murray, K.D., Warland, D.K., Feldheim, D.A. & Chapman, B. Ephrin-As mediate targeting of eye-specific projections to the lateral geniculate nucleus. *Nat Neurosci* **8**, 1013-1021 (2005).
170. Pfeiffenberger, C., *et al.* Ephrin-As and neural activity are required for eye-specific patterning during retinogeniculate mapping. *Nat Neurosci* **8**, 1022-1027 (2005).
171. Cang, J., *et al.* Ephrin-as guide the formation of functional maps in the visual cortex. *Neuron* **48**, 577-589 (2005).
172. Dufour, A., *et al.* Area specificity and topography of thalamocortical projections are controlled by ephrin/Eph genes. *Neuron* **39**, 453-465 (2003).

173. Torii, M. & Levitt, P. Dissociation of corticothalamic and thalamocortical axon targeting by an EphA7-mediated mechanism. *Neuron* **48**, 563-575 (2005).
174. Vanderhaeghen, P., *et al.* A mapping label required for normal scale of body representation in the cortex. *Nat Neurosci* **3**, 358-365 (2000).
175. Knoll, B., Zarbali, K., Wurst, W. & Drescher, U. A role for the EphA family in the topographic targeting of vomeronasal axons. *Development* **128**, 895-906 (2001).
176. Gao, P.P., *et al.* Regulation of topographic projection in the brain: Elf-1 in the hippocamposeptal system. *Proc Natl Acad Sci U S A* **93**, 11161-11166 (1996).
177. Yue, Y., *et al.* Mistargeting hippocampal axons by expression of a truncated Eph receptor. *Proc Natl Acad Sci U S A* **99**, 10777-10782 (2002).
178. Cramer, K.S., Bermingham-McDonogh, O., Krull, C.E. & Rubel, E.W. EphA4 signaling promotes axon segregation in the developing auditory system. *Dev Biol* **269**, 26-35 (2004).
179. Person, A.L., Cerretti, D.P., Pasquale, E.B., Rubel, E.W. & Cramer, K.S. Tonotopic gradients of Eph family proteins in the chick nucleus laminaris during synaptogenesis. *J Neurobiol* **60**, 28-39 (2004).
180. Siddiqui, S.A. & Cramer, K.S. Differential expression of Eph receptors and ephrins in the cochlear ganglion and eighth cranial nerve of the chick embryo. *J Comp Neurol* **482**, 309-319 (2005).
181. Yamaguchi, Y. & Pasquale, E.B. Eph receptors in the adult brain. *Curr Opin Neurobiol* **14**, 288-296 (2004).

182. Henkemeyer, M., Itkis, O.S., Ngo, M., Hickmott, P.W. & Ethell, I.M. Multiple EphB receptor tyrosine kinases shape dendritic spines in the hippocampus. *J Cell Biol* **163**, 1313-1326 (2003).
183. Ethell, I.M., *et al.* EphB/syndecan-2 signaling in dendritic spine morphogenesis. *Neuron* **31**, 1001-1013 (2001).
184. Murai, K.K., Nguyen, L.N., Irie, F., Yamaguchi, Y. & Pasquale, E.B. Control of hippocampal dendritic spine morphology through ephrin-A3/EphA4 signaling. *Nat Neurosci* **6**, 153-160 (2003).
185. Takasu, M.A., Dalva, M.B., Zigmond, R.E. & Greenberg, M.E. Modulation of NMDA receptor-dependent calcium influx and gene expression through EphB receptors. *Science* **295**, 491-495 (2002).
186. Dalva, M.B., *et al.* EphB receptors interact with NMDA receptors and regulate excitatory synapse formation. *Cell* **103**, 945-956 (2000).
187. Armstrong, J.N., *et al.* B-ephrin reverse signaling is required for NMDA-independent long-term potentiation of mossy fibers in the hippocampus. *J Neurosci* **26**, 3474-3481 (2006).
188. Grunwald, I.C., *et al.* Hippocampal plasticity requires postsynaptic ephrinBs. *Nat Neurosci* **7**, 33-40 (2004).
189. Henderson, J.T., *et al.* The receptor tyrosine kinase EphB2 regulates NMDA-dependent synaptic function. *Neuron* **32**, 1041-1056 (2001).
190. Grunwald, I.C., *et al.* Kinase-independent requirement of EphB2 receptors in hippocampal synaptic plasticity. *Neuron* **32**, 1027-1040 (2001).

191. Battaglia, A.A., Sehayek, K., Grist, J., McMahon, S.B. & Gavazzi, I. EphB receptors and ephrin-B ligands regulate spinal sensory connectivity and modulate pain processing. *Nature Neuroscience* **6**, 339-340 (2003).
192. Depaepe, V., *et al.* Ephrin signalling controls brain size by regulating apoptosis of neural progenitors. *Nature* **435**, 1244-1250 (2005).
193. Katakowski, M., Zhang, Z., Decarvalho, A.C. & Chopp, M. EphB2 induces proliferation and promotes a neuronal fate in adult subventricular neural precursor cells. *Neurosci Lett* **385**, 204-209 (2005).
194. Ricard, J., Salinas, J., Garcia, L. & Liebl, D.J. EphrinB3 regulates cell proliferation and survival in adult neurogenesis. *Mol Cell Neurosci* **31**, 713-722 (2006).
195. Holmberg, J., *et al.* Ephrin-A2 reverse signaling negatively regulates neural progenitor proliferation and neurogenesis. *Genes Dev* **19**, 462-471 (2005).
196. Conover, J.C., *et al.* Disruption of Eph/ephrin signaling affects migration and proliferation in the adult subventricular zone. *Nat Neurosci* **3**, 1091-1097 (2000).
197. Aoki, M., Yamashita, T. & Tohyama, M. EphA receptors direct the differentiation of mammalian neural precursor cells through a mitogen-activated protein kinase-dependent pathway. *J Biol Chem* **279**, 32643-32650 (2004).
198. Gerety, S.S., Wang, H.U., Chen, Z.F. & Anderson, D.J. Symmetrical mutant phenotypes of the receptor EphB4 and its specific transmembrane ligand ephrin-B2 in cardiovascular development. *Mol Cell* **4**, 403-414 (1999).

199. Adams, R.H., *et al.* Roles of ephrinB ligands and EphB receptors in cardiovascular development: demarcation of arterial/venous domains, vascular morphogenesis, and sprouting angiogenesis. *Genes Dev* **13**, 295-306 (1999).
200. Gale, N.W., *et al.* Ephrin-B2 selectively marks arterial vessels and neovascularization sites in the adult, with expression in both endothelial and smooth-muscle cells. *Dev Biol* **230**, 151-160 (2001).
201. Shin, D., *et al.* Expression of ephrinB2 identifies a stable genetic difference between arterial and venous vascular smooth muscle as well as endothelial cells, and marks subsets of microvessels at sites of adult neovascularization. *Dev Biol* **230**, 139-150 (2001).
202. Brantley, D.M., *et al.* Soluble Eph A receptors inhibit tumor angiogenesis and progression in vivo. *Oncogene* **21**, 7011-7026 (2002).
203. Noren, N.K., Lu, M., Freeman, A.L., Koolpe, M. & Pasquale, E.B. Interplay between EphB4 on tumor cells and vascular ephrin-B2 regulates tumor growth. *Proc Natl Acad Sci U S A* **101**, 5583-5588 (2004).
204. Brantley-Sieders, D.M., *et al.* Impaired tumor microenvironment in EphA2-deficient mice inhibits tumor angiogenesis and metastatic progression. *Faseb J* **19**, 1884-1886 (2005).
205. Surawska, H., Ma, P.C. & Salgia, R. The role of ephrins and Eph receptors in cancer. *Cytokine Growth Factor Rev* **15**, 419-433 (2004).
206. Wimmer-Kleikamp, S.H. & Lackmann, M. Eph-modulated cell morphology, adhesion and motility in carcinogenesis. *IUBMB Life* **57**, 421-431 (2005).

207. Dodelet, V.C. & Pasquale, E.B. Eph receptors and ephrin ligands: embryogenesis to tumorigenesis. *Oncogene* **19**, 5614-5619 (2000).
208. Kullander, K. & Klein, R. Mechanisms and functions of Eph and ephrin signalling. *Nat Rev Mol Cell Biol* **3**, 475-486 (2002).
209. Ellis, C., *et al.* A juxtamembrane autophosphorylation site in the Eph family receptor tyrosine kinase, Sek, mediates high affinity interaction with p59fyn. *Oncogene* **12**, 1727-1736 (1996).
210. Holland, S.J., *et al.* Juxtamembrane tyrosine residues couple the Eph family receptor EphB2/Nuk to specific SH2 domain proteins in neuronal cells. *Embo J* **16**, 3877-3888 (1997).
211. Wahl, S., Barth, H., Ciossek, T., Aktories, K. & Mueller, B.K. Ephrin-A5 induces collapse of growth cones by activating Rho and Rho kinase. *J Cell Biol* **149**, 263-270 (2000).
212. Bruckner, K., Pasquale, E.B. & Klein, R. Tyrosine phosphorylation of transmembrane ligands for Eph receptors. *Science* **275**, 1640-1643 (1997).
213. Holland, S.J., *et al.* Bidirectional signalling through the EPH-family receptor Nuk and its transmembrane ligands. *Nature* **383**, 722-725 (1996).
214. Davy, A., *et al.* Compartmentalized signaling by GPI-anchored ephrin-A5 requires the Fyn tyrosine kinase to regulate cellular adhesion. *Genes Dev* **13**, 3125-3135 (1999).
215. Davy, A. & Robbins, S.M. Ephrin-A5 modulates cell adhesion and morphology in an integrin-dependent manner. *Embo J* **19**, 5396-5405 (2000).

216. Pasquale, E.B. Eph-ephrin promiscuity is now crystal clear. *Nat Neurosci* **7**, 417-418 (2004).
217. Gale, N.W., *et al.* Eph receptors and ligands comprise two major specificity subclasses and are reciprocally compartmentalized during embryogenesis. *Neuron* **17**, 9-19 (1996).
218. Takemoto, M., *et al.* Ephrin-B3-EphA4 interactions regulate the growth of specific thalamocortical axon populations in vitro. *Eur J Neurosci* **16**, 1168-1172 (2002).
219. Himanen, J.P., *et al.* Repelling class discrimination: ephrin-A5 binds to and activates EphB2 receptor signaling. *Nat Neurosci* **7**, 501-509 (2004).
220. Hornberger, M.R., *et al.* Modulation of EphA receptor function by coexpressed ephrinA ligands on retinal ganglion cell axons. *Neuron* **22**, 731-742 (1999).
221. Marquardt, T., *et al.* Coexpressed EphA receptors and ephrin-A ligands mediate opposing actions on growth cone navigation from distinct membrane domains. *Cell* **121**, 127-139 (2005).
222. Biervert, C., Horvath, E. & Fahrig, T. Semiquantitative expression analysis of ephrine-receptor tyrosine kinase mRNA's in a rat model of traumatic brain injury. *Neurosci Lett* **315**, 25-28 (2001).
223. Moreno-Flores, M.T. & Wandosell, F. Up-regulation of Eph tyrosine kinase receptors after excitotoxic injury in adult hippocampus. *Neuroscience* **91**, 193-201 (1999).

224. Bundesen, L.Q., Scheel, T.A., Bregman, B.S. & Kromer, L.F. Ephrin-B2 and EphB2 regulation of astrocyte-meningeal fibroblast interactions in response to spinal cord lesions in adult rats. *J Neurosci* **23**, 7789-7800 (2003).
225. Fabes, J., *et al.* Accumulation of the inhibitory receptor EphA4 may prevent regeneration of corticospinal tract axons following lesion. *Eur J Neurosci* **23**, 1721-1730 (2006).
226. Miranda, J.D., *et al.* Induction of Eph B3 after spinal cord injury. *Exp Neurol* **156**, 218-222 (1999).
227. Willson, C.A., *et al.* Upregulation of EphA receptor expression in the injured adult rat spinal cord. *Cell Transplant* **11**, 229-239 (2002).
228. Willson, C.A., Miranda, J.D., Foster, R.D., Onifer, S.M. & Whittemore, S.R. Transection of the adult rat spinal cord upregulates EphB3 receptor and ligand expression. *Cell Transplant* **12**, 279-290 (2003).
229. Goldshmit, Y., Galea, M.P., Wise, G., Bartlett, P.F. & Turnley, A.M. Axonal regeneration and lack of astrocytic gliosis in EphA4-deficient mice. *J Neurosci* **24**, 10064-10073 (2004).
230. Henkemeyer, M., *et al.* Nuk controls pathfinding of commissural axons in the mammalian central nervous system. *Cell* **86**, 35-46 (1996).
231. Orioli, D., Henkemeyer, M., Lemke, G., Klein, R. & Pawson, T. Sek4 and Nuk receptors cooperate in guidance of commissural axons and in palate formation. *Embo J* **15**, 6035-6049 (1996).
232. Fu, C.T. & Sretavan, D. Laser-Induced Ocular Hypertension in Albino CD-1 Mice. *Invest Ophthalmol Vis Sci* **Manuscript ID IOVS-09-3579.R1**(2009).

233. Birgbauer, E., Cowan, C.A., Sretavan, D.W. & Henkemeyer, M. Kinase independent function of EphB receptors in retinal axon pathfinding to the optic disc from dorsal but not ventral retina. *Development* **127**, 1231-1241 (2000).
234. Pfaffl, M.W. A new mathematical model for relative quantification in real-time RT-PCR. *Nucleic Acids Res* **29**, e45 (2001).
235. Poliakov, A., Cotrina, M. & Wilkinson, D.G. Diverse roles of eph receptors and ephrins in the regulation of cell migration and tissue assembly. *Dev Cell* **7**, 465-480 (2004).
236. Halloran, M.C. & Wolman, M.A. Repulsion or adhesion: receptors make the call. *Curr Opin Cell Biol* **18**, 533-540 (2006).
237. Butt, A.M., Pugh, M., Hubbard, P. & James, G. Functions of optic nerve glia: axoglial signalling in physiology and pathology. *Eye* **18**, 1110-1121 (2004).
238. Himeda, T., *et al.* Time dependent alterations of co-localization of S100beta and GFAP in the MPTP-treated mice. *J Neural Transm* **113**, 1887-1894 (2006).
239. Ogata, K. & Kosaka, T. Structural and quantitative analysis of astrocytes in the mouse hippocampus. *Neuroscience* **113**, 221-233 (2002).
240. Ito, D., *et al.* Microglia-specific localisation of a novel calcium binding protein, Iba1. *Brain Res Mol Brain Res* **57**, 1-9 (1998).
241. Albelda, S.M., Muller, W.A., Buck, C.A. & Newman, P.J. Molecular and cellular properties of PECAM-1 (endoCAM/CD31): a novel vascular cell-cell adhesion molecule. *J Cell Biol* **114**, 1059-1068 (1991).
242. Sattentau, Q.J. & Weiss, R.A. The CD4 antigen: physiological ligand and HIV receptor. *Cell* **52**, 631-633 (1988).

243. Cosulich, M.E., Rubartelli, A., Risso, A., Cozzolino, F. & Bargellesi, A. Functional characterization of an antigen involved in an early step of T-cell activation. *Proc Natl Acad Sci U S A* **84**, 4205-4209 (1987).
244. Pasquale, E.B. Eph-ephrin bidirectional signaling in physiology and disease. *Cell* **133**, 38-52 (2008).
245. Moeller, M.L., Shi, Y., Reichardt, L.F. & Ethell, I.M. EphB receptors regulate dendritic spine morphogenesis through the recruitment/phosphorylation of focal adhesion kinase and RhoA activation. *J Biol Chem* **281**, 1587-1598 (2006).
246. Schmidt, J., Agapova, O.A., Yang, P., Kaufman, P.L. & Hernandez, M.R. Expression of EphrinB1 and its Receptor in Glaucomatous Optic Neuropathy. *Br J Ophthalmol* (2007).
247. Maragakis, N.J. & Rothstein, J.D. Mechanisms of Disease: astrocytes in neurodegenerative disease. *Nat Clin Pract Neurol* **2**, 679-689 (2006).
248. Hanisch, U.K. & Kettenmann, H. Microglia: active sensor and versatile effector cells in the normal and pathologic brain. *Nat Neurosci* **10**, 1387-1394 (2007).
249. Yuan, L. & Neufeld, A.H. Activated microglia in the human glaucomatous optic nerve head. *J Neurosci Res* **64**, 523-532 (2001).
250. Ju, K.R., Kim, H.S., Kim, J.H., Lee, N.Y. & Park, C.K. Retinal glial cell responses and Fas/FasL activation in rats with chronic ocular hypertension. *Brain Res* **1122**, 209-221 (2006).
251. Inman, D.M. & Horner, P.J. Reactive nonproliferative gliosis predominates in a chronic mouse model of glaucoma. *Glia* **55**, 942-953 (2007).

252. Tan, A.M., Colletti, M., Rorai, A.T., Skene, J.H. & Levine, J.M. Antibodies against the NG2 proteoglycan promote the regeneration of sensory axons within the dorsal columns of the spinal cord. *J Neurosci* **26**, 4729-4739 (2006).
253. Nishiyama, A. Polydendrocytes: NG2 cells with many roles in development and repair of the CNS. *Neuroscientist* **13**, 62-76 (2007).
254. Horvath, L.L., Galimi, F., Gage, F.H. & Horner, P.J. Fate of endogenous stem/progenitor cells following spinal cord injury. *J Comp Neurol* **498**, 525-538 (2006).
255. Yokoyama, A., Sakamoto, A., Kameda, K., Imai, Y. & Tanaka, J. NG2 proteoglycan-expressing microglia as multipotent neural progenitors in normal and pathologic brains. *Glia* **53**, 754-768 (2006).
256. Mendes, S.W., Henkemeyer, M. & Liebl, D.J. Multiple Eph receptors and B-class ephrins regulate midline crossing of corpus callosum fibers in the developing mouse forebrain. *J Neurosci* **26**, 882-892 (2006).
257. Egea, J. & Klein, R. Bidirectional Eph-ephrin signaling during axon guidance. *Trends Cell Biol* **17**, 230-238 (2007).
258. Kayser, M.S., McClelland, A.C., Hughes, E.G. & Dalva, M.B. Intracellular and trans-synaptic regulation of glutamatergic synaptogenesis by EphB receptors. *J Neurosci* **26**, 12152-12164 (2006).
259. Klein, R. Bidirectional modulation of synaptic functions by Eph/ephrin signaling. *Nat Neurosci* **12**, 15-20 (2009).
260. Normando, E.M., Coxon, K.M., Guo, L. & Cordeiro, M.F. Focus on: amyloid beta. *Exp Eye Res* **89**, 446-447 (2009).

261. Gupta, N. & Yucel, Y.H. Glaucoma as a neurodegenerative disease. *Curr Opin Ophthalmol* **18**, 110-114 (2007).
262. Bayer, A.U., Ferrari, F. & Erb, C. High occurrence rate of glaucoma among patients with Alzheimer's disease. *Eur Neurol* **47**, 165-168 (2002).
263. Bayer, A.U., Keller, O.N., Ferrari, F. & Maag, K.P. Association of glaucoma with neurodegenerative diseases with apoptotic cell death: Alzheimer's disease and Parkinson's disease. *Am J Ophthalmol* **133**, 135-137 (2002).
264. Tamura, H., *et al.* High frequency of open-angle glaucoma in Japanese patients with Alzheimer's disease. *J Neurol Sci* **246**, 79-83 (2006).
265. Mattson, M.P. Pathways towards and away from Alzheimer's disease. *Nature* **430**, 631-639 (2004).
266. Yoneda, S., *et al.* Vitreous fluid levels of beta-amyloid((1-42)) and tau in patients with retinal diseases. *Jpn J Ophthalmol* **49**, 106-108 (2005).
267. Guo, L., *et al.* Targeting amyloid-beta in glaucoma treatment. *Proc Natl Acad Sci USA* **104**, 13444-13449 (2007).
268. Goldblum, D., Kipfer-Kauer, A., Sarra, G.M., Wolf, S. & Frueh, B.E. Distribution of Amyloid Precursor Protein and Amyloid- β Immunoreactivity in DBA/2J Glaucomatous Mouse Retinas. *Invest Ophthalmol Vis Sci* **48**, 5085-5090 (2007).
269. Bergmann, M., Post, A., Rittel, I., Bechmann, I. & Nitsch, R. Expression of synaptophysin in sprouting neurons after entorhinal lesion in the rat. *Exp Brain Res* **117**, 80-86 (1997).

270. Styren, S.D., Miller, P.D., Lagenaur, C.F. & DeKosky, S.T. Alternate strategies in lesion-induced reactive synaptogenesis: differential expression of L1 in two populations of sprouting axons. *Exp Neurol* **131**, 165-173 (1995).
271. Xie, W., Strong, J.A., Li, H. & Zhang, J.M. Sympathetic sprouting near sensory neurons after nerve injury occurs preferentially on spontaneously active cells and is reduced by early nerve block. *J Neurophysiol* **97**, 492-502 (2007).
272. Masliah, E., *et al.* An antibody against phosphorylated neurofilaments identifies a subset of damaged association axons in Alzheimer's disease. *Am J Pathol* **142**, 871-882 (1993).
273. Masliah, E., *et al.* Localization of amyloid precursor protein in GAP43-immunoreactive aberrant sprouting neurites in Alzheimer's disease. *Brain Res* **574**, 312-316 (1992).
274. Masliah, E., Hansen, L., Albright, T., Mallory, M. & Terry, R.D. Immunoelectron microscopic study of synaptic pathology in Alzheimer's disease. *Acta Neuropathol* **81**, 428-433 (1991).
275. Lassmann, H., Fischer, P. & Jellinger, K. Synaptic pathology of Alzheimer's disease. *Ann N Y Acad Sci* **695**, 59-64 (1993).
276. Masliah, E., Terry, R.D., Alford, M., DeTeresa, R. & Hansen, L.A. Cortical and subcortical patterns of synaptophysinlike immunoreactivity in Alzheimer's disease. *Am J Pathol* **138**, 235-246 (1991).
277. Tsien, J.Z., Huerta, P.T. & Tonegawa, S. The essential role of hippocampal CA1 NMDA receptor-dependent synaptic plasticity in spatial memory. *Cell* **87**, 1327-1338 (1996).

278. Hnasko, T.S., *et al.* Vesicular glutamate transport promotes dopamine storage and glutamate corelease in vivo. *Neuron* **65**, 643-656 (2010).
279. Innocenti, B., Parpura, V. & Haydon, P.G. Imaging extracellular waves of glutamate during calcium signaling in cultured astrocytes. *J Neurosci* **20**, 1800-1808 (2000).
280. Park, K.K., *et al.* Promoting axon regeneration in the adult CNS by modulation of the PTEN/mTOR pathway. *Science* **322**, 963-966 (2008).
281. Johnson, J., *et al.* Vesicular neurotransmitter transporter expression in developing postnatal rodent retina: GABA and glycine precede glutamate. *J Neurosci* **23**, 518-529 (2003).
282. Sharma, R.K., O'Leary, T.E., Fields, C.M. & Johnson, D.A. Development of the outer retina in the mouse. *Brain Res Dev Brain Res* **145**, 93-105 (2003).
283. Fremeau, R.T., Jr., *et al.* The expression of vesicular glutamate transporters defines two classes of excitatory synapse. *Neuron* **31**, 247-260 (2001).
284. Johnson, J., *et al.* Vesicular glutamate transporter 1 is required for photoreceptor synaptic signaling but not for intrinsic visual functions. *J Neurosci* **27**, 7245-7255 (2007).
285. Stella, S.L., Jr., Li, S., Sabatini, A., Vila, A. & Brecha, N.C. Comparison of the ontogeny of the vesicular glutamate transporter 3 (VGLUT3) with VGLUT1 and VGLUT2 in the rat retina. *Brain Res* **1215**, 20-29 (2008).
286. Fujiyama, F., *et al.* Changes of immunocytochemical localization of vesicular glutamate transporters in the rat visual system after the retinofugal denervation. *J Comp Neurol* **465**, 234-249 (2003).

287. Gong, J., *et al.* Distribution of vesicular glutamate transporters in rat and human retina. *Brain Res* **1082**, 73-85 (2006).
288. Sherry, D.M., Wang, M.M., Bates, J. & Frishman, L.J. Expression of vesicular glutamate transporter 1 in the mouse retina reveals temporal ordering in development of rod vs. cone and ON vs. OFF circuits. *J Comp Neurol* **465**, 480-498 (2003).
289. Wassle, H., Regus-Leidig, H. & Haverkamp, S. Expression of the vesicular glutamate transporter vGluT2 in a subset of cones of the mouse retina. *J Comp Neurol* **496**, 544-555 (2006).
290. Land, P.W., Kyonka, E. & Shamalla-Hannah, L. Vesicular glutamate transporters in the lateral geniculate nucleus: expression of VGLUT2 by retinal terminals. *Brain Res* **996**, 251-254 (2004).
291. Fyk-Kolodziej, B., Dzhagaryan, A., Qin, P. & Pourcho, R.G. Immunocytochemical localization of three vesicular glutamate transporters in the cat retina. *J Comp Neurol* **475**, 518-530 (2004).
292. Shen, Y., Liu, X.L. & Yang, X.L. N-methyl-D-aspartate receptors in the retina. *Mol Neurobiol* **34**, 163-179 (2006).
293. Sudhof, T.C. & Rothman, J.E. Membrane fusion: grappling with SNARE and SM proteins. *Science* **323**, 474-477 (2009).
294. tom Dieck, S., *et al.* Bassoon, a novel zinc-finger CAG/glutamine-repeat protein selectively localized at the active zone of presynaptic nerve terminals. *J Cell Biol* **142**, 499-509 (1998).

295. Schoch, S. & Gundelfinger, E.D. Molecular organization of the presynaptic active zone. *Cell Tissue Res* **326**, 379-391 (2006).
296. Dick, O., *et al.* The presynaptic active zone protein bassoon is essential for photoreceptor ribbon synapse formation in the retina. *Neuron* **37**, 775-786 (2003).
297. Altrock, W.D., *et al.* Functional inactivation of a fraction of excitatory synapses in mice deficient for the active zone protein bassoon. *Neuron* **37**, 787-800 (2003).
298. tom Dieck, S., *et al.* Molecular dissection of the photoreceptor ribbon synapse: physical interaction of Bassoon and RIBEYE is essential for the assembly of the ribbon complex. *J Cell Biol* **168**, 825-836 (2005).
299. Sudhof, T.C. The synaptic vesicle cycle. *Annu Rev Neurosci* **27**, 509-547 (2004).
300. Kraszewski, K., *et al.* Synaptic vesicle dynamics in living cultured hippocampal neurons visualized with CY3-conjugated antibodies directed against the luminal domain of synaptotagmin. *J Neurosci* **15**, 4328-4342 (1995).
301. Matteoli, M., Takei, K., Perin, M.S., Sudhof, T.C. & De Camilli, P. Exo-endocytotic recycling of synaptic vesicles in developing processes of cultured hippocampal neurons. *J Cell Biol* **117**, 849-861 (1992).
302. Rosenmund, C. & Stevens, C.F. Definition of the readily releasable pool of vesicles at hippocampal synapses. *Neuron* **16**, 1197-1207 (1996).
303. Gerber, S.H., *et al.* Conformational switch of syntaxin-1 controls synaptic vesicle fusion. *Science* **321**, 1507-1510 (2008).
304. Maguire, G., Simko, H., Weinreb, R.N. & Ayoub, G. Transport-mediated release of endogenous glutamate in the vertebrate retina. *Pflugers Arch* **436**, 481-484 (1998).

305. Ayoub, G.S. & Dorst, K. Imaging of glutamate release from the goldfish retinal slice. *Vision Res* **38**, 2909-2912 (1998).
306. Ayoub, G.S., Grutis, S. & Simko, H. Imaging of endogenous neurotransmitter release. *J Neurosci Methods* **81**, 113-119 (1998).
307. Chang, Y.C. & Chiao, C.C. Localization and functional mapping of AMPA receptor subunits in the developing rabbit retina. *Invest Ophthalmol Vis Sci* **49**, 5619-5628 (2008).
308. Acosta, M.L., Bumsted O'Brien, K.M., Tan, S.S. & Kalloniatis, M. Emergence of cellular markers and functional ionotropic glutamate receptors on tangentially dispersed cells in the developing mouse retina. *J Comp Neurol* **506**, 506-523 (2008).
309. Sun, D., Bui, B.V., Vingrys, A.J. & Kalloniatis, M. Alterations in photoreceptor-bipolar cell signaling following ischemia/reperfusion in the rat retina. *J Comp Neurol* **505**, 131-146 (2007).
310. Sun, D., Vingrys, A.J. & Kalloniatis, M. Metabolic and functional profiling of the normal rat retina. *J Comp Neurol* **505**, 92-113 (2007).
311. Acosta, M.L., Chua, J. & Kalloniatis, M. Functional activation of glutamate ionotropic receptors in the developing mouse retina. *J Comp Neurol* **500**, 923-941 (2007).
312. Sun, D. & Kalloniatis, M. Mapping glutamate responses in immunocytochemically identified neurons of the mouse retina. *J Comp Neurol* **494**, 686-703 (2006).

313. Marc, R.E., Kalloniatis, M. & Jones, B.W. Excitation mapping with the organic cation AGB2+. *Vision Res* **45**, 3454-3468 (2005).
314. Sun, D. & Kalloniatis, M. Quantification of amino acid neurochemistry secondary to NMDA or betaxolol application. *Clin Experiment Ophthalmol* **32**, 505-517 (2004).
315. Rohrer, B., *et al.* Functionally intact glutamate-mediated signaling in bipolar cells of the TRKB knockout mouse retina. *Vis Neurosci* **21**, 703-713 (2004).
316. Kalloniatis, M., Sun, D., Foster, L., Haverkamp, S. & Wassle, H. Localization of NMDA receptor subunits and mapping NMDA drive within the mammalian retina. *Vis Neurosci* **21**, 587-597 (2004).
317. Sun, D., Rait, J.L. & Kalloniatis, M. Inner retinal neurons display differential responses to N-methyl-D-aspartate receptor activation. *J Comp Neurol* **465**, 38-56 (2003).
318. Kalloniatis, M., Tomisich, G., Wellard, J.W. & Foster, L.E. Mapping photoreceptor and postreceptoral labelling patterns using a channel permeable probe (agmatine) during development in the normal and RCS rat retina. *Vis Neurosci* **19**, 61-70 (2002).
319. Marc, R.E. Mapping glutamatergic drive in the vertebrate retina with a channel-permeant organic cation. *J Comp Neurol* **407**, 47-64 (1999).
320. Marc, R.E. Kainate activation of horizontal, bipolar, amacrine, and ganglion cells in the rabbit retina. *J Comp Neurol* **407**, 65-76 (1999).
321. Tsien, J.Z., *et al.* Subregion- and cell type-restricted gene knockout in mouse brain. *Cell* **87**, 1317-1326 (1996).

322. Cheng, L., Sapieha, P., Kittlerova, P., Hauswirth, W.W. & Di Polo, A. TrkB gene transfer protects retinal ganglion cells from axotomy-induced death in vivo. *J Neurosci* **22**, 3977-3986 (2002).
323. Hellstrom, M., *et al.* Cellular tropism and transduction properties of seven adeno-associated viral vector serotypes in adult retina after intravitreal injection. *Gene Ther* **16**, 521-532 (2009).
324. Ivanova, E. & Pan, Z.H. Evaluation of the adeno-associated virus mediated long-term expression of channelrhodopsin-2 in the mouse retina. *Mol Vis* **15**, 1680-1689 (2009).
325. Malik, J.M., Shevtsova, Z., Bahr, M. & Kugler, S. Long-term in vivo inhibition of CNS neurodegeneration by Bcl-XL gene transfer. *Mol Ther* **11**, 373-381 (2005).
326. Martin, K.R., Klein, R.L. & Quigley, H.A. Gene delivery to the eye using adeno-associated viral vectors. *Methods* **28**, 267-275 (2002).
327. Madisen, L., *et al.* A robust and high-throughput Cre reporting and characterization system for the whole mouse brain. *Nat Neurosci* **13**, 133-140 (2010).
328. Nakanishi, S. Molecular diversity of glutamate receptors and implications for brain function. *Science* **258**, 597-603 (1992).
329. Moriyoshi, K., *et al.* Molecular cloning and characterization of the rat NMDA receptor. *Nature* **354**, 31-37 (1991).
330. Shapira, M., *et al.* Unitary assembly of presynaptic active zones from Piccolo-Bassoon transport vesicles. *Neuron* **38**, 237-252 (2003).

331. Zhai, R.G., *et al.* Assembling the presynaptic active zone: a characterization of an active one precursor vesicle. *Neuron* **29**, 131-143 (2001).
332. Ahmari, S.E., Buchanan, J. & Smith, S.J. Assembly of presynaptic active zones from cytoplasmic transport packets. *Nat Neurosci* **3**, 445-451 (2000).
333. Goldstein, A.Y., Wang, X. & Schwarz, T.L. Axonal transport and the delivery of pre-synaptic components. *Curr Opin Neurobiol* **18**, 495-503 (2008).
334. Dai, Z. & Peng, H.B. Fluorescence microscopy of calcium and synaptic vesicle dynamics during synapse formation in tissue culture. *Histochem J* **30**, 189-196 (1998).
335. Zakharenko, S., Chang, S., O'Donoghue, M. & Popov, S.V. Neurotransmitter secretion along growing nerve processes: comparison with synaptic vesicle exocytosis. *J Cell Biol* **144**, 507-518 (1999).
336. Krueger, S.R., Kolar, A. & Fitzsimonds, R.M. The presynaptic release apparatus is functional in the absence of dendritic contact and highly mobile within isolated axons. *Neuron* **40**, 945-957 (2003).
337. Turner, T.J. Nicotine enhancement of dopamine release by a calcium-dependent increase in the size of the readily releasable pool of synaptic vesicles. *J Neurosci* **24**, 11328-11336 (2004).
338. Kashani, A.H., Chen, B.M. & Grinnell, A.D. Hypertonic enhancement of transmitter release from frog motor nerve terminals: Ca²⁺ independence and role of integrins. *J Physiol* **530**, 243-252 (2001).
339. Attwell, D., Barbour, B. & Szatkowski, M. Nonvesicular release of neurotransmitter. *Neuron* **11**, 401-407 (1993).

340. Matsui, K. & Jahr, C.E. Exocytosis unbound. *Curr Opin Neurobiol* **16**, 305-311 (2006).
341. Ceccarelli, B., Fesce, R., Grohovaz, F. & Haimann, C. The effect of potassium on exocytosis of transmitter at the frog neuromuscular junction. *J Physiol* **401**, 163-183 (1988).
342. Ceccarelli, B., Grohovaz, F. & Hurlbut, W.P. Freeze-fracture studies of frog neuromuscular junctions during intense release of neurotransmitter. II. Effects of electrical stimulation and high potassium. *J Cell Biol* **81**, 178-192 (1979).
343. Zenisek, D., Steyer, J.A. & Almers, W. Transport, capture and exocytosis of single synaptic vesicles at active zones. *Nature* **406**, 849-854 (2000).
344. Zenisek, D., Davila, V., Wan, L. & Almers, W. Imaging calcium entry sites and ribbon structures in two presynaptic cells. *J Neurosci* **23**, 2538-2548 (2003).
345. Lenzi, D., Crum, J., Ellisman, M.H. & Roberts, W.M. Depolarization redistributes synaptic membrane and creates a gradient of vesicles on the synaptic body at a ribbon synapse. *Neuron* **36**, 649-659 (2002).
346. Coggan, J.S., *et al.* Evidence for ectopic neurotransmission at a neuronal synapse. *Science* **309**, 446-451 (2005).
347. Matsui, K., Jahr, C.E. & Rubio, M.E. High-concentration rapid transients of glutamate mediate neural-glia communication via ectopic release. *J Neurosci* **25**, 7538-7547 (2005).
348. Matsui, K. & Jahr, C.E. Differential control of synaptic and ectopic vesicular release of glutamate. *J Neurosci* **24**, 8932-8939 (2004).

349. Matsui, K. & Jahr, C.E. Ectopic release of synaptic vesicles. *Neuron* **40**, 1173-1183 (2003).
350. Ziskin, J.L., Nishiyama, A., Rubio, M., Fukaya, M. & Bergles, D.E. Vesicular release of glutamate from unmyelinated axons in white matter. *Nat Neurosci* **10**, 321-330 (2007).
351. Kukley, M., Capetillo-Zarate, E. & Dietrich, D. Vesicular glutamate release from axons in white matter. *Nat Neurosci* **10**, 311-320 (2007).
352. Thyssen, A., *et al.* Ectopic vesicular neurotransmitter release along sensory axons mediates neurovascular coupling via glial calcium signaling. *Proc Natl Acad Sci U S A* **107**, 15258-15263 (2010).
353. Garcia, E.P., McPherson, P.S., Chilcote, T.J., Takei, K. & De Camilli, P. rbSec1A and B colocalize with syntaxin 1 and SNAP-25 throughout the axon, but are not in a stable complex with syntaxin. *J Cell Biol* **129**, 105-120 (1995).
354. Hagiwara, A., Fukazawa, Y., Deguchi-Tawarada, M., Ohtsuka, T. & Shigemoto, R. Differential distribution of release-related proteins in the hippocampal CA3 area as revealed by freeze-fracture replica labeling. *J Comp Neurol* **489**, 195-216 (2005).
355. Fletcher, E.L., Hack, I., Brandstatter, J.H. & Wassle, H. Synaptic localization of NMDA receptor subunits in the rat retina. *J Comp Neurol* **420**, 98-112 (2000).
356. Micu, I., *et al.* NMDA receptors mediate calcium accumulation in myelin during chemical ischaemia. *Nature* **439**, 988-992 (2006).

357. South, S.M., *et al.* A conditional deletion of the NR1 subunit of the NMDA receptor in adult spinal cord dorsal horn reduces NMDA currents and injury-induced pain. *J Neurosci* **23**, 5031-5040 (2003).
358. Grunder, T., Kohler, K., Kaletta, A. & Guenther, E. The distribution and developmental regulation of NMDA receptor subunit proteins in the outer and inner retina of the rat. *J Neurobiol* **44**, 333-342 (2000).
359. Randle, J.C., Guet, T., Cordi, A. & Lepagnol, J.M. Competitive inhibition by NBQX of kainate/AMPA receptor currents and excitatory synaptic potentials: importance of 6-nitro substitution. *Eur J Pharmacol* **215**, 237-244 (1992).
360. Tricklebank, M.D., Singh, L., Oles, R.J., Preston, C. & Iversen, S.D. The behavioural effects of MK-801: a comparison with antagonists acting non-competitively and competitively at the NMDA receptor. *Eur J Pharmacol* **167**, 127-135 (1989).
361. Bakiri, Y., *et al.* Glutamatergic signaling in the brain's white matter. *Neuroscience* **158**, 266-274 (2009).
362. Ouardouz, M., *et al.* Glutamate receptors on myelinated spinal cord axons: I. GluR6 kainate receptors. *Ann Neurol* **65**, 151-159 (2009).
363. Ouardouz, M., *et al.* Glutamate receptors on myelinated spinal cord axons: II. AMPA and GluR5 receptors. *Ann Neurol* **65**, 160-166 (2009).
364. Ouardouz, M., Malek, S., Coderre, E. & Stys, P.K. Complex interplay between glutamate receptors and intracellular Ca²⁺ stores during ischaemia in rat spinal cord white matter. *J Physiol* **577**, 191-204 (2006).

365. Fowler, J.H., McCracken, E., Dewar, D. & McCulloch, J. Intracerebral injection of AMPA causes axonal damage in vivo. *Brain Res* **991**, 104-112 (2003).
366. Matute, C. Characteristics of acute and chronic kainate excitotoxic damage to the optic nerve. *Proc Natl Acad Sci U S A* **95**, 10229-10234 (1998).
367. Tekkok, S.B., Ye, Z. & Ransom, B.R. Excitotoxic mechanisms of ischemic injury in myelinated white matter. *J Cereb Blood Flow Metab* **27**, 1540-1552 (2007).
368. Tekkok, S.B. & Goldberg, M.P. Ampa/kainate receptor activation mediates hypoxic oligodendrocyte death and axonal injury in cerebral white matter. *J Neurosci* **21**, 4237-4248 (2001).
369. Li, S., Mealing, G.A., Morley, P. & Stys, P.K. Novel injury mechanism in anoxia and trauma of spinal cord white matter: glutamate release via reverse Na⁺-dependent glutamate transport. *J Neurosci* **19**, RC16 (1999).
370. Agrawal, S.K. & Fehlings, M.G. Role of NMDA and non-NMDA ionotropic glutamate receptors in traumatic spinal cord axonal injury. *J Neurosci* **17**, 1055-1063 (1997).
371. McCracken, E., Fowler, J.H., Dewar, D., Morrison, S. & McCulloch, J. Grey matter and white matter ischemic damage is reduced by the competitive AMPA receptor antagonist, SPD 502. *J Cereb Blood Flow Metab* **22**, 1090-1097 (2002).
372. Smith, T., Groom, A., Zhu, B. & Turski, L. Autoimmune encephalomyelitis ameliorated by AMPA antagonists. *Nat Med* **6**, 62-66 (2000).
373. Pitt, D., Werner, P. & Raine, C.S. Glutamate excitotoxicity in a model of multiple sclerosis. *Nat Med* **6**, 67-70 (2000).

374. Kanellopoulos, G.K., *et al.* White matter injury in spinal cord ischemia: protection by AMPA/kainate glutamate receptor antagonism. *Stroke* **31**, 1945-1952 (2000).
375. Wrathall, J.R., Choiniere, D. & Teng, Y.D. Dose-dependent reduction of tissue loss and functional impairment after spinal cord trauma with the AMPA/kainate antagonist NBQX. *J Neurosci* **14**, 6598-6607 (1994).
376. Jakobs, T.C., Ben, Y. & Masland, R.H. Expression of mRNA for glutamate receptor subunits distinguishes the major classes of retinal neurons, but is less specific for individual cell types. *Mol Vis* **13**, 933-948 (2007).
377. Watanabe, M., Mishina, M. & Inoue, Y. Differential distributions of the NMDA receptor channel subunit mRNAs in the mouse retina. *Brain Res* **634**, 328-332 (1994).
378. Brandstatter, J.H., Hartveit, E., Sassoe-Pognetto, M. & Wassle, H. Expression of NMDA and high-affinity kainate receptor subunit mRNAs in the adult rat retina. *Eur J Neurosci* **6**, 1100-1112 (1994).
379. Chen, S. & Diamond, J.S. Synaptically released glutamate activates extrasynaptic NMDA receptors on cells in the ganglion cell layer of rat retina. *J Neurosci* **22**, 2165-2173 (2002).
380. Vorwerk, C.K., *et al.* Excitotoxicity can be mediated through an interaction within the optic nerve; activation of cell body NMDA receptors is not required. *Vet Ophthalmol* **4**, 201-204 (2001).
381. Song, A.H., *et al.* A selective filter for cytoplasmic transport at the axon initial segment. *Cell* **136**, 1148-1160 (2009).

382. Gracy, K.N. & Pickel, V.M. Comparative ultrastructural localization of the NMDAR1 glutamate receptor in the rat basolateral amygdala and bed nucleus of the stria terminalis. *J Comp Neurol* **362**, 71-85 (1995).
383. Aoki, C., Venkatesan, C., Go, C.G., Mong, J.A. & Dawson, T.M. Cellular and subcellular localization of NMDA-R1 subunit immunoreactivity in the visual cortex of adult and neonatal rats. *J Neurosci* **14**, 5202-5222 (1994).
384. Bardoni, R., Torsney, C., Tong, C.K., Prandini, M. & MacDermott, A.B. Presynaptic NMDA receptors modulate glutamate release from primary sensory neurons in rat spinal cord dorsal horn. *J Neurosci* **24**, 2774-2781 (2004).
385. Duguid, I.C. & Smart, T.G. Retrograde activation of presynaptic NMDA receptors enhances GABA release at cerebellar interneuron-Purkinje cell synapses. *Nat Neurosci* **7**, 525-533 (2004).
386. Soto, I., *et al.* Retinal Ganglion Cell Loss in a Rat Ocular Hypertension Model is Sectorial and Involves Early Optic Nerve Axon Loss. *Invest Ophthalmol Vis Sci* (2010).
387. Hare, W.A., *et al.* Efficacy and safety of memantine treatment for reduction of changes associated with experimental glaucoma in monkey, II: Structural measures. *Invest Ophthalmol Vis Sci* **45**, 2640-2651 (2004).
388. Martin, K.R., *et al.* Retinal glutamate transporter changes in experimental glaucoma and after optic nerve transection in the rat. *Invest Ophthalmol Vis Sci* **43**, 2236-2243 (2002).
389. Morfini, G., *et al.* JNK mediates pathogenic effects of polyglutamine-expanded androgen receptor on fast axonal transport. *Nat Neurosci* **9**, 907-916 (2006).

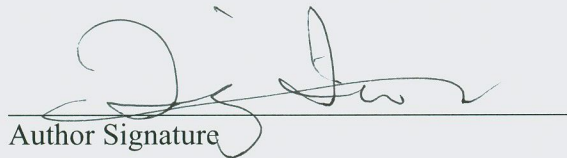
390. Stagi, M., *et al.* Breakdown of axonal synaptic vesicle precursor transport by microglial nitric oxide. *J Neurosci* **25**, 352-362 (2005).
391. Stagi, M., Gorlovoy, P., Larionov, S., Takahashi, K. & Neumann, H. Unloading kinesin transported cargoes from the tubulin track via the inflammatory c-Jun N-terminal kinase pathway. *Faseb J* **20**, 2573-2575 (2006).
392. Falzone, T.L., *et al.* Axonal stress kinase activation and tau misbehavior induced by kinesin-1 transport defects. *J Neurosci* **29**, 5758-5767 (2009).
393. Contractor, A., *et al.* Trans-synaptic Eph receptor-ephrin signaling in hippocampal mossy fiber LTP. *Science* **296**, 1864-1869 (2002).
394. Lim, B.K., Matsuda, N. & Poo, M.M. Ephrin-B reverse signaling promotes structural and functional synaptic maturation in vivo. *Nat Neurosci* **11**, 160-169 (2008).
395. Hansen, M.J., Dallal, G.E. & Flanagan, J.G. Retinal axon response to ephrin-as shows a graded, concentration-dependent transition from growth promotion to inhibition. *Neuron* **42**, 717-730 (2004).
396. Stein, E., *et al.* Eph receptors discriminate specific ligand oligomers to determine alternative signaling complexes, attachment, and assembly responses. *Genes Dev* **12**, 667-678 (1998).

Publishing Agreement

It is the policy of the University to encourage the distribution of all theses, dissertations, and manuscripts. Copies of all UCSF theses, dissertations, and manuscripts will be routed to the library via the Graduate Division. The library will make all theses, dissertations, and manuscripts accessible to the public and will preserve these to the best of their abilities, in perpetuity.

Please sign the following statement:

I hereby grant permission to the Graduate Division of the University of California, San Francisco to release copies of my thesis, dissertation, or manuscript to the Campus Library to provide access and preservation, in whole or in part, in perpetuity.



Author Signature

01/10/2011

Date